PREPARATION OF PNZT THIN FILMS BY SOLUTION DEPOSITION AND THEIR CHARACTERIZATION

A THESIS SUBMITTED TO
THE GRADUATE SCHOOL OF NATURAL AND APPLIED SCIENCES
OF
MIDDLE EAST TECHNICAL UNIVERSITY

BY

VOLKAN KAYASÜ

IN PARTIAL FULFILLMENT OF THE REQUIREMENTS
FOR
THE DEGREE OF MASTER OF SCIENCE
IN
METALLURGICAL AND MATERIALS ENGINEERING

FEBRUARY 2008

Approval of the thesis:

PREPARATION OF PNZT THIN FILMS BY SOLUTION DEPOSITION AND THEIR CHARACTERIZATION

submitted by **VOLKAN KAYASÜ** in partial fulfillment of the requirements for the degree of **Master of Science in Metallurgical and Materials Engineering Department, Middle East Technical University** by,

Prof. Dr. Canan Özgen ____________
Dean, Graduate School of **Natural and Applied Sciences**

Prof. Dr. Tayfur Öztürk ____________
Head of Department, **Metallurgical and Materials Engineering**

Prof. Dr. Macit Özenbaş ____________
Supervisor, **Metallurgical and Materials Engineering Dept., METU**

Examining Committee Members:

Prof. Dr. Muharrem Timuçin __________________
Metallurgical and Materials Engineering Dept., METU

Prof. Dr. Macit Özenbaş __________________
Metallurgical and Materials Engineering Dept., METU

Prof. Dr. Abdullah Öztürk __________________
Metallurgical and Materials Engineering Dept., METU

Asst. Prof. Dr. Caner Durucan __________________
Metallurgical and Materials Engineering Dept., METU

Dr. İbrahim Çam __________________
Central Laboratory, METU

Date: 06.02.2008

I hereby declare that all information in this document has been obtained and presented in accordance with academic rules and ethical conduct. I also declare that, as required by these rules and conduct, I have fully cited and referenced all material and results that are not original to this work.

Name, Last name : Volkan Kayasü

Signature :

ABSTRACT

PREPARATION OF PNZT THIN FILMS BY SOLUTION DEPOSITION AND THEIR CHARACTERIZATION

Kayasü, Volkan
M.S., Department of Metallurgical and Materials Engineering
Supervisor: Prof. Dr. Macit Özenbaş

February 2008, 120 pages

The aim of this study is to produce Nb doped PZT thin films and then investigate the effects of Nb^{+5} ion on the structural, dielectric and ferroelectric properties. Niobium (Nb) doped lead zirconate titanate thin films (PNZT) were produced by solution deposition with nominal compositions, $Pb_{(1-0.5x)}(Zr_{0.53}Ti_{0.47})_{1-x}Nb_xO_3$ where x = 0.00 - 0.07. Single and multi-layered films were deposited onto (111)-Pt/Ti/SiO_2/Si-(100) substrates by spin coating. PZT compositions near the morphotropic phase boundary (MPB) was chosen because excellent ferroelectric and dielectric properties were achieved in this area.

The effects of sintering temperature, sintering time, variation of thickness in the films and change of niobium content were investigated with regard to phase development, microstructure, and ferroelectric and dielectric characteristics. The best results were obtained in double layered films (390 nm) which were sintered at 600 °C for 1 h. Grain size of the films decreases with increasing Nb content except for 1 at % Nb doped films. The average grain size of 1 at % Nb doped thin films was calculated as 130 nm by using FESEM.

Optimum doping level was found in 1 at % Nb doped films. For 1 at % Nb doped [$Pb_{0.995}(Zr_{0.53}Ti_{0.47})_{0.99}Nb_{0.01}O_3$] films, remnant polarization (P_r) of 35.75 $\mu C/cm^2$ and coercive field (E_c) of 75.65 kV/cm have been obtained. The maximum dielectric constant was achieved in 1 at % Nb doped films which was 689. Tangent loss values were found between 2-4 % and these values were independent of Nb concentrations. Ferroelectric and dielectric properties were decreased at higher Nb doping levels because of the changes in the grain size, distortion of the crystal structure and pinning of the domains.

Keywords: Solution Deposition, Ferroelectric Properties, Dielectric Properties, PNZT

ÖZ

FERROELEKTRİK PNZT FİLMLERİN SOL-JEL YÖNTEMİYLE ÜRETİMİ VE KARAKTERİZASYONU

Kayasü, Volkan

Y. Lisans, Metalurji ve Malzeme Mühendisliği Bölümü
Tez Yöneticisi: Prof. Dr. Macit Özenbaş

Şubat 2008, 120 sayfa

Bu çalışmanın amacı Niyobiyum (Nb) eklenmiş kurşun zirkonat titanat (PNZT) ince filmlerini üretmek ve Nb^{5+} iyonunun filmlerin yapısal, ferroelektrik ve dielektrik özelliklerine yaptığı etkiyi incelemektir. PNZT ince filmleri, $Pb_{(1-0.5x)}(Zr_{0.53}Ti_{0.47})_{1-x}Nb_xO_3$ (x = 0.00 - 0.07) kompozisyonuna göre sol-jel yöntemi kullanılarak üretilmişlerdir. Tek ve çok katlı PNZT filmleri (111)-Pt/Ti/SiO_2/Si-(100) altlıkların üzerine kaplanmıştır. PZT kompozisyonları, en iyi ferroelektik ve dielektrik özelliklerin elde edilebilmesi için morfotropik faz sınırından seçilmiştir.

Oluşan filmlerin faz oluşumu, mikroyapı, ferroelektrik ve dielektrik özelliklerine bakılarak film kalınlığı, Nb miktarı, sinterleme sıcaklığı ve zamanı gibi üretim parametrelerinin özellikler üzerine olan etkileri incelenmiştir. En yüksek değerler 2 katlı (390 nm), 600 °C ve 1 saat boyunca sinterlenmiş olan filmlerde elde edilmiştir. 1 at % Nb eklenmiş filmler hariç (tane büyüklüğü : 130 nm), filmlerdeki Nb miktarı arttıkça, tane büyüklüğünün azaldığı görülmüştür.

En iyi sonuçlar 1 at % Nb eklenmiş [$Pb_{0.995}(Zr_{0.53}Ti_{0.47})_{0.99}Nb_{0.01}O_3$] filmlerde görülmüştür. Bu filmlerde elde edilen kalıntı polarizasyon (P_r) ve koersiv alan (E_c) değerleri sırasıyla 35.75 $\mu C/cm^2$ ve 75.65 kV/cm olarak hesaplanmıştır. En yüksek dielektrik sabiti (689) 1 at % Nb eklenmiş PNZT filmlerde elde edilmiştir.

Filmlerdeki dielektrik kaybı 2-4 % arasında değişmektedir ve Nb değişiminin dielektrik kaybı üzerinde bir etkisi olmadığı görülmüştür. Niyobiyumun yüksek miktarlarda eklendiği durumlarda, filmlerin ferroelektrik ve dielektrik özelliklerinde düşüş gözlenmiştir. Bunun nedeni tane boyutundaki azalma, kristal yapıdaki bozulma ve/veya olarak belirlenmiştir.

Anahtar Kelimeler: Çözelti Depolama, Ferroelektrik Özellikler, Dielektrik Özellikler, PNZT

To my family

ACKNOWLEDGEMENTS

I would like to express my sincere gratitude to my supervisor Prof. Dr. Macit Özenbaş for his support, guidance, impatience, supervision and encouragement during the study.

I would like to thank to Dr. İbrahim Çam for his help during the dielectric measurements and for his comments. I am also grateful to all the Department of Metallurgical and Materials Engineering and Central Laboratory staff.

I must thank to Özge Acarbaş and Ali Erdem Eken for their endless support and friendship. I am also thankful to my best friends; Deniz Ceylan and Yusuf Erdem for sharing my hard times with me.

Finally, I would like to express my deepest gratitude to my family Emel and Zafer Kayasü for their endless love and support during my life.

This study was supported by TÜBİTAK Project No: 106M060.

TABLE OF CONTENTS

LIST OF TABLES

TABLES

LIST OF FIGURES

FIGURES

CHAPTER 1

INTRODUCTION

More interest has been given to ferroelectric thin and thick films for electronic applications in the last few years. An increased development has been observed in this field. The history of the ferroelectric thin films began in the 1980's. The research on this subject has accelerated because there is more need of producing high quality films. Current trends in the electronics industries that involve computing, data processing, sensing and communications all point toward a continuing need for improved materials. Some application areas can be classified as memories, modulators, switches, shutters, mixers, sensors, imagers and displays. Higher levels of miniaturization and integration in the future promise more demand for smaller size, higher speed and more integration in present-day devices [1].

Ferroelectric thin films have many advantages toward their bulk counterparts. These are lower operating voltage, more economical processing, greater design flexibility and the ability to fabricate nano-level composites. Furthermore, thin films require low sintering temperatures [1]. Thin films bridge the gap between monolayer and bulk structures. They lay between the thickness range of 1 nanometer to 1 micron [2].

To produce ceramic thin films, there are numerous deposition techniques such as pulsed laser deposition (PLD), molecular beam epitaxy (MBE), chemical vapor deposition (CVD), sputtering and chemical solution deposition (CSD) [3]. Chemical solution deposition process for the production of ferroelectric thin films has many advantages over other methods and will be used in the entire study. Control of chemical composition and microstructure, low cost and high chemical homogeneity are some of the benefits of using chemical solution deposition method.

Solution deposition technique allows low temperature processing conditions and it also offers close control of chemical composition. Sols are deposited onto a substrate by spin coating and then the resulting layer (gel) is heat treated to form a ceramic film [4]. Furthermore, temperature-time requirements for the subsequent crystallization/densification processing can be minimized because of high degree of chemical homogeneity in the polymeric ceramic precursor systems [5].

The PZT ($Pb(Zr_xTi_{1-x})O_3$) perovskites possess a number of properties which make them suitable candidates for memory applications [5]. With some compositional modifications like adding dopants, modifiers or other compositions, the properties can be improved for specific applications [3]. Some important materials that are used for ferroelectric thin films are PZT, PLZT and PNZT, because these materials have good ferroelectric and dielectric properties due to their structural properties.

In this study, lead niobium zirconate titanate with the composition $Pb_{(1-0.5x)}(Zr_{0.53}Ti_{0.47})_{1-x}Nb_xO_3$ is used for the production of thin films. The Zr/Ti ratio is taken constant as 53/47. This ratio in the PZT phase diagram corresponds to morphotropic phase boundary (MPB) and this boundary separates the tetragonal region from the rhombohedral region. Electrical properties are increased at this region giving excellent polarizations and dielectric properties.

The most common applications of PZT and niobium doped PZT thin films are accelerometers, ferroelectric random access memories (FeRAM), amplifiers, thermal imaging and non volatile memories. Because of their high remnant polarization and low coercive field, the 1.0 mol % Nb doped PZT films are good candidates for FERAM applications [6].

The aim of this study was to produce Nb doped PZT thin films by solution deposition method and then investigate the effects of Nb^{+5} ion addition on the structural, dielectric and ferroelectric properties. This was done by firstly preparing a homogeneous solution and then forming a crack free and smooth film on a substrate. The composition of the solution was taken as Nb:Zr:Ti=x/53/47, where x is Nb content of the material. All of the compositions were taken on the morphotropic phase boundary on the PNZT phase diagram.

The PNZT films were expected to have low processing temperatures compared to the bulk counterparts. High remnant polarization, small coercive field and low leakage current characteristics are achieved in PNZT thin films.

This thesis is composed of five chapters. It begins with literature survey of PNZT thin films. First, general information about ferroelectric and dielectric properties of materials were given to explain the important parameters that were used during the entire study. Then, ferroelectricity concept and perovskite structure were explained in accordance with PNZT system. In the last part of chapter 2, production of PNZT thin films by chemical solution deposition method was covered. Chapter 3 consists of experimental procedure, solution preparation, coating, heat treatment and characterization of the films. Chapter 4 discusses the results of film deposition, optimization of sintering parameters, X-ray studies (XRD), morphology, optimization of thickness and Nb content and finally electrical characterization of the films. Conclusions and further suggestions were presented in chapter 5.

CHAPTER 2

LITERATURE SURVEY

2.1 PNZT Materials

Lead zirconate titanate (PZT) thin films that have a composition $Pb(Zr_{0.53}Ti_{0.47})O_3$ near the morphotropic phase boundary have been investigated extensively in the recent years [4, 7]. They have been used in ferroelectric memory applications and micro-electro-mechanical systems (MEMS) [5, 8-10]. The most common applications of PZT and niobium doped PZT thin films are accelerometers, ferroelectric random access memories (FeRAM), amplifiers, thermal imaging and non volatile memories.

2.2 Dielectric Properties of Materials

2.2.1 Dielectric Properties

Dielectric materials are insulators, since they do not conduct electricity. They exhibit electric dipole structure, so that there is a separation of positive and negative electrically charged entities on a molecular or atomic layer [11]. Dielectric constant (relative dielectric constant or relative permittivity) is the ratio of the amount of stored electrical energy when a potential is applied relative to permittivity of vacuum.

Capacitance of a dielectric material can be defined as the quantity of charge stored on either plate Q per unit voltage V applied for a parallel plate capacitor.

$$C \text{ (Farad)} = Q \text{ (Coulomb)} / V \text{ (Volt)} \qquad \text{Eq. [2.1]}$$

If there is vacuum present between the plates for a parallel plate capacitor, the capacitance is equal to

$$C = \frac{\varepsilon_0 \times A}{d} \qquad \text{Eq. [2.2]}$$

where ε_0 is the permittivity of vacuum, A represents the area of the plates and d is the distance between the plates. The equation changes when a dielectric material is inserted between the plates as;

$$C = \frac{\varepsilon \times A}{d} \qquad \text{Eq. [2.3]}$$

where ε is the permittivity of the dielectric medium. Relative dielectric constant (ε_r) is the ratio of permittivity of medium to permittivity of vacuum and it is always greater than unity.

$$\varepsilon_r = \frac{\varepsilon}{\varepsilon_0} \qquad \text{Eq. [2.4]}$$

The polarization P (coulomb/m^2) that is induced in an insulating, polarizable material (a dielectric) by an applied electric field E (volt/meter) is given by:

$$P = \chi \times E \qquad \text{Eq. [2.5]}$$

where χ (farad/meter) is the dielectric susceptibility of the material. Equation [2.5] is valid only for linear materials or in a linear limit for nonlinear materials and, in general, P depends on higher-order terms of the field. The total surface charge density that is induced in the material by the applied field is given by the dielectric displacement D (coulomb/m^2):

$$D = \varepsilon_0 E + P \qquad \text{Eq. [2.6]}$$

It follows from eq. [2.5] and eq. [2.6] that

$$D = \varepsilon_0 E + \chi E = \varepsilon_0 \delta E + \chi E = (\varepsilon_0 \delta + \chi)E = \varepsilon E \qquad \text{Eq. [2.7]}$$

where $\varepsilon = \varepsilon_0 \times \delta + \chi$ is the dielectric permittivity of the material and δ is Kronecker's symbol. For the most ferroelectric materials $\varepsilon_0 \times \delta << \chi$ and $\varepsilon \approx \chi$. In practice, the relative dielectric permittivity, $\varepsilon_r = \varepsilon / \varepsilon_0$, also known as the dielectric constant of the material, is often more used than the dielectric permittivity [12].

Therefore, we can get an equation:

$$D = \varepsilon_0 \times \varepsilon_r \times E \qquad \text{Eq. [2.8]}$$

Dielectric constant of the material can be written in terms of capacitance which is defined as charge stored in the material per unit voltage applied :

$$\varepsilon_r = \frac{D}{\varepsilon_0 \times E} = \frac{Q/A}{\varepsilon_0 \times V/d} \qquad \text{Eq. [2.9]}$$

Therefore,

$$Q = \varepsilon_0 \times \varepsilon_r \times \frac{A}{d} \times V = C \times V \qquad \text{Eq. [2.10]}$$

where

$$C = \varepsilon_0 \times \varepsilon_r \times \frac{A}{d} \qquad \text{Eq. [2.11]}$$

$$C_0 = \varepsilon_0 \times \frac{A}{d} \qquad \text{Eq. [2.12]}$$

and

$$\varepsilon_r = \frac{C}{C_0} = \frac{\varepsilon}{\varepsilon_0} \qquad \text{Eq. [2.13]}$$

In eq. [2.13], C_0 represents respective air capacitance, C is the material capacitance, V the voltage impressed across the cell.

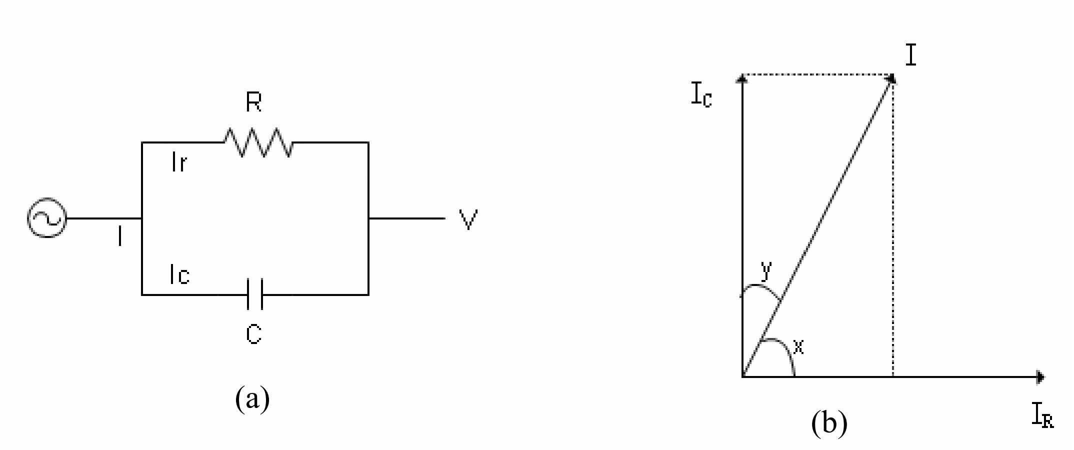

Figure 2.1 Equivalent circuit diagrams:**(a)** charging and loss current **(b)** loss tangent for a typical dielectric [13].

$$I_c = E\omega\varepsilon' C_0 \qquad \text{Eq. [2.14]}$$

$$I_R = E\omega\varepsilon'' C_0 \qquad \text{Eq. [2.15]}$$

In an ideal condenser of geometrical capacitance C_0, in which the polarization is instantaneous, the charging or capacitive current $E\omega\varepsilon' C_0$ is 90° out of phase with the alternating potential which can be seen in Figure 2.1. In a condenser in which absorptive polarization occurs, the current also has a component $E\omega\varepsilon'' C_0$ in phase with the potential and determined by Ohm's law. This ohmic or loss current, which measures the absorption, is due to the dissipation of part of the energy of the field as heat. In vector notation, the total current is the sum of the charging current and the loss current. The angle y (known as δ) between the vector for the amplitude of the total current and that for the amplitude of the charging current is the loss angle, and the tangent of this angle is the loss tangent

$$\tan\delta = -\text{(loss current)/(charging current)} = \frac{\varepsilon''}{\varepsilon'} \qquad \text{Eq. [2.16]}$$

where ε’ is the measured dielectric constant of the dielectric material in the condenser and ε’’ is its loss factor [14].

2.2.2 Polarization

To begin, for every dipole, there is a separation between a positive and a negative electric charge. An electric dipole moment p is associated with each dipole as follows:

$$\mathrm{p} = q \times d \qquad \text{Eq. [2.17]}$$

where q is the magnitude of each dipole charge and d is the distance of separation between them. In the presence of an electric field E, which is a vector quantity, a force (or torque) will come to bear on an electric dipole to orient it with the applied field; this phenomenon is illustrated in Figure 2.2. The process of dipole alignment is termed polarization [11].

There are three types of polarization: electronic, ionic and orientation. Dielectric materials ordinarily exhibit at least one of these polarization types depending on the material and also the manner of the external field application. Electronic polarization may be induced to one degree or another in all atoms. It results from a displacement of the center of the negatively charged electron cloud relative to the positive nucleus of an atom by the electric field. This polarization type is found in all dielectric materials, and, of course, exists only while an electric field is present [11].

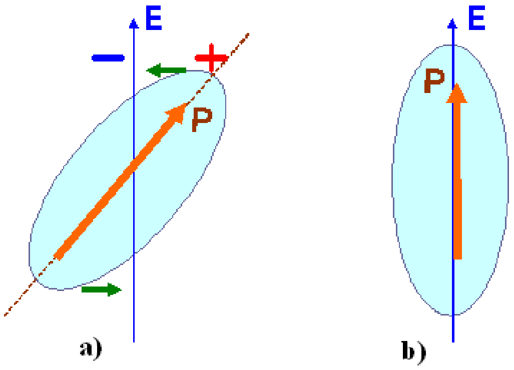

Figure 2.2 (a) Imposed forces (torque) acting on a dipole by an electric field. **(b)** Final dipole alignment with the field [15].

Ionic polarization occurs only in materials that are ionic. An applied field acts to displace cations in one direction and anions in the opposite direction, which gives rise to a net dipole moment. The magnitude of the dipole moment for each ion pair p_i is equal to the product of the relative displacement d_i and the charge on each ion, or

$$p_i = q \times d_i \qquad \text{Eq. [2.18]}$$

The third type, orientation polarization, is found only in substances that possess permanent dipole moments. Polarization results from a rotation of the permanent moments into the direction of the applied field. The alignment tendency is counteracted by the thermal vibrations of the atoms, such that polarization decreases with increasing temperature. The total polarization P of a substance is equal to the sum of the electronic, ionic and orientation polarizations (P_e, P_i and P_o, respectively) [11].

These three mechanisms of polarization are due to charges that are locally bound in atoms, in molecules, or in structures of solids and liquids. In addition, charge carriers usually exist that can migrate for some distance through the dielectric. When such carriers are impeded in their motion, either because they become trapped in the material or on interfaces, or because they cannot be freely discharged or replaced at the electrodes, space charges and a macroscopic field distortion result. Such a distortion appears to an outside observer as an increase in the capacitance of the sample and may be distinguishable from a real rise of the dielectric permittivity. Thus we have to add to our polarization mechanisms a fourth one, a space charge polarization P_s. Assuming that these polarization mechanism act independently so we may write total polarizability P of a dielectric material as the sum of the four terms indicated above [16].

2.3 Ferroelectric Properties of Materials

2.3.1 Ferroelectric Phenomena

The group of dielectric materials called ferroelectrics exhibit spontaneous polarization, that is, polarization in the absence of an electric field. They are the dielectric analogue of ferromagnetic materials, which may display permanent magnetic behavior [11].

Ferroelectrics are a special group of advanced electronic materials consisting of dielectrics which are spontaneously electrically polarized and possess the ability to switch their internal polarization with an electric field. These two specific characteristics, in fact, make up the definition of a ferroelectric; and experimental evidence for both of them rests in the ability to generate a hysteresis loop (polarization vs. electric field). A typical hysteresis loop is shown in Figure 2.3. The remnant states ($+P_r$ and $–P_r$) are produced by electrically switching the ferroelectric with ever increasing positive and negative electric fields greater than its coercive field (E_c). During the switching or looping process, the positive ions (Zr^{4+}, Ti^{4+}) in the microscopic unit cells take up stable alternate positions, thus producing a positive dipole on every other half cycle. Either of these two polarization states are permanent (neglecting aging effects) unless the material is subjected to external mechanical, electrical or thermal stimuli which are sufficiently large to alter them. The procedure of producing a permanent + or – polarization state in a ferroelectric material is commonly referred to as poling [1].

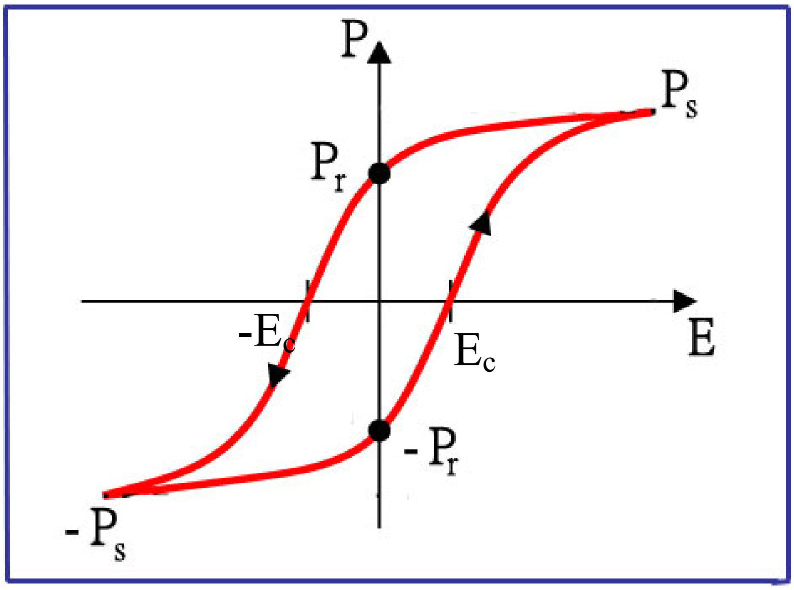

Figure 2.3 Typical hysteresis loop for a ferroelectric material [17].

Ferroelectrics are also unique among the family of materials because, individually and collectively, they possess a large number of combined and useful properties found in nature such as;

(a) Mechanical
(b) Electrical
(c) Optical
(d) Piezoelectric (stress/strain dependent polarization)
(e) Pyroelectric (temperature dependent polarization)
(f) Ferroelectric (electric field dependent polarization)

(g) Electrooptic (electric field dependent optical birefringence)

These properties are especially useful since they are highly sensitive to external stimuli, and hence, useful for devices in bulk, thick and thin film forms [1].

A material is ferroelectric if it has a spontaneous polarization P_s which can be reversed in sense or reoriented by the application of an electric field larger than the coercive field. Most ferroelectric materials undergo a structural phase transition from a high temperature nonferroelectric (or paraelectric) phase into a low temperature ferroelectric phase as shown in Figure 2.4 [12].

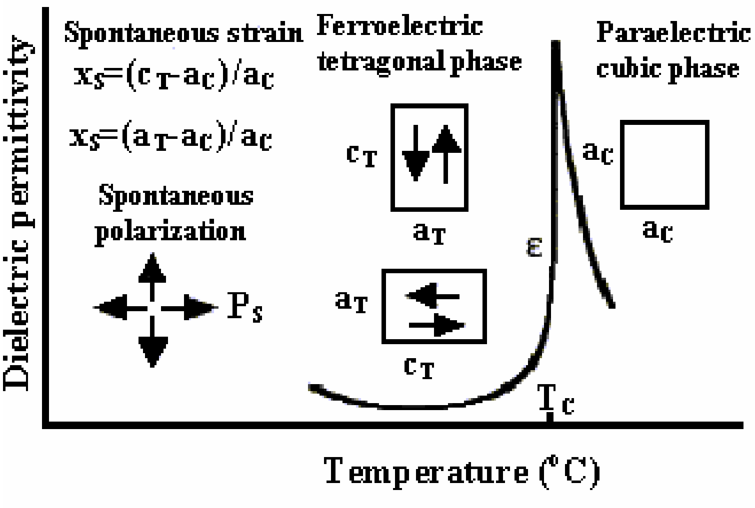

Figure 2.4 Illustration of changes in a ferroelectric material which transforms from a paraelectric cubic into ferroelectric tetragonal phase with temperature [12].

The symmetry of the ferroelectric phase is always lower than the symmetry of the paraelectric phase. The temperature of the phase transition is called the Curie point, T_C. Above the Curie point the dielectric permittivity falls off with temperature according to the Curie-Weiss law

$$\varepsilon = \varepsilon_0 + \frac{C}{T - T_0} \approx \frac{C}{T - T_0} \qquad \text{Eq. [2.19]}$$

where C is the Curie constant, T_0 ($T_0 \le T_C$) is the Curie-Weiss temperature [13].

2.3.2 Ferroelectric Materials

Historically, the first ferroelectric composition deposited as a thin film on a supporting substrate consisted of thermally evaporated barium titanate. This is understandable since barium titanate was the first oxide ferroelectric material discovered and remains to this day the most researched of all the ferroelectrics. Since that time (1969), a large number of ferroelectrics with a variety of properties and phenomena have been discovered or synthesized, and a number of these have been fabricated in thin film form. Table 2.1 lists the most popular ferroelectric compositions of current use along with a number of suitable common substrates. This priority listing shows that, to date, the overwhelming ferroelectric composition of choice is PZT and all of its many variations including PLZT [1].

A choice of substrate is often dictated by the particular ferroelectric, material which is being deposited. Considerations here are;

- Chemical compatibility at deposition and/or sintering temperatures
- Thermal expansion compatibility
- Lattice matching for epitaxy
- Process compatibility
- Optical transparency
- Availability
- Cost

Table 2.1 Ferroelectric compositions and substrates in common use [1].

Composition	**Substrates**
PZT	Si
PLZT	Sapphire
$LiNbO_3$	MgO
$BaMgF_4$	$SrTiO_3$
SBN	Metal foils
$Bi_4Ti_3O_{12}$	GaAs
$KNbO_3$	PLZT
$Pb_5Ge_3O_{11}$	$LiNbO_3$
PMN-PT	Fused silica
$BaTiO_3$	ZrO_2
PScT	Glass
KTN	
SKN	
PSKNN	

2.3.3 Ferroelectric Properties

Ferroelectric thin films, like bulk materials, possess a given set of properties relatable to their composition and microstructure; but unlike them, they possess another set of properties derived from their proximity and interaction with the supporting substrate (diffusion/buffer layer, epitaxy, internal stresses). These latter factors are very important and often control the behavior of the film when in use. In particular, the stress/strain conditions in the films and those to which the film is subjected during use are critical to its survival (fatigue, endurance); and as a rule, the less stress there is, the better is the performance of the film [1].

Like the bulk materials, the specific properties of the films depend primarily on composition and processing. In general, it has been noted that the properties of the thin film and thick films are quite similar to those of the bulk materials. Speaking specifically for the PZT and PLZTs, dielectric constants may vary from 100 to 2000, remnant polarizations from 5 to 40 $\mu C/cm^2$, and coercive fields (E_c) from 30 to 150 kV/cm, depending on the composition, grain size, substrate and electrodes used. Of these, only E_c is consistently higher in thin films than in the bulk; i.e., corresponding E_c values for bulk material range from 3 to 35 kV/cm. It has been also noted that as the films ranged from thin to thick, there is a decrease in E_c, as expected. This behavior is largely attributed to the mechanical clamping of the films by the substrate [1].

2.3.4 Ferroelectric Domains and Poling

PNZT materials have a perovskite structure which has the general formula ABO_3. In PZT, Ti^{4+} or Zr^{4+} ions are located at the body center position of the tetragonal unit cell. These ions are displaced from their positions up or down along c_T-axis of the tetragonal unit cell. This shift causes spontaneous polarization of the PZT material at temperatures lower than the Curie temperature. A dipole moment is created because the Ti^{4+}/Zr^{4+} ion is displaced from its equilibrium position with respect to lead and oxygen ions. These uniform dipole moments which are aligned in the same direction creates domains and the region between two domains is called the domain wall. The walls which separate regions with mutually perpendicular polarization are called 90° walls and those which separate domains with oppositely oriented polarization are called 180° walls.

When there is no electric field, there is no spontaneous polarization since the dipole moments in the domains are aligned randomly. Figure 2.5 shows the stages of a ferroelectric material when there is no electric field and electric field applied to the material. When an electric field is applied the domains are oriented in the same direction by the movement of domains and the material will have a net spontaneous polarization. After the electric field is removed some of the dipole moments remain in their aligned position. The remaining polarization when the electric field is removed is called the remnant polarization.

One consequence of the domain-wall switching in ferroelectric materials is the occurrence of the ferroelectric hysteresis loop that is shown in Figure 2.6. The hysteresis loop can be observed experimentally by using a Sawyer–Tower circuit. At small values of the AC electric field, the polarization increases linearly with the field amplitude. This corresponds to segment AB in Figure 2.6. In this region, the field is not strong enough to switch domains with the unfavourable direction of polarization [12].

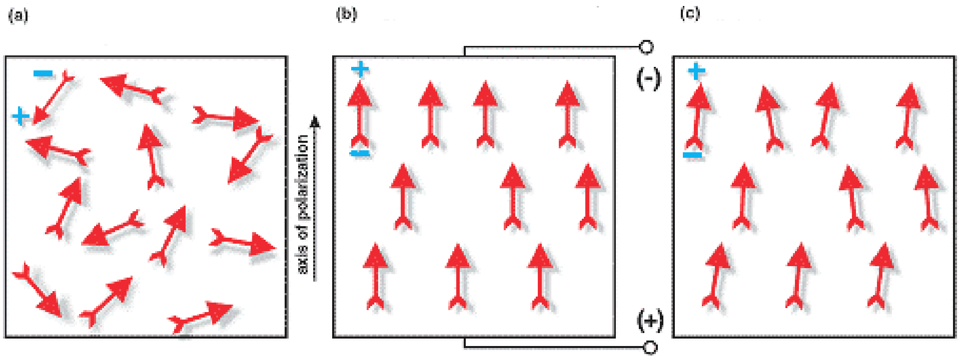

Figure 2.5 (a) Random polarization of polar domains prior to polarization, **(b)** polarization in DC electric field, **(c)** Remnant polarization after electric field removed [18].

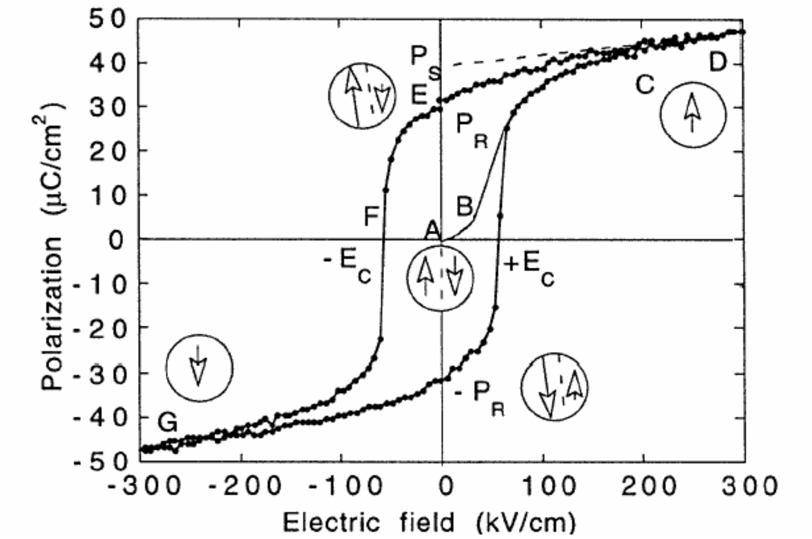

Figure 2.6 Ferroelectric (P-E) hysteresis loop. Circles with arrows represent the polarization state of the material at the indicated fields [12].

As the field is increased the polarization of domains with an unfavourable direction of polarization will start to switch in the direction of the field, rapidly increasing the measured charge density (segment BC). The polarization response in this region is strongly nonlinear. Once all the domains are aligned (point C) the ferroelectricity again behaves linearly (segment CD). If the field strength starts to decrease, some domains will back-switch, but at zero field the polarization is nonzero (point E). To reach a zero polarization state the field must be reversed (point F). Further increase of the field in the negative direction will cause a new alignment of dipoles and saturation (point G). The field strength is then reduced to zero and reversed to complete the cycle. The value of polarization at zero field (point E) is called the remnant polarization, P_r . The field necessary to bring the polarization to zero is called the coercive field, E_c . The spontaneous polarization P_s is usually taken as the intercept of the polarization axis with the extrapolated linear segment CD. An ideal hysteresis loop is symmetrical so that $+E_c = -E_c$ and $+P_r = -P_r$. The coercive field, spontaneous and remnant polarization and shape of the loop may be affected by many factors including the thickness of the film, the presence of charged defects, mechanical stresses, preparation conditions, and thermal treatment [12].

2.3.5 Ferroelectric Thin Films

From the 1970s the mainstream of the memory activities was taken over by silicon based Random Access Memories (RAM) and Read Only Memories (ROM) such as Dynamic RAM (DRAM), Static RAM (SRAM), Electrically Programmable ROM (EPROM), Electrically Erasable Programmable ROM (EEPROM) etc., which offer a high performance at low costs and a great compactness. It should be noted that the non-volatile memories (EPROM, EEPROM) have much lower write speed and a limited number of allowed write cycles as compared with their volatile counterparts (DRAM, SRAM). In the late 1980s the interest in ferroelectric memory applications was renewed, but now as a part of a silicon based memory cell. By using films of submicron thickness the switching threshold can be reduced to a level below the standard IC supply voltages. The marriage of thin film ferroelectric film technology with the silicon based memory technology offers the potential of combining nonvolatility with the fast read and write characteristics of a DRAM as well as the small cell size of this memory. As a non-volatile memory the ferroelectric memory has some superior characteristics, in particular a faster writing and a better write endurance, over the existing ones (e.g. EEPROMs) [19].

In 1990s, the trend of using three-dimensional or bulk sensor or device elements for future electronic devices is shifting toward the two- and one- dimensional geometry of sensor material. The effects of dimensionality in relation to optoelectronic properties and applications, emerging technological materials research in the sensor area, and the incorporation of ferroelectric materials and thin film technology with semiconductor technologies have opened new avenues for future ferroelectric applications and devices. As a result, the ferroelectric thin film has become an area of attention for the last ten years [1].

The most important factor in the use of ferroelectric thin films is the voltage necessary to switch the polarization state of the ferroelectric materials which is highly dependent on the thickness of the material. As the thickness decreases, the voltage, which is necessary to reverse the polarization vector also decreases. To be able to use a ferroelectric material in an integrated circuit efficiently, the switching voltage must be less than 5 volt and to achieve this voltage a ferroelectric thin film must have thickness less than 1 micron. Figure 2.7 shows graph of switching voltage versus film thickness. Kay and Dunn predict that switching voltage is proportional to $d^{2/3}$, where d is the film thickness. Minimum switching voltage is observed for the 250 nanometer film thickness as seen in the figure. After this point, voltage increases as thickness decreases. The switching speed also depends on the film thickness and proportional to $d^{-2/3}$. Scott and de Aruba reported that films having a thickness of 100 nanometer are 8 times faster than 400 nanometer film [20].

The dielectric and ferroelectric properties of PNZT thin films studied in the literature are listed in Table 2.2.

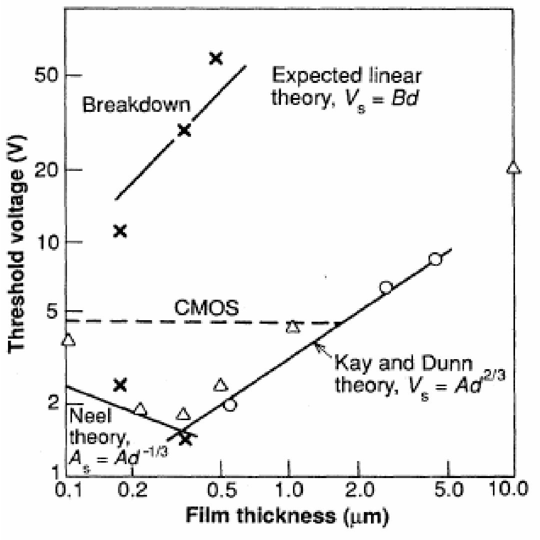

Figure 2.7 Switching voltage versus film thickness demonstrating the necessity of the films [20].

Table 2.2 The dielectric and ferroelectric properties of PNZT thin films studied in literature.

Ref. No	Production Technique	Composition (Nb/Zr/Ti)	Sintering Temperature (°C)	Dielectric Constant (ε_r)	Tangent Loss (%) (tanδ)	P_r (μC/cm^2)	E_c (kV/cm)	Film Thickness (nm)	Substrate
[21]	R. F. magnetron sputtering	2/54/46	625	1100	2.2	34	38	800	(111)-Pt/Ti/SiO_2/Si-(100)
[6]	Polymeric precusor method, spin coating	5/40/60	700	800	7.0	39	119	-	(111)-Pt/Ti/SiO_2/Si-(100)
[4]	Sol-Gel process, spin coating	2/53/47	600	780	5.0	19	50	500	(111)-Pt/Ti/SiO_2/Si-(100)
[7]	Sol-Gel process, spin coating	2/53/47	650	700-750	-	25	80-100	300	Si/BPSG/Ti/Pt
[9]	Sol-Gel process, spin coating	2/53/47	550	940	4.0	-	-	800	Pt/Ti/SiO_2/Si/Si_3N_4
[5]	Sol-Gel process, spin coating	4/53/47	600	-	-	24	8	260	(111)-Pt/Ti/SiO_2/Si-(100)
[22]	Sputtering	2/54/46	625	1100	1.8		18	700	(111)-Pt/Ti/SiO_2/Si-(100)

2.4 The Perovskite Structure and PNZT System

Lead zirconate titanate (PZT) has a perovskite crystal structure. Perovskite crystals has a general formula ABO_3, where A represents a cation with a larger ionic radius, and B (Zr or Ti) represents a cation with a smaller ionic radius and O is oxygen. Figure 2.8 shows the perovskite structure which contains six oxygen atoms that form an octahedral cage. Inside this cage, there is a smaller ion resides in B site which is Ti^{4+} or Zr^{4+}. At the corners of the unit cell, there are 8 Pb^{2+} ions. This is called the A site. To maintain electrical neutrality, some of the A and B sites are vacant because of the difference of valency between A and B atoms.

At temperatures higher than the ferroelectric Curie temperature (T_C) of PZT, the unit cell becomes cubic and paraelectric since cubic structures are centrosymmetric. Figure 2.8 shows the units cell of PZT different temperatures. As the temperature is decrease below the Curie temperature, unit cell becomes noncentrosymmetric, thus showing a ferroelectric behavior.

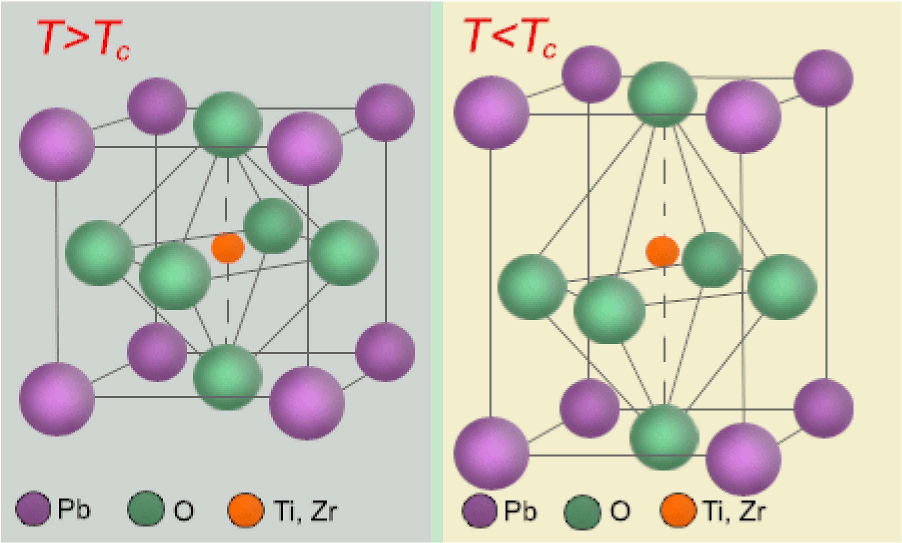

Figure 2.8 The perovskite crystal structure ABO_3 – A:Pb B:Zr,Ti [23].

Nb^{5+} ion substitutes for B site ions that are Zr^{4+} or Ti^{4+} acting as a donor. For every two atoms of Nb^{5+} ion introduced into the lattice, one lead vacancy occurs to maintain charge neutrality. The unit cell of a PNZT material is shown in Figure 2.9.

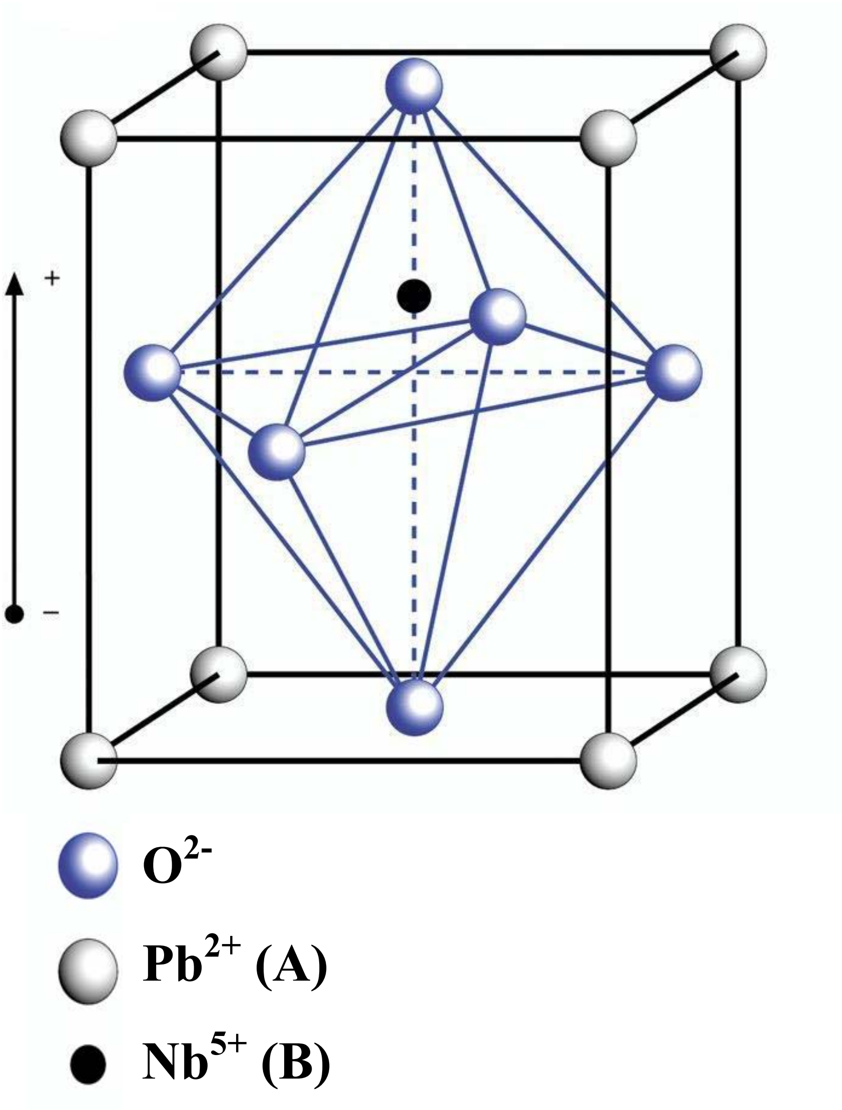

Figure 2.9 Perovskite ABO_3 crystal structure of PNZT [24].

The phase diagram of PZT is shown on Figure 2.10. At high temperatures the unit cell has a cubic structure which is paraelectric. On cooling below the Curie point line, the structure undergoes a transition to form a rhombohedral or tetragonal structure depending on the composition.

As shown in Figure 2.11 most physical properties such as dielectric constant shows an anomalous behavior at the morphotropic phase boundary (MPB). The MPB separating the two ferroelectric tetragonal and orthorhombic phases has a room temperature composition with a Zr/Ti ratio of ~ 52/48. PZT ceramics with the MPB composition show excellent electrical properties.

This MPB region, initially settled for ratios *x*≈50 mol% Ti, separates both phases, tetragonal from rhombohedric. As a matter of fact, the MPB region was understood as resulting of the coexistence between the tetragonal and rhombohedral phases, and this would explain the well known PZT's improved properties around that region [25].

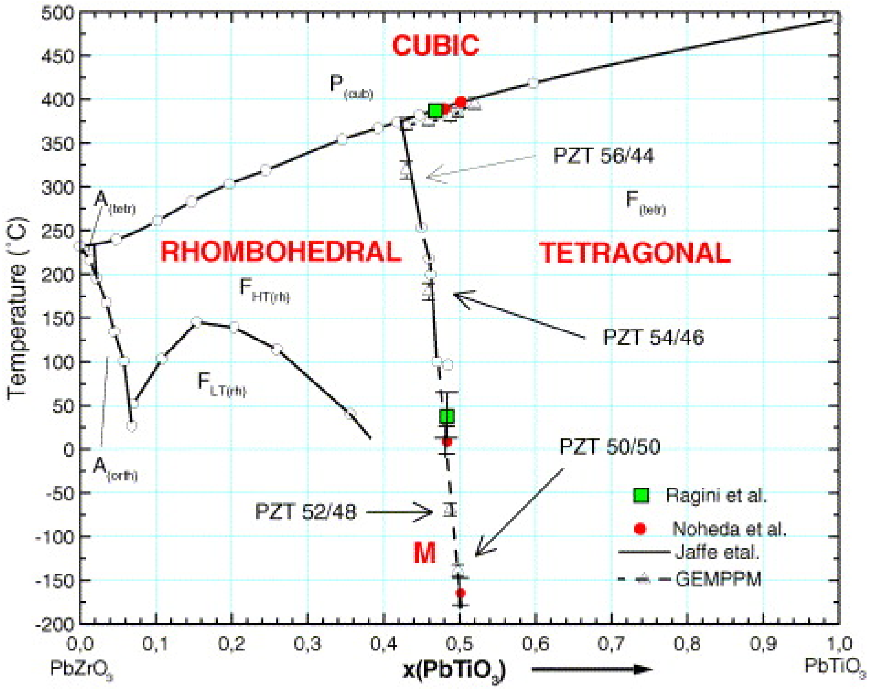

Figure 2.10 Phase diagram of Lead Titanate Zirconate (PZT) [26].

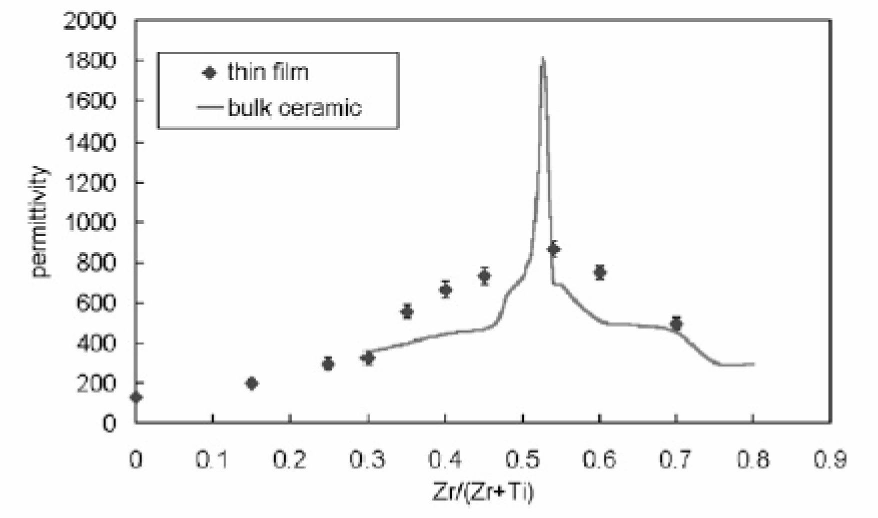

Figure 2.11 Evolution of ε_r function of the Zr/Ti ratio and comparison between bulk and thin film [21].

As the niobium incorporation occurs on the B-site, the compensation for the additional positive charge introduced (to achieve electroneutrality) is assumed through A-site, i.e. Pb site [22].

A general formula for the PNZT system can be given as

$$Pb_{1-x/2}\square_{x/2}[(Zr_{1-y}Ti_{y})_{1-x}Nb_{x}]O_{3} \qquad \text{Eq. [2.20]}$$

Since Nb^{5+} ion substitutes for Zr^{4+}/Ti^{4+}, charge balance is maintained by the creation of Pb^{2+} vacancies. One A-site vacancy (Pb^{2+}) is created with the addition of two Nb^{5+} ions.

2.5 Chemical Solution Deposition Technique (CSD)

Sol-gel processing of materials has been investigated for more than 100 years, but the use of related chemical solution deposition (CSD) techniques for the preparation of ferroelectric thin films is significantly more recent. The process involves the synthesis of a multicomponent solution that may be applied as a coating on a substrate, with the formation of the desired crystalline phase being induced by heat treatment [27].

The first step of any sol-gel process always consists in selecting the precursors of the wanted materials. It is the precursor that, by its chemistry, lead the reaction towards the formation of either colloidal particles or polymeric gels [28].

A sol is a suspension or dispersion of discrete colloidal particles or polymeric species in a solution while a gel is a colloidal or polymeric solid which has an internal network structure with mixed or highly dispersed solid and fluid components. Thus, there are two distinct types of sol-gel systems, namely polymeric and colloidal. In colloidal gels, electrolytic and steric effects in the precursor solution, or sol, determined gel formation, while in polymeric gels the relative rates and extents of chemical reactions (including polymerization) are important. Polymeric gels are formed from the three dimensional linkages (initiated by hydrolysis and polycondensation reactions) of complexed solutions containing the desired cations [29].

Polymeric sol-gel processing offers unique forming advantages. In particular, thin films can be deposited by spin-casting, dip-coating, or spraying appropriately hydrolyzed, alkoxide solutions containing the desired cations onto various substrates, including those of large or complex shapes. The amorphous gel films are then pyrolyzed at relatively low temperatures (300-700 °C) to form amorphous or crystalline oxides [29]. A variety of sol-gel technologies are given in Figure 2.12.

There are many advantages to sol-gel processing. It not only allows for materials to have any oxide composition, but it also permits the production of new hybrid organic-inorganic materials which do not exist naturally. Very pure products are obtained by simply purifying the precursors either by distillation, crystallization, or electrolysis. Moreover, the chemical processes of the first steps are always carried out at low temperatures. By comparison with the classical high temperature synthesis of conventional ceramics, this minimizes considerably the chemical interactions between the materials and the container walls. Another advantage is the association of the solid colloidal state with a liquid medium, thus avoiding any pollution by the eventual dispersion of dust [28].

There are other more fundamental advantages to sol-gel processing. For instance, the kinetics of the various chemical reactions can be easily controlled by the low processing temperatures and by the often dilute conditions. The nucleation and growth of the primary colloidal particles can also be controlled in order to give particles with a given shape, size and size distribution. The structure of sol-gel ceramics can be as easily controlled as the size of the particles. Sol-gel processing offers the most outstanding advantages for mixed oxides systems in which the chemical homogeneity of various elements can be controlled down to the atomic level [28].

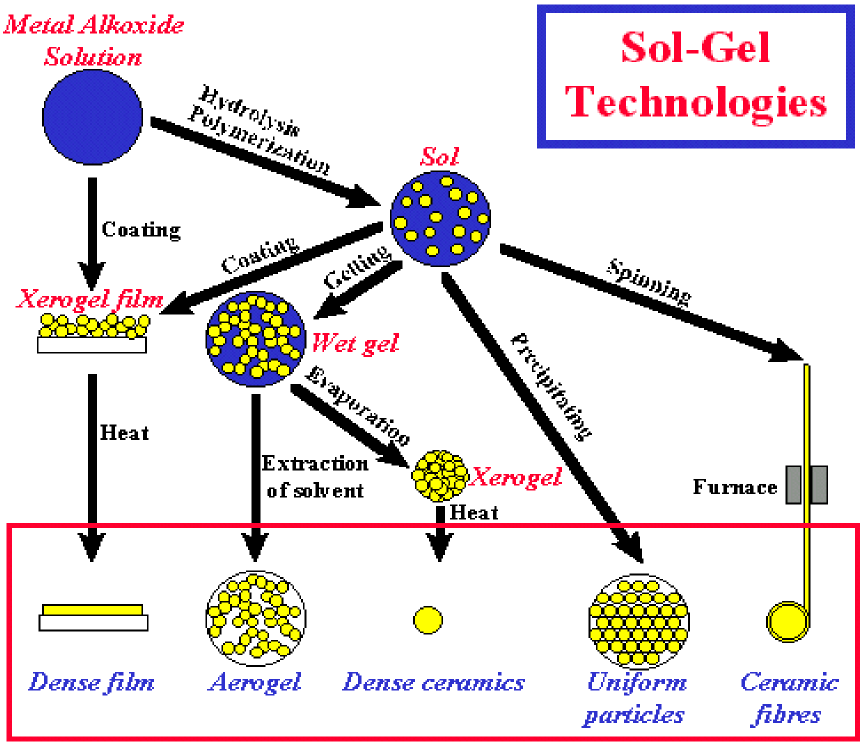

Figure 2.12 Categories of the sol-gel processing technique. The route at the left in the figure, called chemical solution deposition, was used in this study [30].

The greatest limitation to the synthesis of ceramic by sol-gel processing is still the cost of the precursors, and especially that of alkoxides. Most of these alkoxides are nonetheless quite easy to make; especially if they do not tend to polymerize [28].

2.5.1 Process Chemistry of Solution Deposition Processing

To fabricate multicomponent perovskite thin films, numerous metal organic precursors including alkoxides, carboxylates (ethyl hexanoates, propionates, and neodecanetes), diketonates, and various organic salts are used to form initially metal-complexed solutions. From a commercial viewpoint, alkoxides of most metals can be synthesized and are convenient starting materials with respect to availability and cost. Metal alkoxide (general formula of $M(OR)_n$, where M is a metal ion and R is an alkyl group) complexes are partially hydrolyzed by addition of less-than-stoichiometric quantities of water to produce a spin-casting solution. This hydrolysis step must be controlled so that precipitation is avoided while polymerization proceeds [29].

Metal oxides are members of the family of metallorganic compounds, which have an organic ligand attached to a metal or metalloid atom. Organometallic compounds are defined as having direct metal-carbon bonds, not metal-oxygen-carbon linkages as in metal alkoxides; thus alkoxides are not organometallic compounds, although that usage turns up frequently in the literature. Metal oxides; are popular precursors because they react with water. The reaction is called hydrolysis, because a hydroxyl ion becomes attached to the metal atom

$$M(OR)_x + H_2O \rightarrow M(OH)_x + xROH \qquad \text{Eq. [2.21]}$$

Two partially hydrolyzed molecules can link together in a condensation, such as

$$(OR)_{x-1}M - OH + HO - M(OR)_{x-1} \rightarrow (OR)_{x-1}M - O - M(OR)_{x-1} + H_2O \quad \text{Eq. [2.22]}$$

or

$$(OR)_{x-1}M - OR + HO - M(OR)_{x-1} \rightarrow (OR)_{x-1}M - O - M(OR)_{x-1} + ROH \quad \text{Eq. [2.23]}$$

These reactions cause the formation of a metal-oxygen-metal bridge, which constitutes the backbone of any oxide ceramics structure. Continued condensation leads to an increase in the density of metal-oxygen-metal crosslink's until eventually geletion or precipitation occurs [13].

Important and typical precursors for making sol-gel solutions are alkoxides of the general composition M(O-R)$_n$, where R is an alkyl radical (CH_3,C_2H_5, etc.). Their properties and reactions affect the preparation process and determine the product features. Inorganic and organic salts can also be used for introducing some oxides into multicomponent systems. The precursors are dissolved in a suitable organic solvent to form the solution. In order to get the solution with a high concentration of necessary components and proper viscosity, surface tension and boiling point, the solvent must be carefully selected. Table 2.3 summarizes the precursors and solvents used in the literature.

2.5.2 Spin Coating Process

A variety of techniques may be used to deposit the precursor solution onto the substrate, including spin and dip coating, and various other spray techniques, though for ferroelectric film fabrication, spin coating is the process that has been used almost exclusively. On a laboratory scale, deposition is usually carried out with a photoresist spinner and the substrate is typically either a single crystal oxide or an electroded silicon wafer. The substrate is held in place on the spinner and is typically "flooded" with solution. The wafer is then accelerated rapidly to 1000 rpm to 8000 rpm, with 3000 rpm being the most commonly used speed. The angular velocity and spinning time, together with the solution viscosity, can be used to control the thickness of the wet film [27].

A variety of defects can arise at this processing stage. Simple defects, such as dust or airborne particulates, may be incorporated in the films, although the density of these defects may be reduced by the use of a clean room or clean tent. Another defect that may arise during deposition is striation formation (i.e., thickness variations) within the layer [27].

Table 2.3 Literature review of precursors and solvents that were used for the production of PNZT thin films.

Ref No	Precursors	Solvents	Substrate
[31]	Lead acetate trihydrate, titanium butoxide, Zr acetate and lead acetate, Nb ethoxide	Acetylacetone, 2-methoxyethanol	(111)-Pt/Ti/SiO_2/Si-(100)
[32]	Lead 2-ethylhexanoate, Zr tetra-n-butozide,Ti tetraisopropozide, Nb pentaethoxide	-	Pt coated SiO_2/Si
[33]	Zr butoxide-butanol, titanium isopropoxide, lead (IV) acetate, Nb ethoxide	Methanol, Acetic acid	(111)-Pt/Ti/SiO_2/Si-(100)
[10]	Lead acetate trihydrate, Ti iso-propoxide, Zr n-buthoxide, Nb pentaethoxide	Ethanol, Acetylacetone	(111)-Pt/Ti/SiO_2/Si-(100)
[7]	Lead acetate trihydrate, Zr n-propoxide, Ti isopropoxide, Nb ethoxide	2-methoxyethanol	Si/BPSG/Ti/Pt
[4]	Lead acetate trihydrate, Nb (V) ethoxide, Ti diisopropoxide bisacetylacetone, Zr n-propoxide	1.3 propanediol, Acetylacetone	(111)-Pt/Ti/SiO_2/Si-(100)
[34]	Ti (IV) isopropoxide, Zr-tetra-n-butoxide, Lead acetate trihydrate,	Citric acid, NH_4OH, ethylene glycol	Pt/Ti/SiO_2/Si-(100)

Striations typically appear as radial patterns originating at the center of the substrate and are associated with phase segregation during the drying stage of spin casting. Other film processing characteristics that are controlled through manipulation of solution chemistry include substrate wetting and film cracking [27].

Film thickness for most common CSD processes is usually in the range of 0.05 to 0.1 μm per coating, although thinner layers have also been prepared by using more dilute solutions and/or higher spinning rates. For the preparation of thicker coatings, a multilayer approach is often used. In practice, this means the deposition of multiple (usually three or four) layers, with a pyrolysis step after each layer, followed by crystallization anneal. Films with thicknesses in excess of 10 μm have been prepared by this technique, though some investigators have developed automated dip-coating procedures to achieve the same goal while reducing the manual labor associated with this type of repetitive procedure [27].

Bornside et. al. [35] indicated that there are four distinct stages of spin coating process that is shown on Figure 2.13. Flow controlled (Stage 3) and evaporation controlled (Stage 4) stages the two stages that have the most effect on final coating thickness.

Deposition of the coating fluid onto the wafer or substrate is the first stage of the spin coating process. It can be done using a nozzle that pours the solution out, or it could be sprayed onto the surface, etc. Usually this dispense stage provides a substantial excess of coating solution compared to the amount that will ultimately be required in the final coating thickness. The second stage is when the substrate is accelerated up to its final, desired, rotation speed. This stage is usually characterized by aggressive fluid expulsion from the wafer surface by the rotational motion. The third stage is when the substrate is spinning at a constant rate and fluid viscous forces dominate fluid thinning behavior. This stage is characterized by gradual fluid thinning. The fourth stage is when the substrate is spinning at a constant rate and solvent evaporation dominates the coating thinning behavior. As the prior stage advances, the fluid thickness reaches a point where the viscosity effects yield only rather minor net fluid flow. At this point, the evaporation of any volatile solvent species will become the dominant process occurring in the coating. In fact, at this point the coating effectively "gels" because as these solvents are removed the viscosity of the remaining solution will likely rise [13].

The prediction of Mayerhofer about factors affecting the film thickness includes the spin rate (f), the initial viscosity (η_i), and the evaporation rate (e):

$$h \,\alpha\, f^{2/3} \eta_i^{1/3} e^{1/3} \qquad \text{Eq. [2.24]}$$

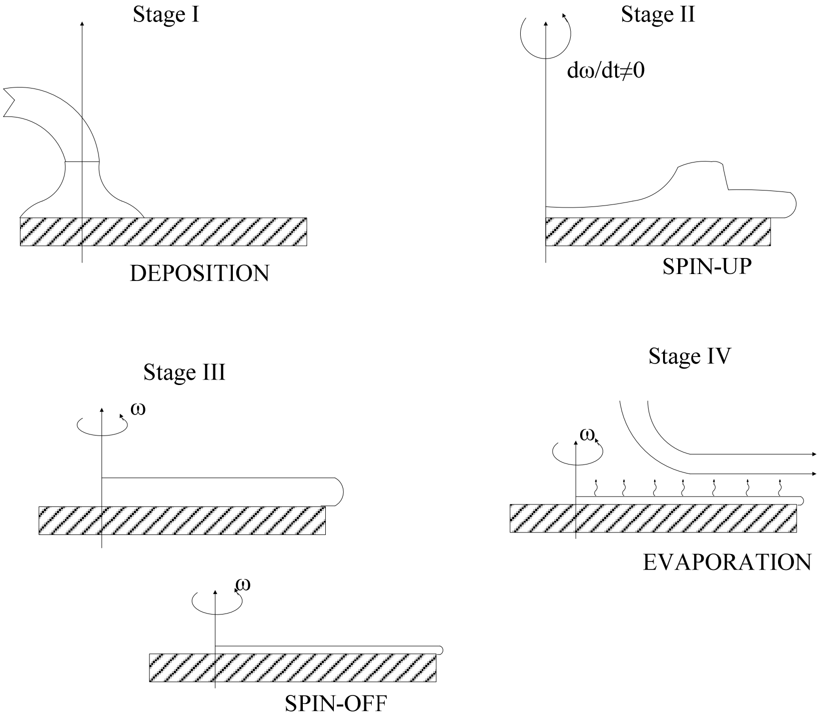

Figure 2.13 Stages of spin coating process [35].

2.5.3 Drying, Firing and Sintering of PNZT Thin Films

As the beginning step drying of the films were done after the coating of the films. In this stage water an solvent in the solution is removed. There are some stages occurring during drying process. In the first stage called constant rate period, liquid flows to the surface to replace that which is lost to evaporation. This is the stage where the most shrinkage and warping occurs as a result of capillary pressure differentials within the film. The gel matrix reaches a point called critical point where it can no longer shrink to release the solvent necessary to reduce the capillary pressure. At this point the liquid meniscus enters the matrix and drying from within the film begins. This is when a crack is the most likely to appear in the material. In the first falling rate period, the last layers of solvent are removed by flow along the pores walls to the surface. During second falling rate period, the volatized solvent is removed by the diffusion of vapor to the surface.

The timing of these stages is intimately linked to the structure of the film. Cracking is the most important subject that should be considered during the drying. The gel consists of two phases, the network solid phase and connected pores filled with liquid phase. Initially the surface of the gel is covered with liquid phase. The liquid phase evaporates so that the solid phase is exposed. Since the solid network is wetted by the liquid phase, the liquid phase tends to cover all the solid surface capillary force will be imposed on the solid network. Since the gel network is compliant, the gel shrinks under capillary force as the liquid evaporates [36].

Conversion of the as deposited film into the crystalline state has been carried out by a variety of methods. The most typical approach is a two-step heat treatment process involving seperate low-temperature pyrolysis (~300 to 350 °C) and high-temperature (~550 to 750 °C) crystallization sintering process. The times and temperatured utilized depend upon precursor chemistry, film composition, and layer thickness. At the laboratory scale, the pyrolysis step is most often carried out by simply placing the film on a hot plate that has been preset to the desired temperature. Nearly always, pyrolyis condisitons are chosen based on thermal decomposition behavior of powders derived from the same solution chemistry. Thermal gravimetric analysis (TGA) is normally employed for these studies, and while this approach seems less than ideal, it has proved reasonably effective [27].

In the second phase of the standard two step heat treatment method, the pyrolyzed film, which is amorphous at this stage, is subjected to higher heat treatment temperatures for nucleation and growth into the desired crystalline structure. For PZT, BST and SBT, the temperatures typically utilized are 550 to 750 °C, and most investigators seem to have settled on a heat treatment period of 30 min, though both shorter and longer periods have been used. It is virtually certain that nucleation begins during the ramp to the crystallization temperature, with complete conversion to the final crystalline phase occuring during the longer hold period at the maximum temperature [27].

Heating rates typically range from 10 to 50 °C/min when a standard tube or box furnace is used for crystallization, to ~300 °C/s when RTA is used. Heating rates and the time and temperature of the crystallization anneal are known to play a role in the significance of transitory phases that are formed during the heat treatment. These phases may be compositionally related to the final film, as for the formation of fluorite during PZT processing, may be decomposition products, such as $BaCO_3$ in BT or BST processing, or may involve reaction with the lower electrode, such as formation of Pt_3-Ti or Pb-Pt_x in PZT processing on platinum electrodes [27].

2.6 Viscosity of PNZT solutions

The characateristic property for viscous flow, viscosity, is a measure of a noncrystalline material's resistance to deformation. For viscous flow in a liquid that originates from shear stresses imposed by two flat and parallel plates, the viscosity η is the ratio of the applied shear stress τ and the change in velocity $d\upsilon$ with distance dy in a direction perpendicular to and away from the plates, or

$$\eta = \frac{\tau}{d\upsilon / dy} = \frac{F / A}{d\upsilon / dy} \qquad \text{Eq. [2.25]}$$

The units for viscosity are poises (P) and pascal-seconds (Pa-s); 1 P = 1 dyne-s/cm^2, and 1 Pa-s = 1 N-s/m^2. Conversion from one system of units to the other is according to 10 P = 1 Pa-s.

For straight, parallel and uniform flow, the shear stress, τ, between layers is proportional to the velocity gradient, du/dy, in the direction perpendicular to the layers, in other words, the relative motion of the layers.

$$\tau = \mu \frac{\partial u}{\partial y} \qquad \text{Eq. [2.26]}$$

where the constant μ is known as the coefficient of viscosity, the viscosity, or the dynamic viscosity. Many fluids satisfy Newton's criterion and are known as Newtonian fluids. Non-Newtonian fluids exhibit a more complicated relationship between shear stress and velocity gradient than simple linearity. Newtonian and non-Newtonian behaviours of fluids are given in Figure 2.14. When the viscosity decreases with increasing shear rate, it is called the fluid shear-thinning. In opposite case where the viscosity increases as fluid is subjected to a higher shear rate, fluid is called shear-thickening [37].

The regions where the apparent viscosity is approximately constant are known as Newtonian regions. The behavior between these regions can usually be approximated by a straight line on these axes. It is known as the power-law region. In this region, we can approximate the behavior by

$$\log \eta = a + b \log \theta \qquad \text{Eq. [2.27]}$$

which can be rewritten as

$$\eta = K\theta^{b} \qquad \text{Eq. [2.28]}$$

where K=exp(a). Instead of b it is commonly used (n-1) for the exponent and written a result for the apparent viscosity as follows.

$$\eta = K\theta^{n-1} \qquad \text{Eq. [2.29]}$$

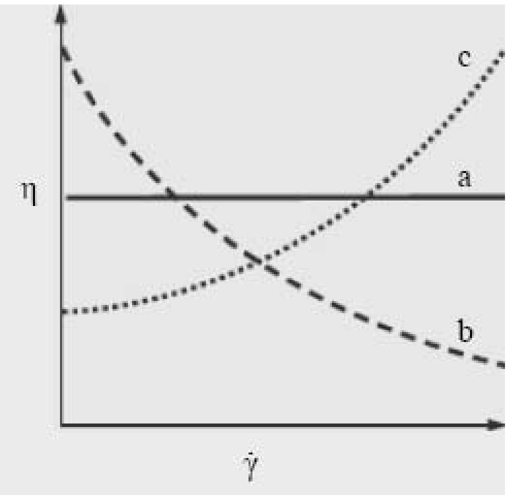

Figure 2.14 (a) Newtonian, **(b)** shear thinning and **(c)** shear thickening non-Newtonian behaviors [37].

Upon using the connection among the shear stress, apparent viscosity, and the shear rate, power-law model is obtained:

$$\tau = K\theta^{n} \qquad \text{Eq. [2.30]}$$

where n is called the power-law index. Note that n=1 corresponds to Newtonian behavior. Typically, for shear thinning fluids, n lies between 1/3 and ½, even though other values are possible [38].

Liquids have relatively low viscosities; for example, the viscosity of water at room temperature is about 10^{-3} Pa-s. On the other hand, glasses have extremely large viscosities at ambient temperatures, which is accounted for by strong interatomic bonding. As the temperature is raised, the magnitude of the bonding is diminished, the sliding motion or flow of the atoms or ions is facilitated, and subsequently there is an attendant decrease in viscosity [11].

CHAPTER 3

EXPERIMENTAL PROCEDURE

Solutions used to produce PNZT thin film were obtained with respect to the nominal compositions, $Pb_{(1-0.5x)}(Zr_{0.53}Ti_{0.47})_{1-x}Nb_xO_3$: $x = 0.00 - 0.07$. Compositions were chosen near morphotropic phase boundary (MPB) [Zr/Ti : 53/47] to boost the electrical and structural properties of the films. To obtain the final form of the film, solution preparation, coating and heat treatment processes were carried out, respectively.

3.1 Solution Preparation

3.1.1 Starting Materials

The starting materials used for preparing the precursors were lead acetate trihydrate $Pb(CH_3COO)_2.3H_2O$ (Aldrich Co., purity 99+%), titanium (IV) isopropoxide $Ti[(CH_3)_2CHO]_4$ (Aldrich Co., purity 97%), zirconium (IV) propoxide $Zr(C_3H_7O)_4$ (Aldrich Co., 70wt.% solution in 1-propanol), and niobium (V) ethoxide $Nb(OC_2H_5)_5$ (Aldrich Co., purity 99.95%). The solvent used during the study was 2-methoxyethanol $C_3H_8O_2$ (Aldrich Co., purity 99%). Deionized water was used as a diluting solvent.

3.1.2 Solution Preparation

To obtain a homogeneous solution with the desired composition, two different solutions were prepared and then mixed with each other. The concentration and the volume of the solutions were set to 0.4M and 40 mL. In the first solution, lead acetate trihydrate and 2-methoxyethanol were mixed. The temperature of the solution was increased to 90 °C to dissolve all of the lead acetate in the solvent in order to get a homogeneous solution. After stirring the solution for 30 min at that temperature, the solution was cooled to 60 °C. Niobium (V) ethoxide was added at this temperature and fluxed for 30 min. The reason for the addition of niobium (V) ethoxide at a temperature lower than 90 °C is to avoid precipitation at 90 °C. In the second solution, zirconium (IV) propoxide, titanium (IV) isopropoxide and 2-methoxyethanol were mixed at room temperature for 45 min. Then, two solutions were mixed with each other and refluxed at 75 °C for 2 h. The final solution was cooled to room temperature and then 2-methoxyethanol and deionized water were added to complete the solution to 40 mL. Finally, to obtain a homogeneous stock solution, the solution was stirred gently for 24 h at room temperature. The solution was kept as a stock and clear for a few months. The flow diagram of the PNZT solution preparation is shown in Figure 3.1.

The compositions were selected near morphotropic phase boundary. Zr/Ti ratio was taken constant as 53/47. Niobium content was taken between 0 and 7 at %. The selected compositions and the added Niobium content are listed in the Table 3.1.

Table 3.1 Table of compositions that were used during the study.

Nb content (Nb at %)	***Chemical Formula***
x = 0.00 (0%)	$Pb(Zr_{0.53}Ti_{0.47})O_3$
x = 0.01 (1%)	$Pb_{0.995}(Zr_{0.53}Ti_{0.47})_{0.99}Nb_{0.01}O_3$
x = 0.03 (3%)	$Pb_{0.985}(Zr_{0.53}Ti_{0.47})_{0.97}Nb_{0.03}O_3$
x = 0.05 (5%)	$Pb_{0.975}(Zr_{0.53}Ti_{0.47})_{0.95}Nb_{0.05}O_3$
x = 0.07 (7%)	$Pb_{0.965}(Zr_{0.53}Ti_{0.47})_{0.93}Nb_{0.07}O_3$

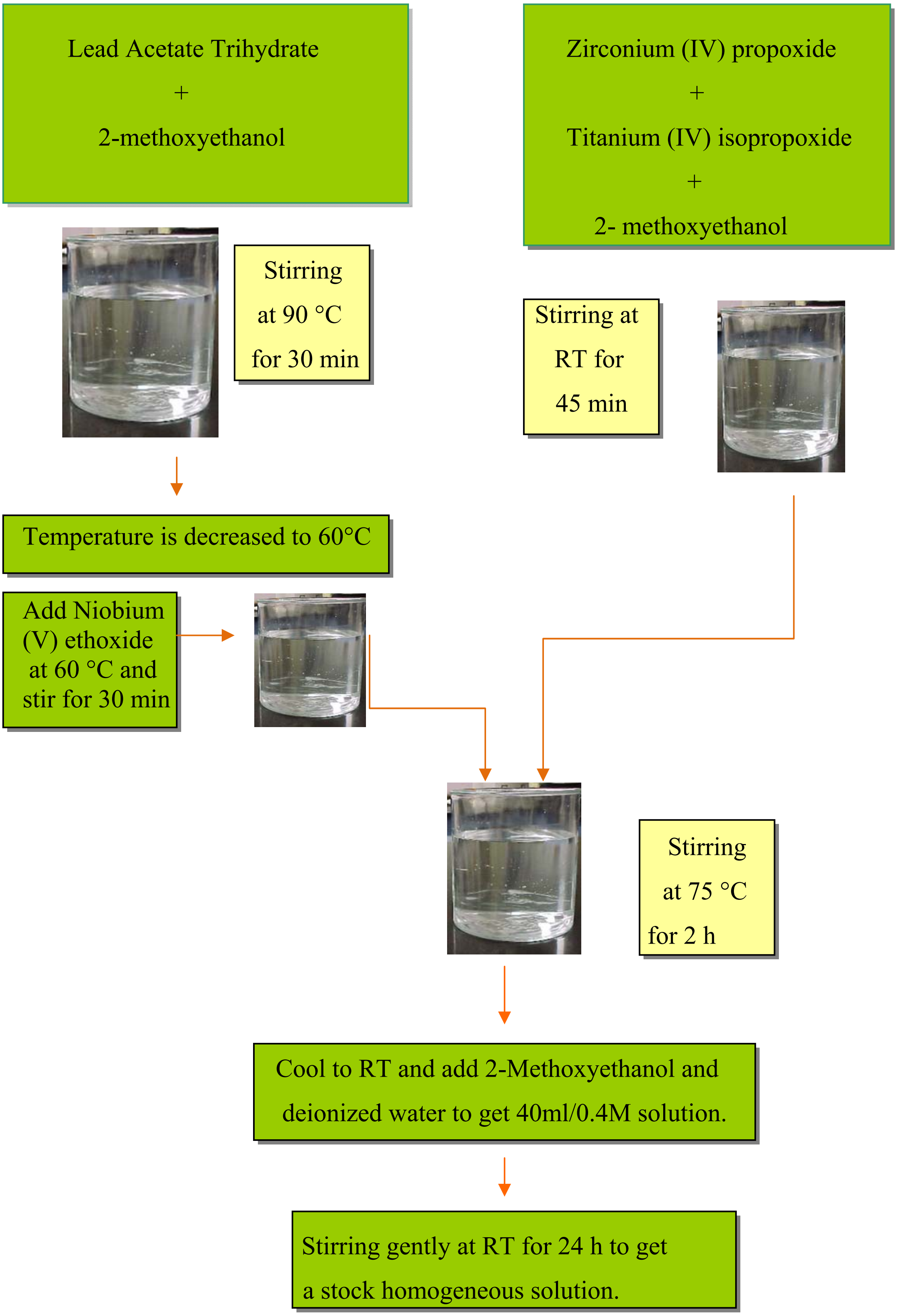

Figure 3.1 The flow diagram of solution preparation of PNZT thin films.

To produce a PNZT thin film with the composition $Pb_{0.995}(Zr_{0.53}Ti_{0.47})_{0.99}Nb_{0.01}O_3$ (Nb:Zr:Ti = 1/53/47), firstly the amount of lead acetate trihydrate was determined as 6.161 g. Then, it was dissolved in 9.304 g 2-methoxyethanol and the temperature was increased to 90 °C. The solution was stirred for 30 min until a homogeneous solution was achieved. Lead acetate trihydrate was taken 10% excess to compensate the losses during the sintering process. Then the solution was cooled to 60 °C to add the Nb (V) ethoxide and dissolve it completely at that temperature for 30 min. The calculated amount of Nb (V) ethoxide for 1 at % Nb doping was 0.047 g (37 μL). At the second solution, 3.306 g Zr (IV) propoxide and 2.152 g Ti (IV) isopropoxide were mixed with each other. The amount of Zr (IV) propoxide was taken 30% excess because of being a 70 wt. % solution. Also the amount of Ti (IV) isopropoxide was taken 10% excess since Ti is removed during the preparation of the solution. 18.607 g of 2-methoxyethanol was used as the solvent and the final solution was mixed at room temperature for 45 min. Finally, these two solutions were mixed at 75 °C. After getting a homogeneous solution at the end of 2 h of mixing, it was cooled to room temperature. Few milliliters of 2-methoxyethanol and deionized water were added to adjust the solution to 40 ml. The final solution was stirred gently for 24 h.

3.2 Coating of PNZT Thin Films on Substrates

3.2.1 Preparation of Substrates

All of the PNZT and PZT films were coated on (111)-Pt/Ti/SiO_2/Si-(100) substrates. The similarities in thermal expansion coefficients and lattice parameter make Pt a good choice for the bottom electrode [5]. Firstly, the substrates were cut from the wafers using a diamond glass cutter with the dimensions of 1.5 cm to 1.5 cm. Then they were rinsed in acetone using the ultrasonic cleaner for 15 min. The final prepared substrates had a surface with good adhesion and deposition to the films and also they were free of cracks and scratches. The substrates were cut in square shapes to coat the PNZT thin films homogeneously in a symmetrical way. The dimensions were selected as 1.5 cm to 1.5 cm because the probe that was used during testing of the films requires dimensions of minimum 1.2 cm^2. The specifications of the (111)-Pt/Ti/SiO_2/Si-(100) substrates are given in Table 3.2.

3.2.2 Spin Coating

The prepared substrates were positioned on the spin coater by double-sided tapes. Chemat Technology Spin Coater was used for the coating process. Excess amount of solution was dropped by using pasteur pipettes onto the substrates in order to coat whole surface of the substrates. Different speeds for different durations were performed with the spin coater and the optimum spinning rate was determined as 1500 rpm for 30 seconds. To achieve the required thickness, multiple coating-pyrolysis cycles were employed and single and multilayered films up to four layers have been produced.

Table 3.2 Specifications of (111)-Pt/Ti/SiO_2/Si-(100) substrate (INOSTEK Korea)

Substrate: Silicon Wafer	
Crystal Growth Method	CZ (Prime)
Orientation	<100>
Thickness (μm)	525 ± 20
SiO_2 Layer	
Film Growth Method	Thermal Oxidation
Thickness (nm)	3000
Ti Layer	
Film Growth Method	DC Magnetron Sputtering
Thickness (nm)	100
Pt Layer	
Film Growth Method	DC Magnetron Sputtering
Thickness (nm)	1500
Orientation	(111)

As the thickness of the films increases by the application of multiple coating steps, the possibility of crack formation increases. It was intended to produce a film that is going to be both thin and crack free. However, in order to measure the electrical properties, the films must have a minimum thickness value so that they can resist the applied voltages up to 15 V.

It was found that, eight-layered films (~1.5µm and coated at 1500 rpm for 30 sec) totally crack due to shrinkage of films during drying operation. The optimum thickness-layer combination was determined as 390 nm-double layered films.

3.2.3 Heat Treatment of PNZT Thin Films

Heat treatment of the films starts with the drying process. The films were placed inside the furnace at room temperature. Then the temperature was raised to 150 °C and kept at that temperature for 15 min for the removal of water. Then the films were fired at 450 °C in the preheated furnace for 15 min. At this pyrolysis stage, removal of organics takes place. The same procedure was repeated until the thickness of the films came to a desired value.

After the drying and pyrolysis steps, sintering process was performed. This step is critical because of the crystallization of the amorphous phase and the formation of other phases. Sintering temperature and time were selected as two important parameters in this study. They affect the ferroelectric and dielectric properties of the films because of the changes occurring in the film during the sintering process. The films were placed inside the furnace at room temperature. The furnace temperature was increased to the sintering temperature at a heating rate of 20 °C/min and it is cooled back to room temperature at a cooling rate of 15 °C/min after the process.

To understand the effects of sintering temperature and find the optimum temperature for sintering process, three different temperatures were chosen as 600, 650 and 700 °C. Also the sintering periods for the films were taken as 1, 2 and 3 h. All of the possible combinations were applied to find the optimum conditions for sintering.

The thickness and composition of the films were kept constant while changing the sintering period and temperature. Double layered (390 nm) PNZT thin films that had a composition $Pb_{0.985}(Zr_{0.53}Ti_{0.47})_{0.97}Nb_{0.03}O_3$ were used to find the optimum sintering parameters.

3.3 Characterization of PNZT Thin Films

3.3.1 Structural and Morphological Analysis

For the chemical and microstructural analysis of the films, JEOL JSM-6400 Scanning Electron Microscope (SEM) equipped with an Energy Dispersive Spectrometer (EDS analyser) was used. The surface and cross-section of the films were investigated by SEM to find out information about the composition, morphology and the thickness of the films. X-ray diffraction analysis was performed by using Rigaku (JAPAN) D/MAX 2200/PC Diffractometer between angles 20°- 60° (2θ) with Cu (K_α) radiation. Nikon Type 104 Stereo Microscope was used to investigate the surface cracks of the films and substrates. Surface characteristics of the films were measured by Nanosurf Easyscan 2 Atomic Force Microscopy (AFM) and surface profilometry. Grain size of the films was found using the SEM images obtained by FEI Quanta 400 FEG Field Emission Scanning Electron Microscope (FESEM).

3.3.2 Dielectric and Ferroelectric Measurements

Dielectric measurements of the PNZT thin films were carried out using Impedance Analyzer (Agilent 4294A). Dielectric constant (ε_r) and tangent loss (tanδ) values of the films were determined at the frequency range 1 kHz-500 kHz with an oscillation voltage of 0.05 V at room temperature. Mercury Probe Model 802B-200 was used for the measurements. Contact area was taken as 0.00454 cm^2. Capacitance-voltage (C-V) curves between -10 and 10 V and hysteresis curves [Polarization ($\mu C/cm^2$) – Electric field (kV/cm)] at 5, 10 and 15 V were measured by Radiant Ferroelectric Tester Precision LC (Radiant Technologies, Inc.).

3.3.3 Leakage Current Analysis

Leakage current analysis was carried out by the Radiant Ferroelectric Tester Precision LC (Radiant Technologies, Inc.) at ±10 V. Leakage current density (current/area) as a function of electric field (kV/cm) was obtained.

3.3.4 Differential Thermal Analysis (TG/DTA)

TG (thermogravimetry) and DTA (differential thermal analysis) analysis were done by Simultaneous Thermogravimetric Analyser and Differential Thermal Analyser (SETARAM) Labsys TGA/DTA unit in Central Laboratory at METU. Determination of critical temperatures and weight losses occurred during heating of the powders to temperatures of 900 °C with a heating rate of 10 °C/min were done. PNZT powders were produced by heating the solution at 100 °C for 5 h. Drying, pyrolysis and sintering temperatures were obtained from the analysis to obtain smooth and crack-free PNZT thin films.

3.3.5 Viscosity Measurements

Viscosity of the solutions was found by TA Instruments ARES Rheometer unit in Central Laboratory at METU. Viscosity (Pa.s) of the solutions with increasing shear rate (s^{-1}) curves was obtained for PNZT solutions in order to find uniformity of the solutions.

CHAPTER 4

RESULTS AND DISCUSSION

The aim of this study was to produce Nb added lead zirconate titanate thin films (PNZT) by sol-gel method and then investigate the effects of Nb^{+5} ion on structural, ferroelectric and dielectric properties. The method used during the entire work was chemical solution deposition. By this method, it is possible to obtain homogeneous stock solutions. This is required, because the quality of the films depends on the solution homogeneity and to be able to form crack free and smooth films. In order to find optimum sintering parameters, PNZT with 3 at % Nb doped thin films were produced. Different sintering temperatures (600, 650 and 700 °C) [7, 10, 32, 39, 40] and periods (1, 2 and 3 h) were taken, while the film thickness and composition were kept constant. By interpreting X-ray diffraction results and ferroelectric properties of films, the best sintering conditions were determined as 600 °C and 1 h. After this point, sintering temperature and sintering time were kept constant during the entire study. The thickness of the films was another important parameter, therefore different layered films were produced while all other parameters were kept constant. The thicknesses of the films were measured using SEM and the optimum thickness value was determined as 390 nm (2 layered films). Then the composition of the films was changed while the other parameters kept constant. The hysteresis parameters, dielectric constant and tangent loss values of PNZT thin films with varying Nb^{+5} ion additions were investigated and the optimum composition was determined using the remnant polarization and dielectric constant values. Coercive field and tangent loss values also played an important role on determining the optimum parameters. The grain sizes were estimated using FESEM.

Nb element was chosen as a dopant for PZT thin films in this study. Since Nb and Zr has a very close ionic radius (r_{Nb}: 0.69 and r_{Zr}: 0.72Å), possible distortions that will be created in the lattice is minimized. Five different compositions of PNZT thin films were produced. All of the compositions were selected near morphotropic phase boundary. This boundary lies between the tetragonal and rhombohedral regions of the phase diagram. Firstly, to compare Nb doped films with the undoped one, PZT films were produced with the same Zr/Ti ratio. Then by increasing Nb content, the effects of Nb^{+5} ion on the structural, ferroelectric and dielectric properties of the films were observed. Table 4.1 shows some experimental details of the specimens that were produced during the entire study.

Table 4.1 Experimental details for PNZT thin films produced during the study.

	For 15 min	*For 15 min*				**Spin Coater**	
Nb content (at %)	**Drying Temperature (°C)**	**Pyrolysis Temperature (°C)**	**Sintering Temperature (°C)**	**Sintering Time (h)**	**# of layers coated**	**Speed (rpm)**	**Time (sec)**
0	150	450	600	1	2	1500	30
1	150	450	600	1	2	1500	30
3	150	450	600	1	1	1500	30
3	150	450	600	1	2	1500	30
3	150	450	600	1	3	1500	30
3	150	450	650	1	2	1500	30
3	150	450	650	2	2	1500	30
3	150	450	600	1	4	1500	30
3	150	450	650	3	2	1500	30
3	150	450	600	2	2	1500	30
3	150	450	600	3	2	1500	30
3	150	450	700	1	2	1500	30
3	150	450	700	2	2	1500	30
3	150	450	700	3	2	1500	30
5	150	450	600	1	2	1500	30
7	150	450	600	1	2	1500	30

4.1 Thermal Analysis

Thermal analysis were done to determine the critical temperatures and the weight losses occurred during the heating of the solution using powders prepared by keeping the PNZT solution at 100 °C for 5 h. These powders were then heated to 900 °C with a heating rate of 10 °C/min. Drying, pyrolysis and sintering temperatures were obtained from the analysis to produce smooth and crack-free PNZT thin films.

By interpreting exothermic thermodynamic reactions in the differential thermal analysis (DTA) curve, important stages that PNZT powders have undergone while heating were obtained. Also, by thermogravimetry (TG) curves, weight losses were determined. DTA and TG curves of the PNZT gel that had a composition $Pb_{0.985}(Zr_{0.53}Ti_{0.47})_{0.97}Nb_{0.03}O_3$ were shown in Figure 4.1 and Figure 4.2, respectively. Combination of DTA and TG curves were plotted in Figure 4.3.

In the TG plot, there were 3 weight loss regions observed. The first one was approximately 2.15% between 50 °C and 115 °C. In this region, solvents and moisture present in the gel were removed. Second weight loss region, which was around 11.92%, had occurred between 115 °C and 410 °C. Between these temperatures, light organics and acetates were decomposed. The first exothermic peak in DTA curve at 318 °C also assists this behavior. The final weight loss region (3.39%) in the TG curve was observed between the temperatures 410 °C and 545 °C. This decrease in the weight can be explained by the formation of inorganic ceramic phase and decomposition of organic compounds which can also be seen from the exothermic peak at 500 °C in DTA curve. The last tiny exothermic peak that was found at 580 °C belongs to crystallization of the PNZT powder.

The real values of the critical temperatures that were found by the DTA curve were expected to be slightly lower than the obtained values because of using high heating rates of powders. The crystallization of PNZT powder starts at 580 °C. This means that perovskite formation had occurred after 580 °C. Further increase in the temperature only promotes the crystallization because there was no weight losses observed after 580 °C.

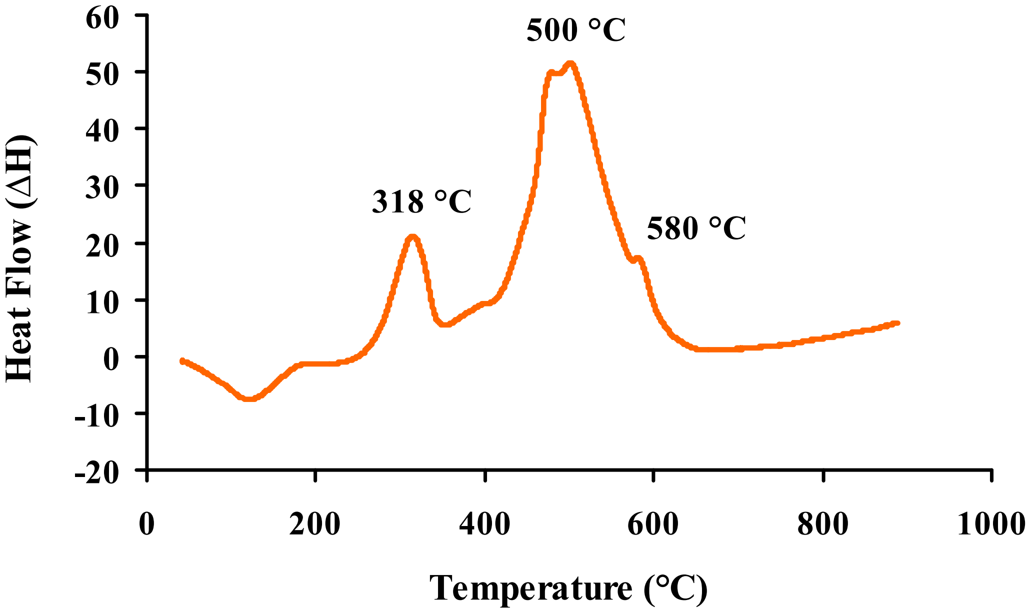

Figure 4.1 Differential thermal analysis (DTA) curve of PNZT gel with composition of $Pb_{0.985}(Zr_{0.53}Ti_{0.47})_{0.97}Nb_{0.03}O_3$.

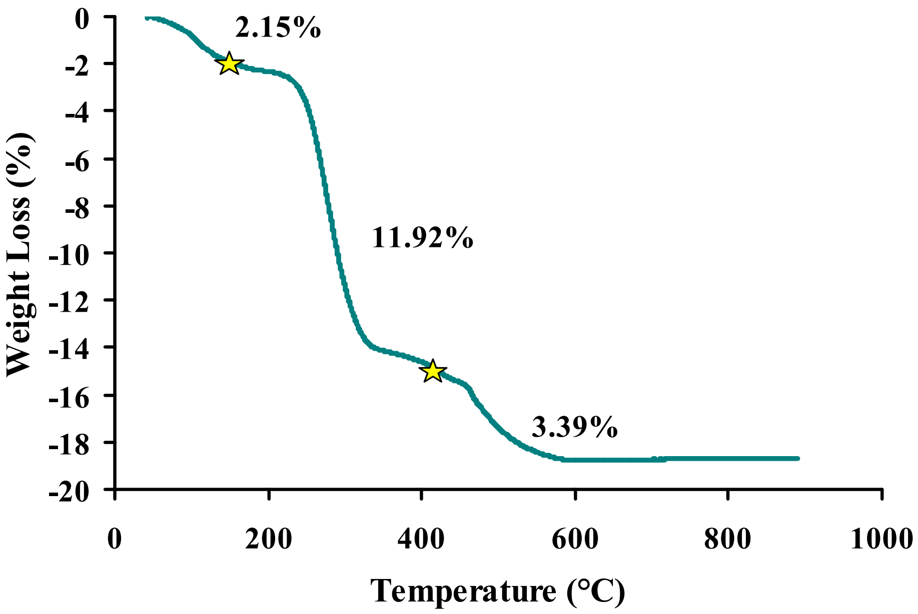

Figure 4.2 Thermogravimetry (TG) curve of PNZT gel with composition of $Pb_{0.985}(Zr_{0.53}Ti_{0.47})_{0.97}Nb_{0.03}O_3$.

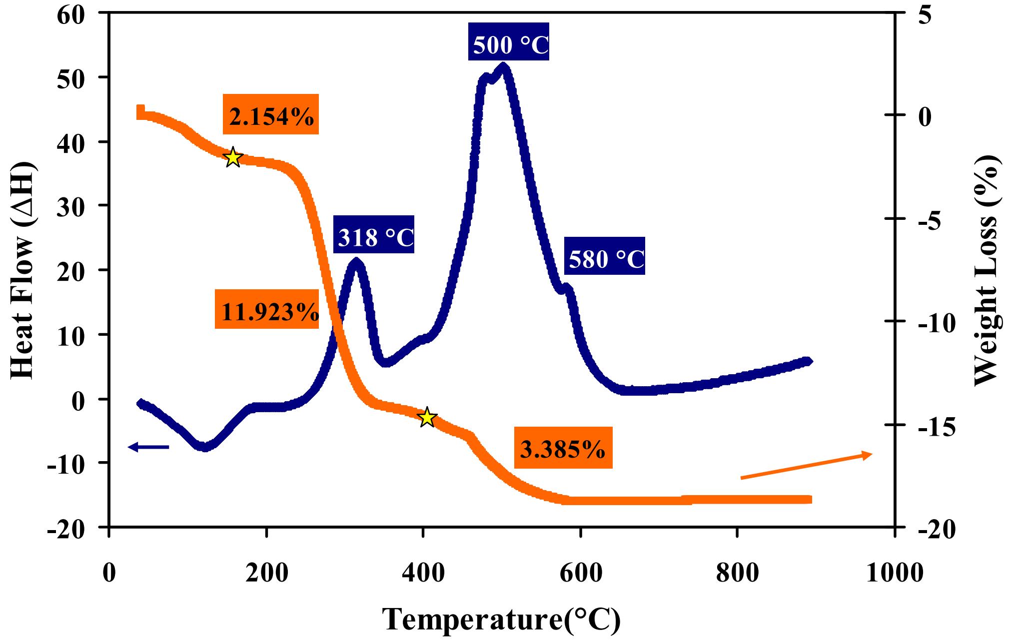

Figure 4.3 Differential thermal analysis (DTA) and thermogravimetry (TG) curves of PNZT gel with composition of $Pb_{0.985}(Zr_{0.53}Ti_{0.47})_{0.97}Nb_{0.03}O_3$.

Figure 4.4 shows the TGA curves of PNZT gels with varying Nb content. It was found that TGA curves of the samples containing varying Nb content were s,milar in behavior. However, weight loss values of these samples showed some variation maintaining the same temperatures in all of the curves which is also supported by the study of Kurchania and Milne [4]. It can be concluded that the selection of pyrolysis temperature as 450 °C and sintering temperature as 600 °C was a good choice for both the perovskite formation and to obtain crack-free and smooth films.

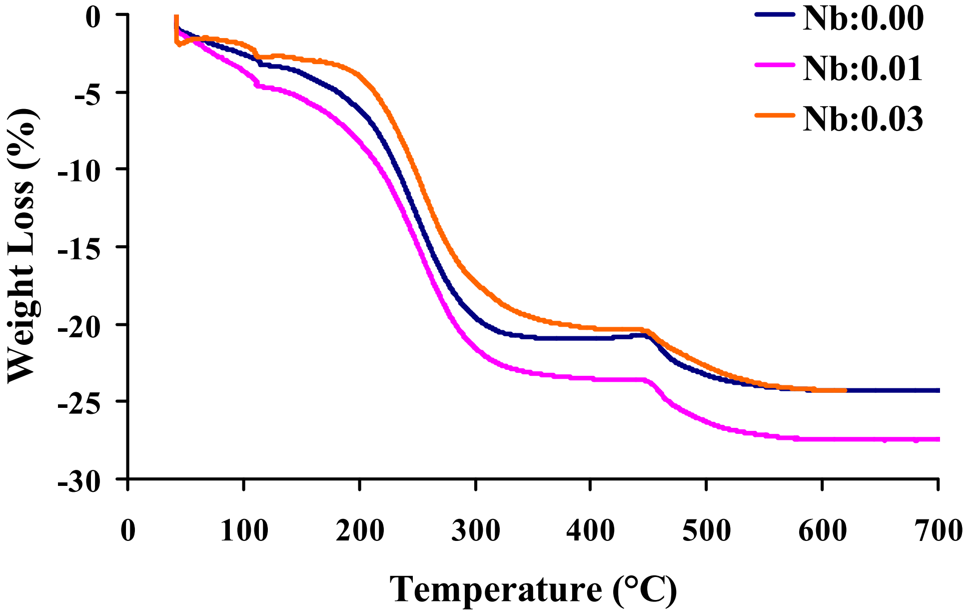

Figure 4.4 TGA curves of PNZT gel with varying Nb content.

4.2 Viscosity Measurements of PNZT Solution

Viscosity of PNZT solutions was measured to understand the uniformity of the solution. To be able to coat a uniform and smooth film on a substrate, a uniform solution is required.

Figure 4.5 shows the viscosity (Pa.s) of the solution ($Pb_{0.995}(Zr_{0.53}Ti_{0.47})_{0.99}Nb_{0.01}O_3$) with increasing shear rate (s^{-1}). It can be seen that viscosity did not change significantly as the shear rate increased which showed the uniformity of the solution. The average viscosity was measured as 0.00258 Pa.s.

The behavior of the solution was estimated by calculating the power law index. It was found as 0,999 from eq. [2.9]. This value is very close to 1 meaning that it is a Newtonian solution. Newtonian solutions exhibit homogeneous and uniform behavior.

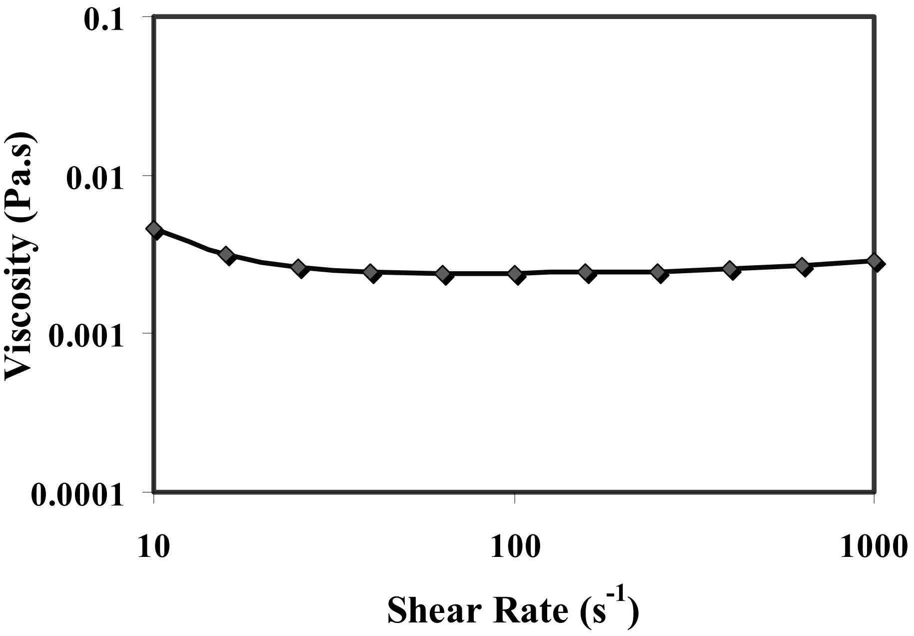

Figure 4.5 Viscosity (Pa.s) vs shear rate (s^{-1}) curve of a PNZT solution which had a composition $Pb_{0.995}(Zr_{0.53}Ti_{0.47})_{0.99}Nb_{0.01}O_3$.

4.3 Crystalline Film Formation

The phases in PNZT thin films deposited on (111)-Pt/Ti/SiO_2/Si-(100) substrates were determined by XRD studies. Optimum sintering temperature and sintering time were estimated using the phases present in the film and magnitudes of the peak intensities of these phases. Sintering temperatures of 600, 650 and 700 °C were applied to the films. Also sintering time was taken as another parameter. Sintering periods of 1, 2 and 3 h were applied to the samples. To find optimum sintering parameters, PNZT thin films with the composition $Pb_{0.985}(Zr_{0.53}Ti_{0.47})_{0.97}Nb_{0.03}O_3$ and thickness of 390 nm were produced.

The final crystal structure of PNZT thin films was highly sensitive to both the initial chemical stoichiometry and sintering temperature. The volume fraction of pyrochlore phase and the time required for its transformation to the perovskite phase strongly depend on temperature [5].

In Figures 4.6 to 4.8, it can be seen that perovskite peaks emerged clearly at 600 °C for 1, 2 and 3 h, respectively. Perovskite peaks emerged at approximately 2θ = 22° (100), 38° (111) and 45° (200). Also, Pt (111) peak at 2θ = 40° was observed which overlapped with the perovskite peak at 2θ = 38° at low intensities. The highest perovskite peak emerged at 2θ = 38° (111) showing that the preferred orientation was on (111) crystallographic plane because of the (111) oriented Pt substrate. Figure 4.9 shows all the curves together in order to see the effect of sintering time easily for the films sintered at 600 °C.

The crystallization of perovskite phase and pyrochlore phase from the amorphous phase are both nucleation controlled processes, because there is no significant grain growth at temperatures between 450 °C and 600 °C. However after 600 °C, the grains grow and there is a significant Pb loss and possibility of forming a lead deficient pyrochlore phase at high temperatures [5].

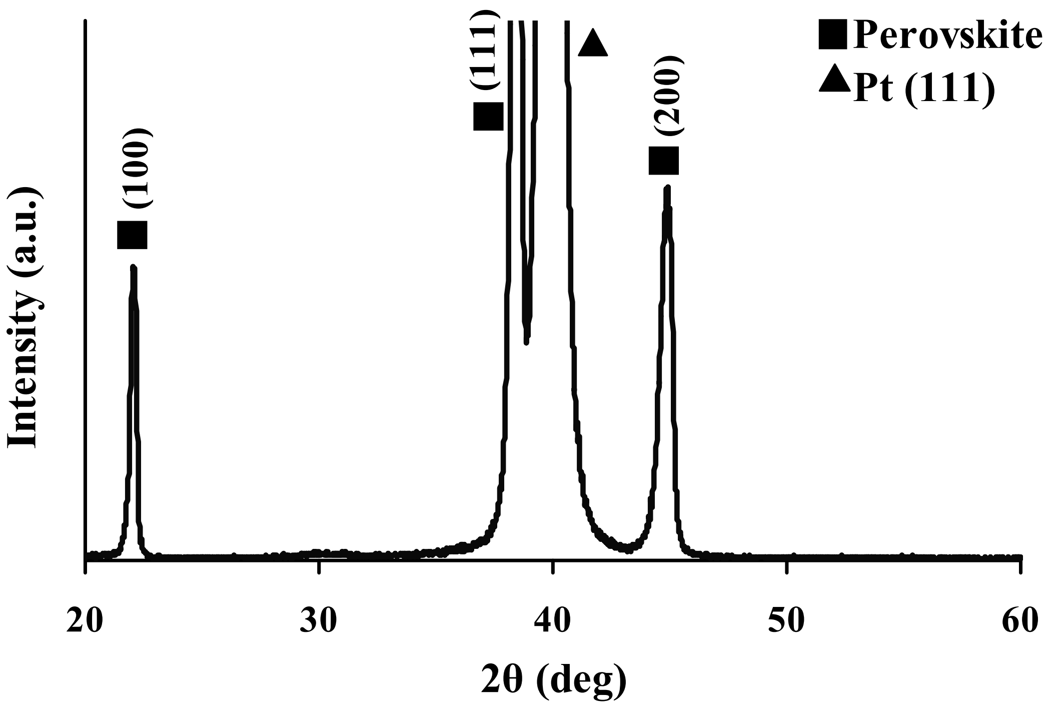

Figure 4.6 X-ray diffractogram of PNZT thin film that was 390 nm in thickness with the composition $Pb_{0.985}(Zr_{0.53}Ti_{0.47})_{0.97}Nb_{0.03}O_3$ and sintered at 600 °C for 1 h.

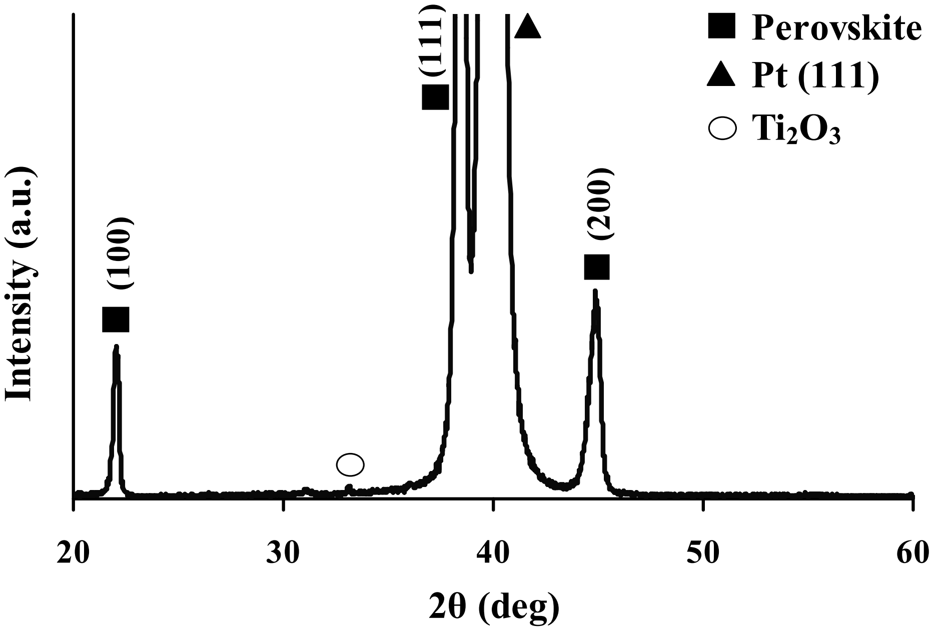

Figure 4.7 X-ray diffractogram of PNZT thin film that was 390 nm in thickness with the composition $Pb_{0.985}(Zr_{0.53}Ti_{0.47})_{0.97}Nb_{0.03}O_3$ and sintered at 600 °C for 2 h.

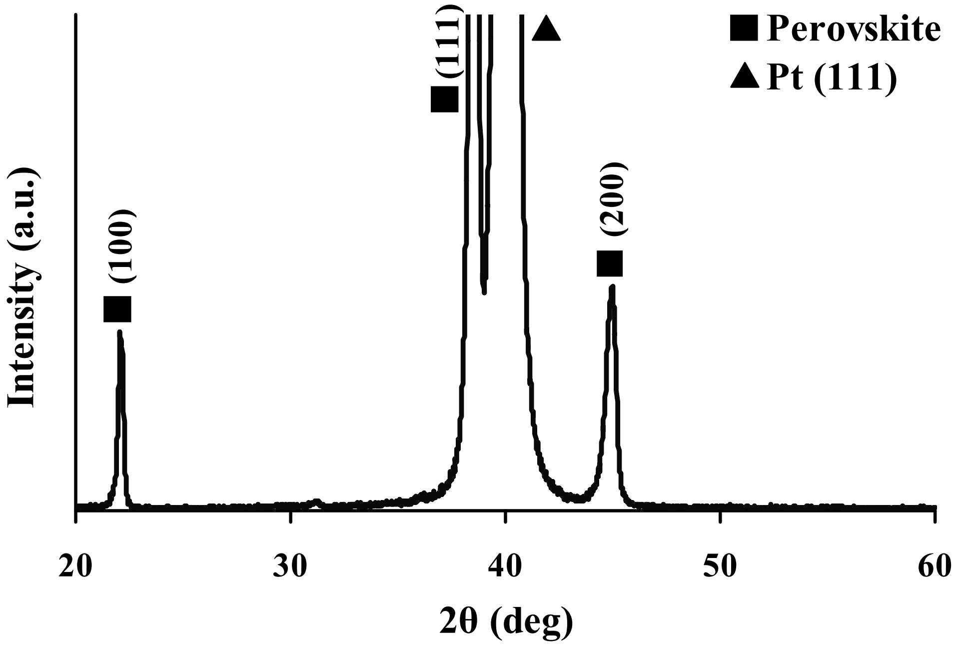

Figure 4.8 X-Ray diffractogram of PNZT thin film that was 390 nm in thickness with the composition $Pb_{0.985}(Zr_{0.53}Ti_{0.47})_{0.97}Nb_{0.03}O_3$ and sintered at 600 °C for 3 h.

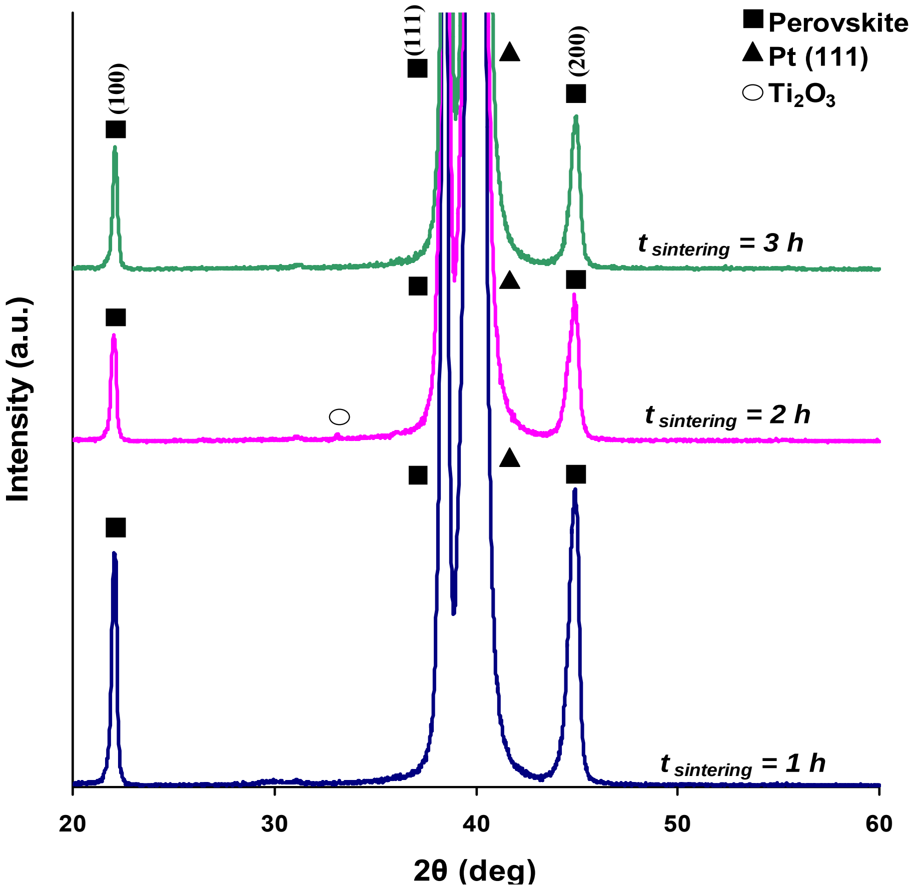

Figure 4.9 X-Ray diffractograms of PNZT thin films that were 390 nm with the composition $Pb_{0.985}(Zr_{0.53}Ti_{0.47})_{0.97}Nb_{0.03}O_3$ and sintered at 600 °C for 1, 2 and 3 h.

There was no pyrochlore phase determined in PNZT films sintered at 600 °C for 1 and 3 h. This result is consistent with the previous studies [22, 34]. However, a small Ti_2O_3 peak was observed in films sintered for 2 h. This pyrochlore phase emerged at $2\theta = 33°$ (121). Its JCPDS file number is 76-0145. This phase decreases the ferroelectric and dielectric properties of PNZT thin films that will be shown in ferroelectric and dielectric properties part.

Figures 4.10 and 4.11 show the X-ray diffractogram of PNZT thin films sintered at 450 and 550 °C, respectively. It is important to analyze the films at different sintering temperatures between the pyrolysis and crystallization steps. Figure 4.10 shows the X-ray diffractogram of PNZT thin film sintered at 450 °C for 3 h. There were 2 peaks observed. One belongs to the substrate Pt (111) (2θ = 40°) and the other peak belongs to PbO (2θ = 29°) which can be named as the pyrochlore phase. This phase was determined from powder diffraction material ID card whose JCPDS file number was 88-1589. Kurchania and Milne [4] found the same PbO peak with the PNZT films sintered at 500 °C. This pyrochlore phase was also confirmed in Figure 4.11.

It can be said that the minimum temperature for crystallization of perovskite phase from the amorphous phase is 600 °C, because the PbO peak still remains in the films sintered at 550 °C for 1 h since no pyrochlore phase is wanted. Additional perovskite peaks emerged for the PNZT film with the composition $Pb_{0.985}(Zr_{0.53}Ti_{0.47})_{0.97}Nb_{0.03}O_3$ sintered at 550 °C for 1 h can be seen in Figure 4.11. This film consists of 10 layers and had a thickness of 1.7 μm. Peaks corresponding to perovskite phase emerged at approximately 2θ = 22° (100), 31° (110), 38° (111), 45° (200) and 55° (211). It was not possible to see these additional peaks in two layered films. The intensities of the peaks were increased as the thickness increased and because of that additional 2θ = 31° (110) and 55° (211) peaks were emerged in thick films.

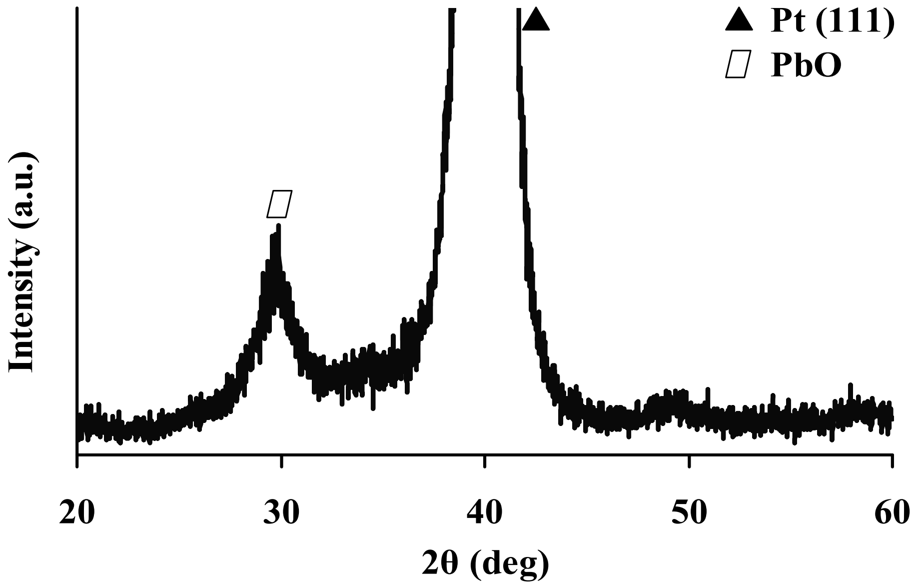

Figure 4.10 X-ray diffractogram of PNZT thin film that was 390 nm in thickness with the composition $Pb_{0.985}(Zr_{0.53}Ti_{0.47})_{0.97}Nb_{0.03}O_3$ and sintered at 450 °C for 3 h.

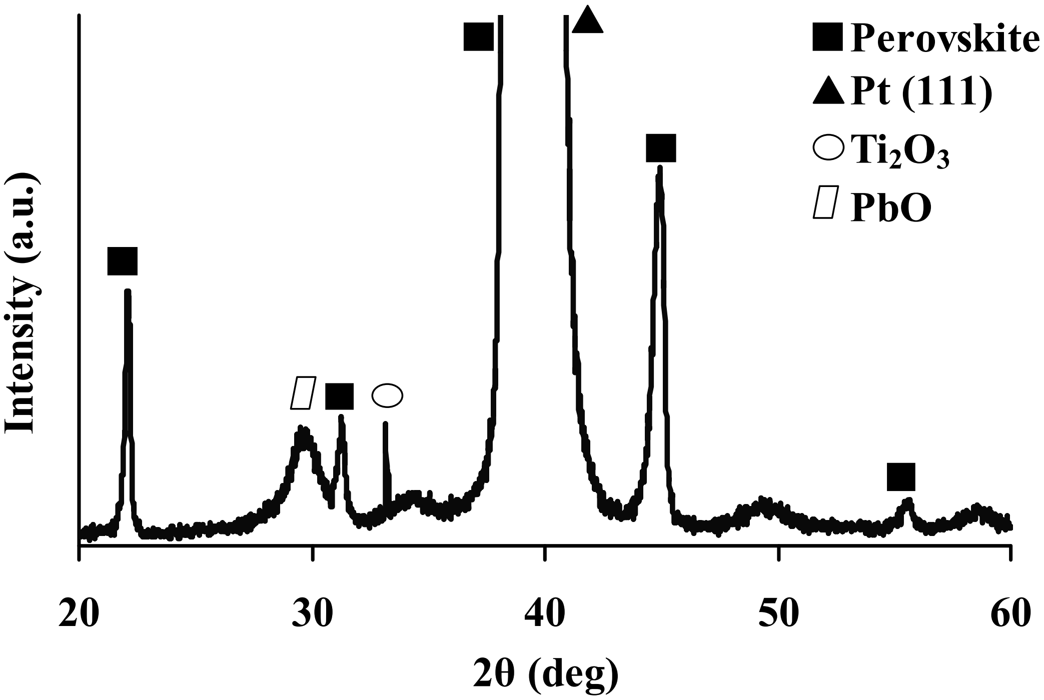

Figure 4.11 X-ray diffractogram of PNZT thin film that was 1.7 μm in thickness with the composition $Pb_{0.985}(Zr_{0.53}Ti_{0.47})_{0.97}Nb_{0.03}O_3$ and sintered at 550 °C for 1 h.

Ti_2O_3 phase emerged in films sintered at 550 °C. This phase was also seen in other PNZT films sintered at temperatures higher than 600 °C. Figures 4.12 to 4.14 show X-ray diffraction patterns of PNZT thin films sintered at 650 °C for 1, 2 and 3 h. To see the effect of sintering time, these three curves are placed in one figure which is shown in Figure 4.15. For all sintering periods, there was pyrochlore phase determined as Ti_2O_3. The effect of this phase on the properties of PNZT thin films will be seen in ferroelectric and dielectric measurements part in a detailed manner. In Figure 4.15, it is clear that intensities of the perovskite peaks changed randomly as the sintering period changed. The highest perovskite peak was observed at $2\theta = 38°$.

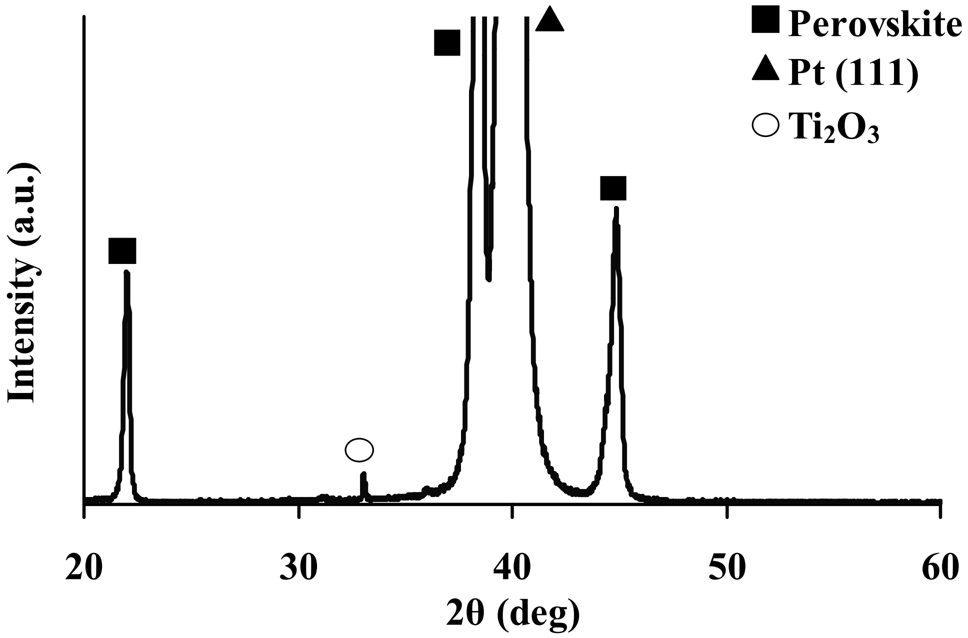

Figure 4.12 X-ray diffractogram of PNZT thin film that was 390 nm in thickness with the composition $Pb_{0.985}(Zr_{0.53}Ti_{0.47})_{0.97}Nb_{0.03}O_3$ and sintered at 650 °C for 1 h.

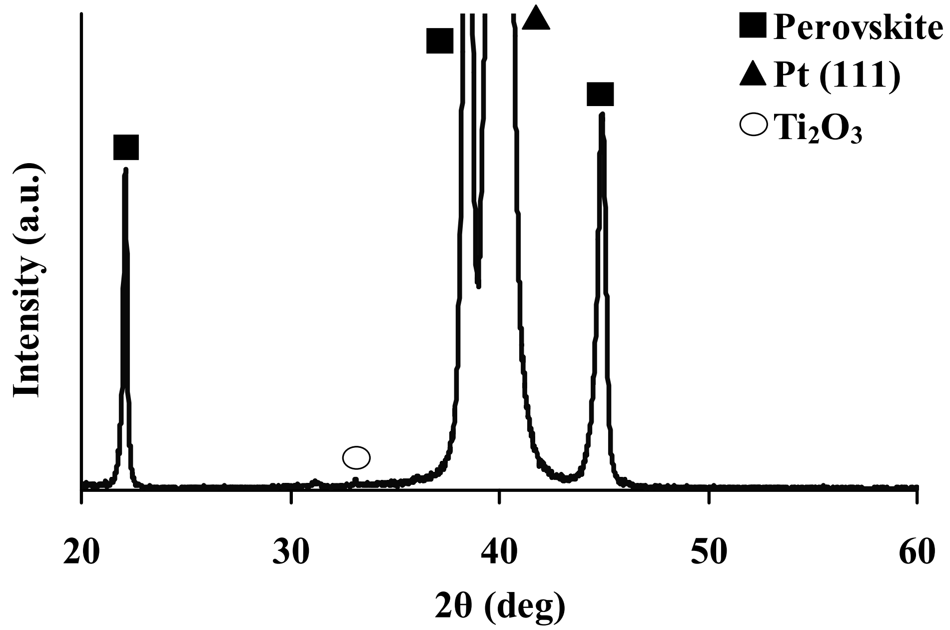

Figure 4.13 X-ray diffractogram of PNZT thin film that was 390 nm in thickness with the composition $Pb_{0.985}(Zr_{0.53}Ti_{0.47})_{0.97}Nb_{0.03}O_3$ and sintered at 650 °C for 2 h.

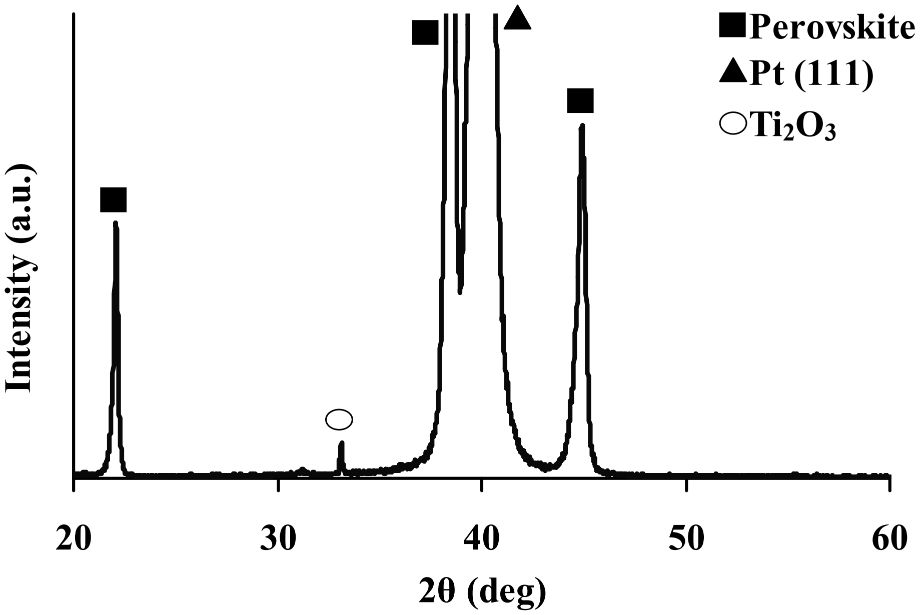

Figure 4.14 X-Ray diffractogram of PNZT thin film that was 390 nm in thickness with the composition $Pb_{0.985}(Zr_{0.53}Ti_{0.47})_{0.97}Nb_{0.03}O_3$ and sintered at 650 °C for 3 h.

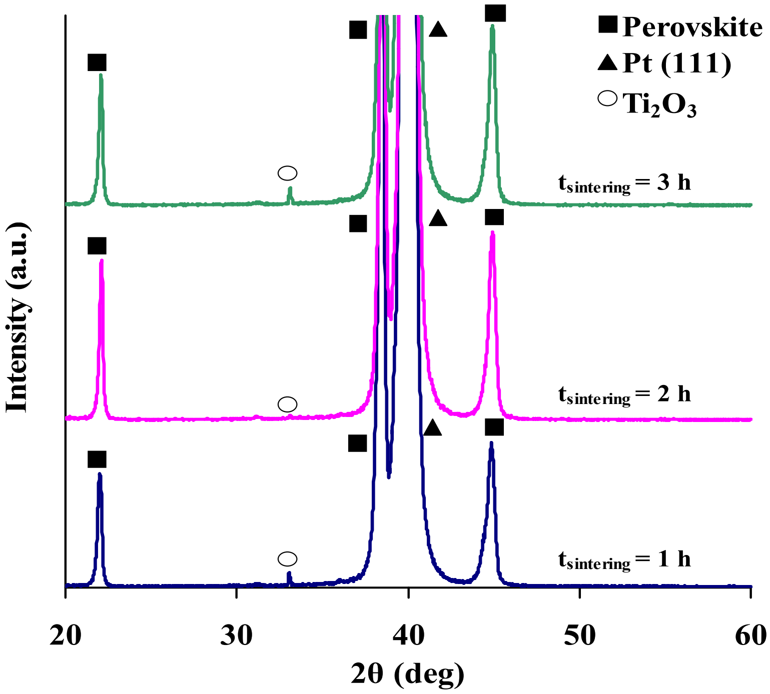

Figure 4.15 X-Ray diffractograms of PNZT thin films that were 390 nm in thickness with composition $Pb_{0.985}(Zr_{0.53}Ti_{0.47})_{0.97}Nb_{0.03}O_3$ and sintered at 650 °C for 1, 2 and 3 h.

XRD patterns of PNZT thin films sintered at 700 °C for 1, 2 and 3 h with the same composition of $Pb_{0.985}(Zr_{0.53}Ti_{0.47})_{0.97}Nb_{0.03}O_3$ were shown in Figures 4.16 to 4.18. Ti_2O_3 phase was determined for all sintering durations similar to PNZT thin films sintered at 650 °C. Same perovskite peaks were observed similar to films sintered at 600 and 650 °C. Figure 4.19 shows all the curves together in order to see the effect of sintering time easily for the films sintered at 700 °C.

All of the films showed polycrystalline structure with (111) preferred orientation. There was pyrochlore phase obtained in films sintered at temperatures higher than 600 °C. The final crystal structure of PNZT thin films was found to be highly sensitive to both the initial chemical stoichiometry and sintering temperature.

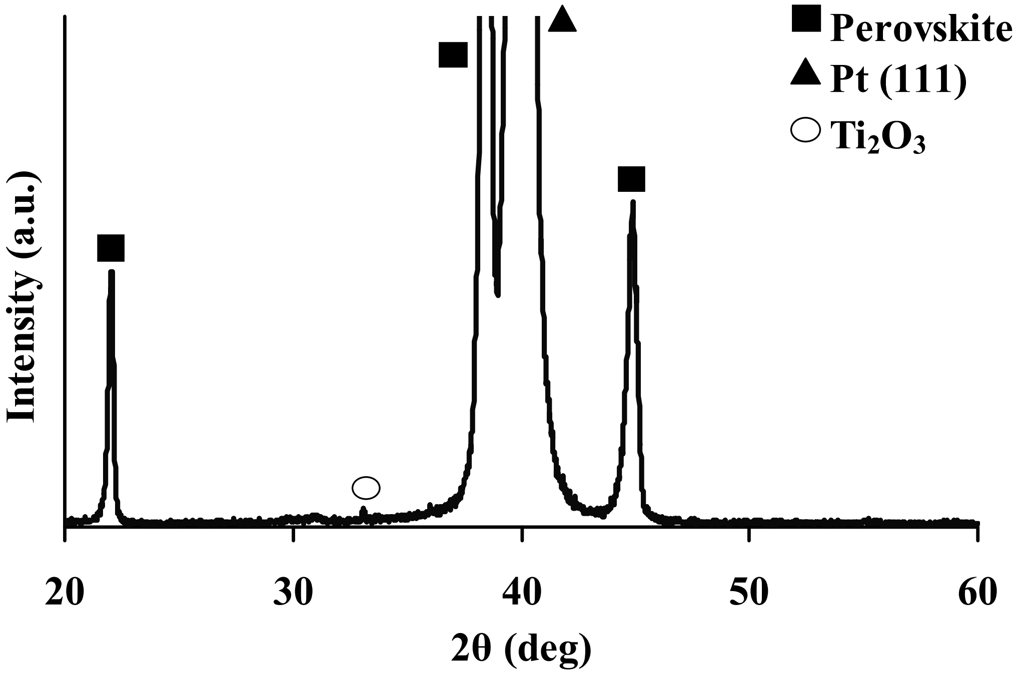

Figure 4.16 X-ray diffractogram of PNZT thin film that was 390 nm in thickness with the composition $Pb_{0.985}(Zr_{0.53}Ti_{0.47})_{0.97}Nb_{0.03}O_3$ and sintered at 700 °C for 1 h.

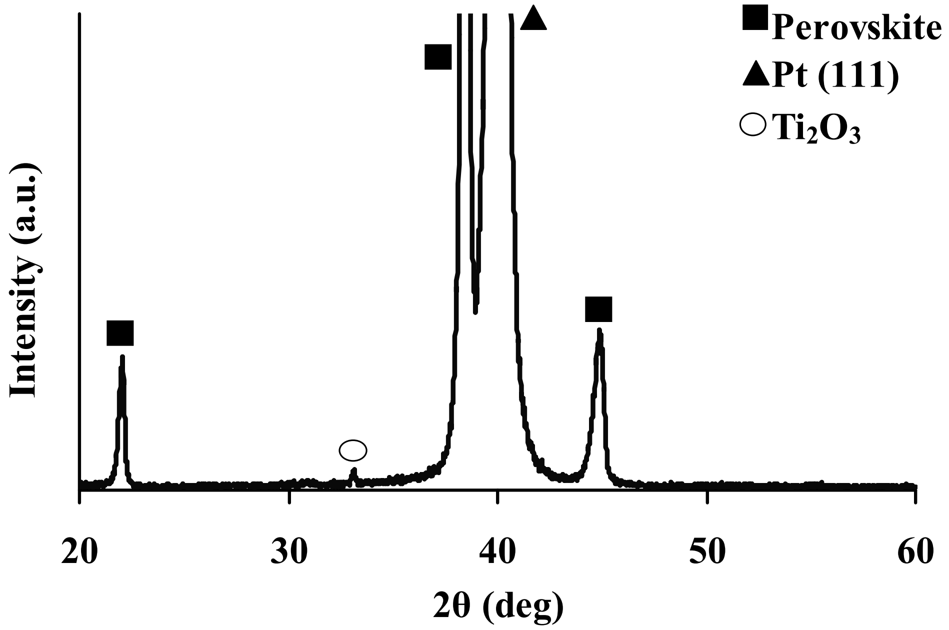

Figure 4.17 X-ray diffractogram of PNZT thin film that was 390 nm in thickness with the composition $Pb_{0.985}(Zr_{0.53}Ti_{0.47})_{0.97}Nb_{0.03}O_3$ and sintered at 700 °C for 2 h.

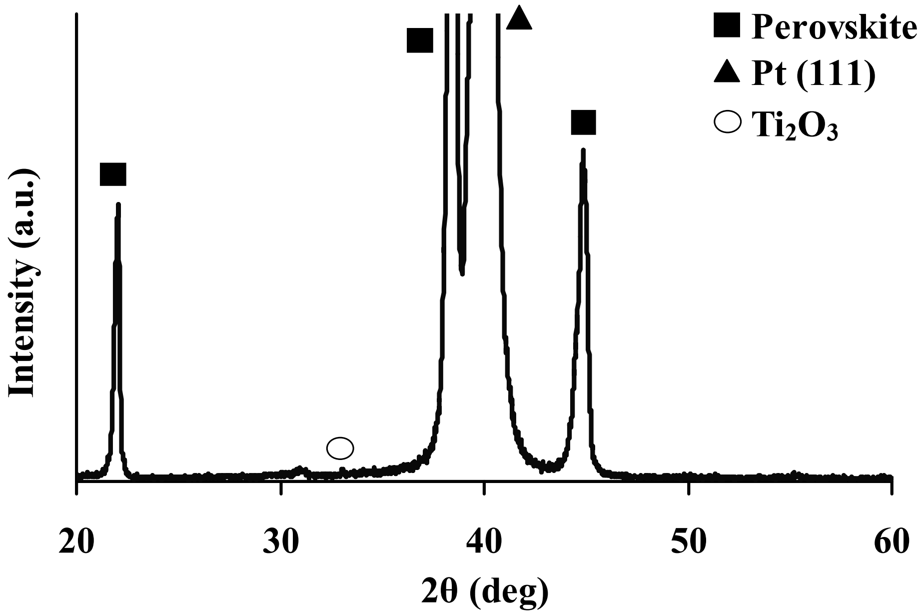

Figure 4.18 X-ray diffractogram of PNZT thin film that was 390 nm in thickness with the composition $Pb_{0.985}(Zr_{0.53}Ti_{0.47})_{0.97}Nb_{0.03}O_3$ and sintered at 700 °C for 3 h.

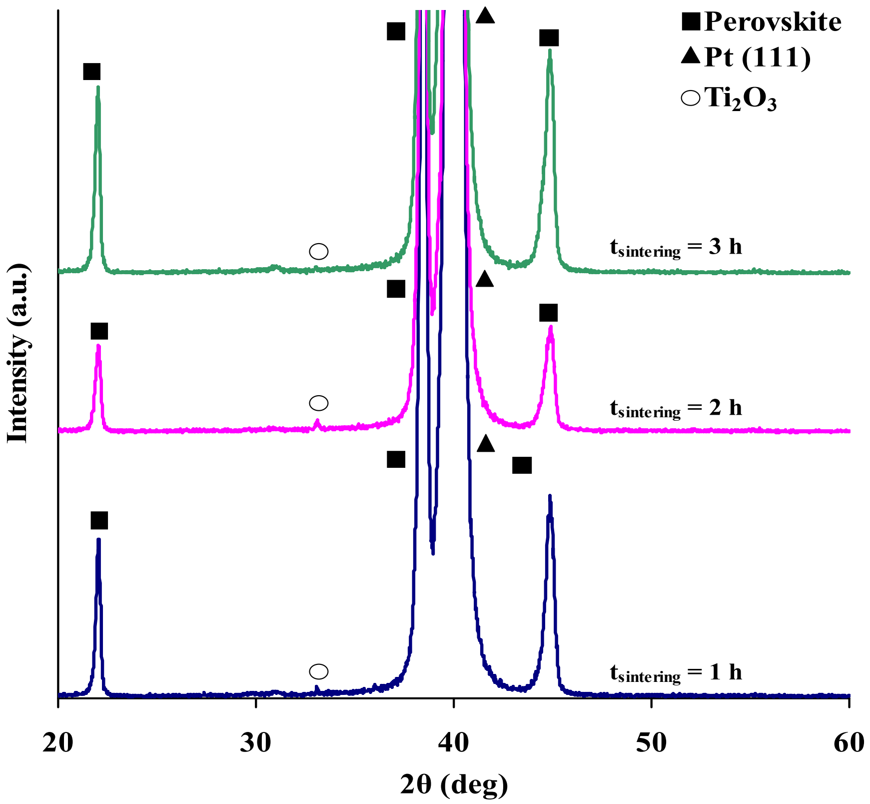

Figure 4.19 X-ray diffractograms of PNZT thin films that were 390 nm in thickness with the composition $Pb_{0.985}(Zr_{0.53}Ti_{0.47})_{0.97}Nb_{0.03}O_3$ and sintered at 700 °C for 1, 2 and 3 h.

At sintering temperatures higher than 600 °C, there was Ti_2O_3 phase observed in all of the films. Figure 4.20 shows X-ray diffractogram of PNZT thin films sintered at 600, 650 and 700 °C for 1 h in order to see the effect of sintering temperature. It can be seen from the figure that, pyrochlore (Ti_2O_3) phase was observed for the films sintered at 650 and 700 °C. The highest perovskite peak intensity was achieved for films sintered at 600 °C for 1 h. So the optimum sintering temperature was determined as 600 °C. The optimum sintering period was determined from the intensities of the perovskite peaks. The highest perovskite peak intensity was obtained for films sintered for 1 h that is shown in Figure 4.9.

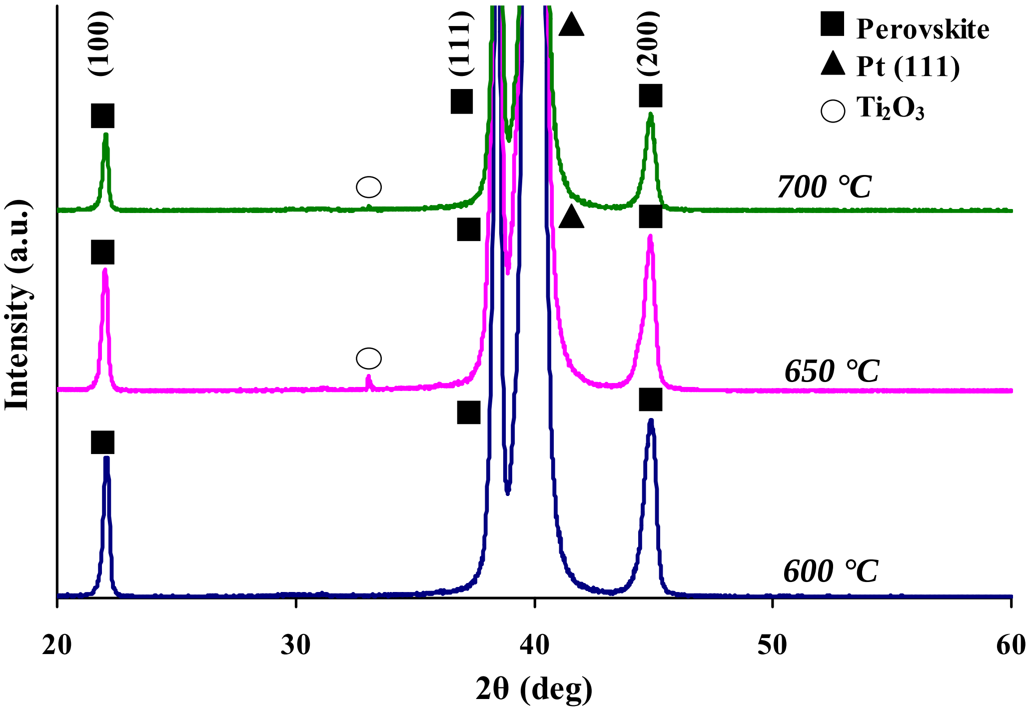

Figure 4.20 X-ray diffractograms of PNZT thin films that were 390 nm in thickness with the composition $Pb_{0.985}(Zr_{0.53}Ti_{0.47})_{0.97}Nb_{0.03}O_3$ and sintered at 600, 650 and 700 °C for 1 h.

After determining the optimum sintering parameters, PNZT thin films with different compositions were produced. Nb content was changed at constant sintering temperature, sintering time and film thickness in order to see the effects of Nb^{+5} ion addition on PNZT thin films. Figure 4.21 shows the X-ray diffractogram of PZT thin film with the composition $Pb(Zr_{0.53}Ti_{0.47})O_3$. In Figures 4.22 to 4.24 PNZT thin films with Nb content containing 1, 5 and 7 at % was given, respectively. The intensities of the perovskite peaks (100), (111) and (200) were highest in the 1 at % Nb doped films. As the Nb addition was increased, the intensities of the perovskite peaks were decreased. In 0 and 7 at % Nb doped thin films Ti_2O_3 impurity phase was determined.

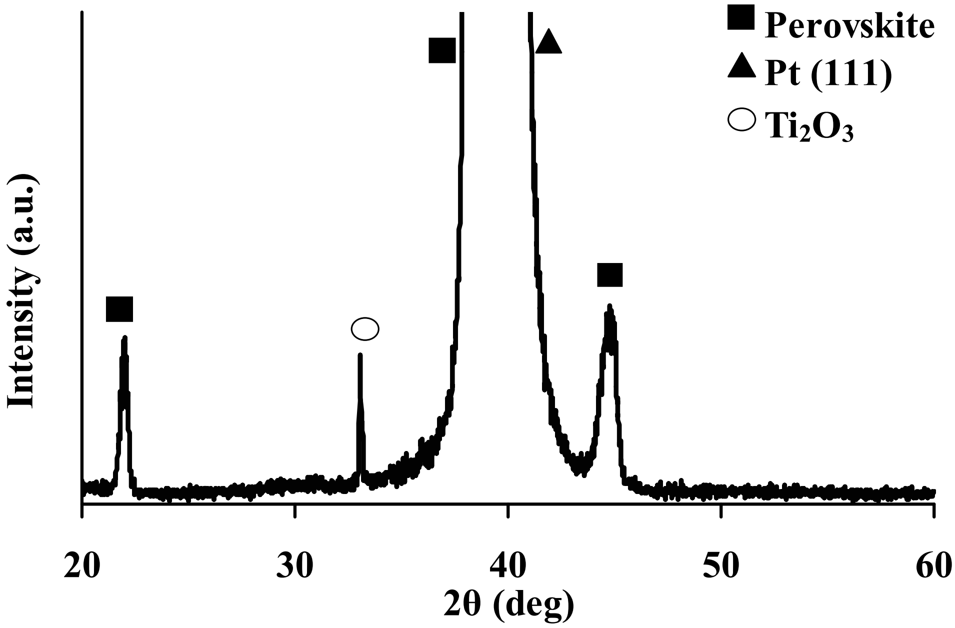

Figure 4.21 X-ray diffractogram of PZT thin film that was 390 nm in thickness with the composition $Pb(Zr_{0.53}Ti_{0.47})O_3$ and sintered at 600 °C for 1 h.

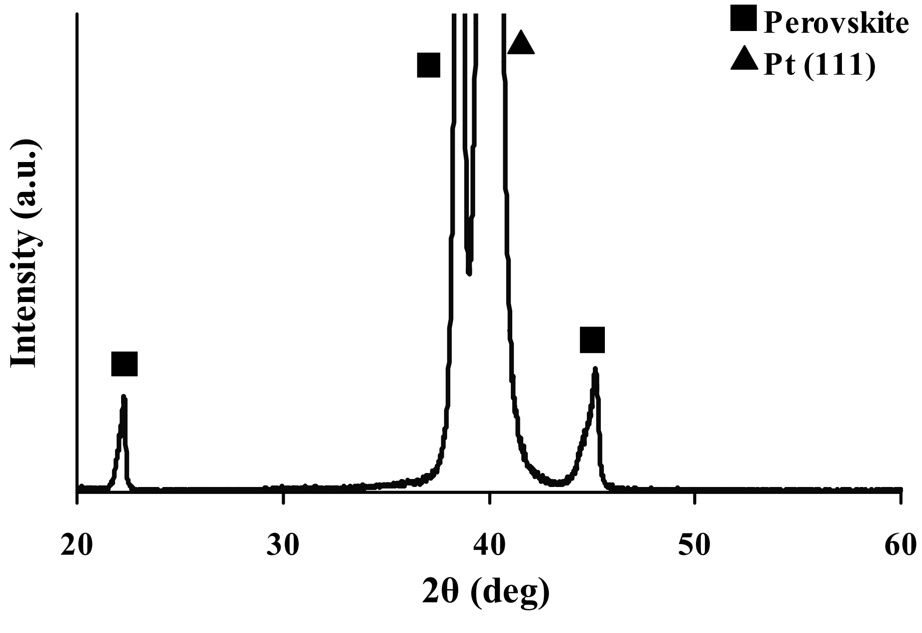

Figure 4.22 X-ray diffractogram of PNZT thin film that was 390 nm in thickness with the composition $Pb_{0.995}(Zr_{0.53}Ti_{0.47})_{0.99}Nb_{0.01}O_3$ and sintered at 600 °C for 1 h.

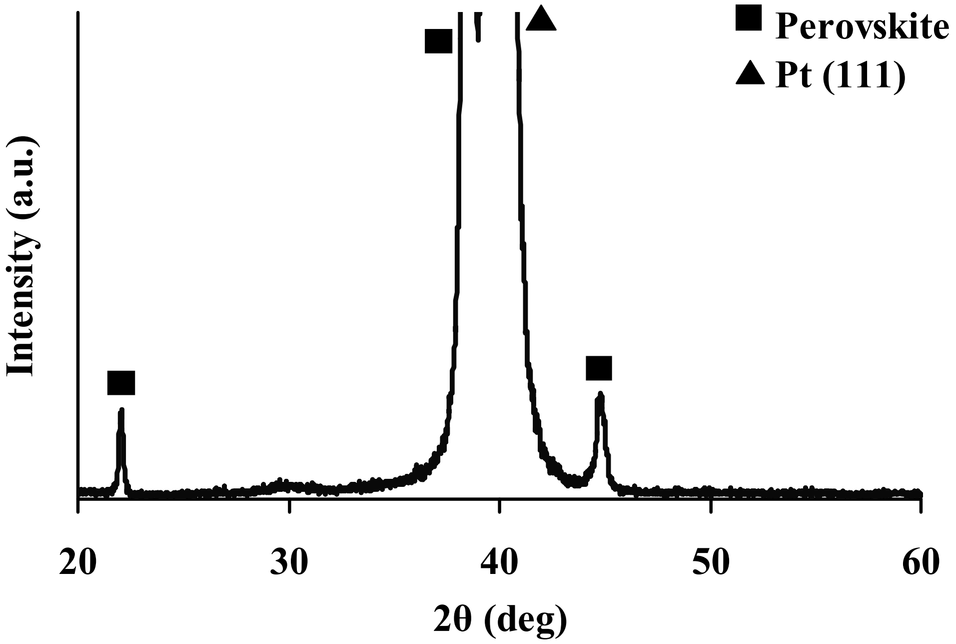

Figure 4.23 X-ray diffractogram of PNZT thin film that was 390 nm in thickness with the composition $Pb_{0.975}(Zr_{0.53}Ti_{0.47})_{0.95}Nb_{0.05}O_3$ and sintered at 600 °C for 1 h.

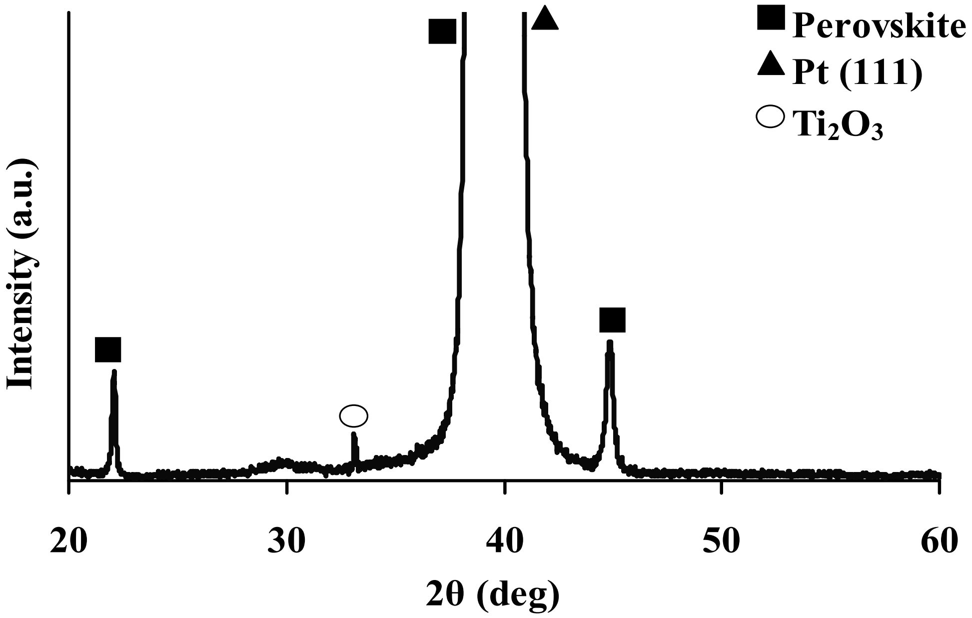

Figure 4.24 X-ray diffractogram of PNZT thin film that was 390 nm in thickness with the composition $Pb_{0.965}(Zr_{0.53}Ti_{0.47})_{0.93}Nb_{0.07}O_3$ and sintered at 600 °C for 1 h.

4.4 Composition of PNZT Thin Films

The composition of PNZT thin films and powders were investigated by EDS analysis. The powders were prepared by drying PNZT stock solution at 100 °C for 5 h. From the analysis, the quantities of the elements Pb, Nb, Ti and Zr were determined. The results of this analysis gave important clues about the composition of the solution and the films that were prepared. The expected compositions and the results were compared to make sure that the experimental route was going right.

Figure 4.25 shows the EDS result of the PNZT film of composition $Pb_{0.985}(Zr_{0.53}Ti_{0.47})_{0.97}Nb_{0.03}O_3$ (3 at % Nb doped films) sintered at 600 °C for 2 h. The average film thickness was around 5 μm. The SEM image of the thick film was given in Figure 4.26.

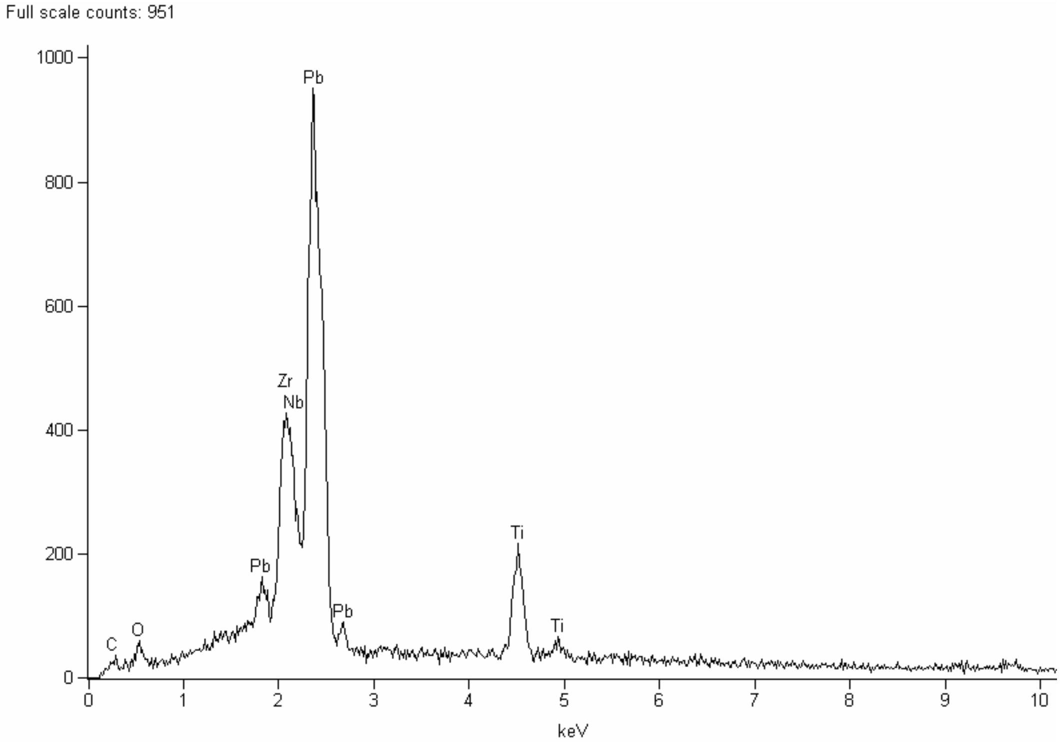

Figure 4.25 EDS analysis of PNZT film with a thickness 5.55 μm and composition $Pb_{0.985}(Zr_{0.53}Ti_{0.47})_{0.97}Nb_{0.03}O_3$ and sintered at 600 °C for 2 h.

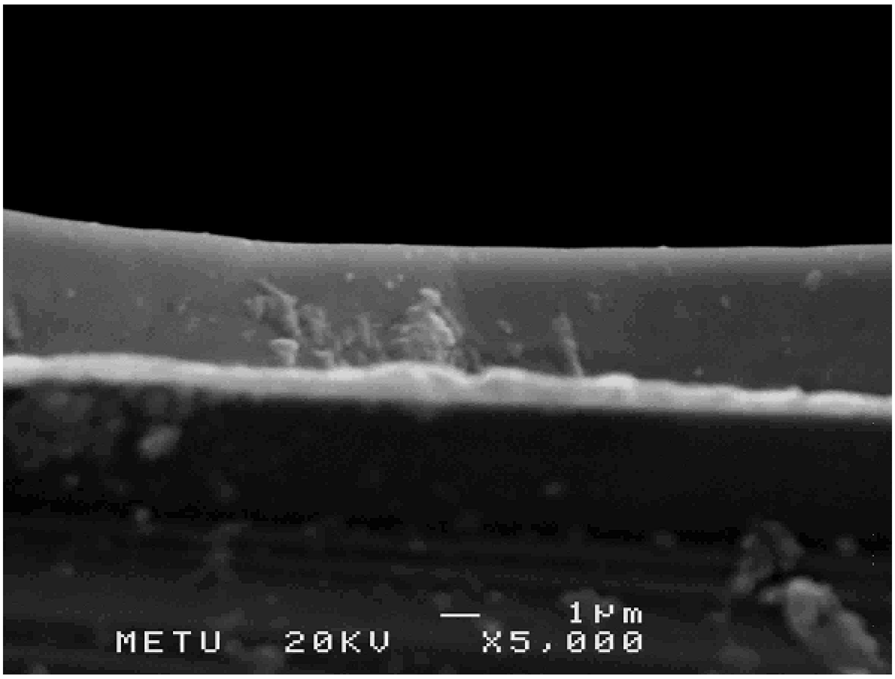

Figure 4.26 The cross-section of PNZT film with an average thickness of 5 μm and composition $Pb_{0.985}(Zr_{0.53}Ti_{0.47})_{0.97}Nb_{0.03}O_3$ and sintered at 600 °C for 2 h.

Thick films were prepared to find out the composition, because in the prepared thin films that have thicknesses smaller than 1 μm, there was Pt peak observed in EDS results coming from the substrate and it is overlapping with the Zr peak. In Figure 4.25, there was no Pt peak present in the EDS analysis, but there was another problem that niobium and zirconium peaks were overlapping too. PZT powders were produced to solve this problem. Figure 4.27 shows the EDS analysis of PZT powders that had a composition $Pb(Zr_{0.53}Ti_{0.47})O_3$. Pt peak was eliminated by preparing powders and Nb peak was eliminated by using PZT.

The calculated amount of elements from the EDS analysis of PZT powders was given in Table 4.2. Pb/Zr/Ti ratio given in the table was calculated by using the atomic percentages given in EDS analysis. This ratio was approximately similar to the intended PZT composition showing that the processing route used in the study was successful.

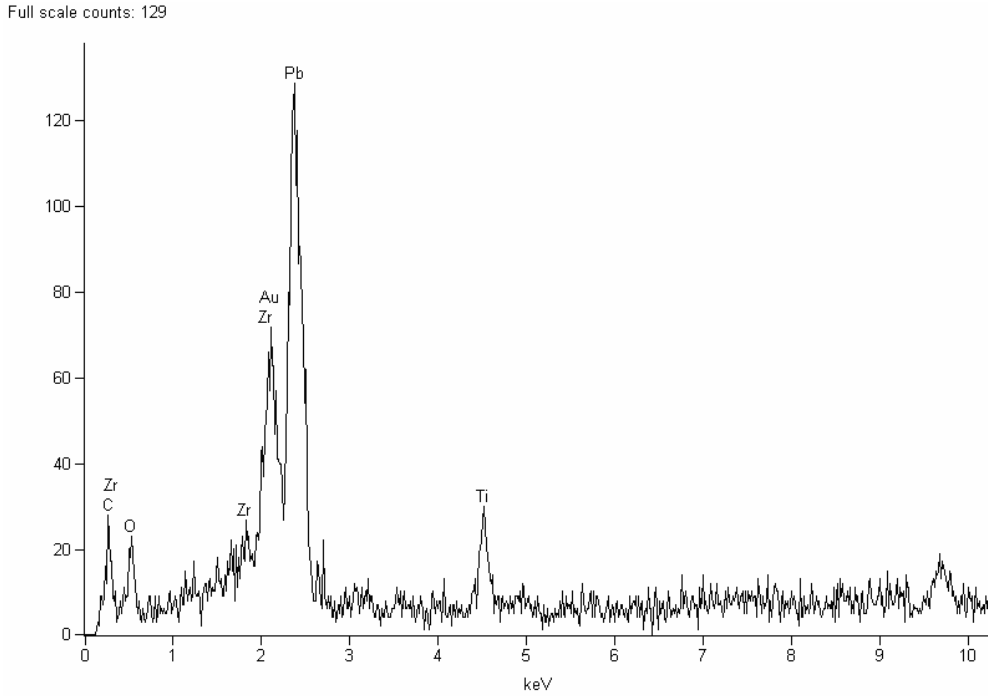

Figure 4.27 EDS analysis of PZT powders with a composition $Pb(Zr_{0.53}Ti_{0.47})O_3$.

Table 4.2 Quantities of the elements which belongs to EDS analysis of PZT powders with a composition $Pb(Zr_{0.53}Ti_{0.47})O_3$.

Prepared Composition	Pb (at %)	Zr (at %)	Ti (at %)	Pb/Zr/Ti by EDS analysis
$Pb(Zr_{0.53}Ti_{0.47})O_3$	52.49	25.12	22.39	1.1/0.526/0.469

4.5 Morphology of PNZT Thin Films

The morphology of PNZT thin films were investigated by Atomic Force Microscopy (AFM), Surface Profilometry, Scanning Electron Microscope (SEM) and Field Emission Scanning Electron Microscope (FESEM). The surface characteristics of the films were analyzed firstly by AFM. Figure 4.28 shows the surface of a PNZT thin film with the composition $Pb_{0.985}(Zr_{0.53}Ti_{0.47})_{0.97}Nb_{0.03}O_3$ sintered at 600 °C for 1 h. There were no defects and cracks observed at the surfaces of the films.

Surface profilometry technique was used to see the surface roughness of the films. These results also confirmed the smoothness of the films. It can be seen from the Figure 4.29 that the roughness of PNZT thin film was very low indicating a uniform surface.

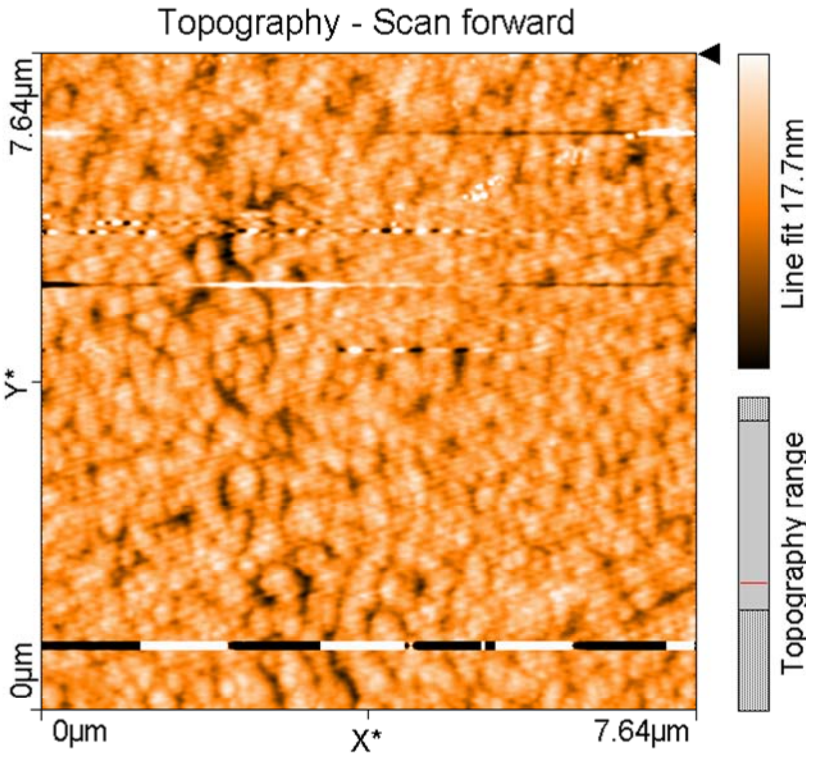

Figure 4.28 Atomic Force Microscopy (AFM) image of PNZT thin film with a thickness 250 nm and composition $Pb_{0.985}(Zr_{0.53}Ti_{0.47})_{0.97}Nb_{0.03}O_3$ sintered at 600 °C for 1 h.

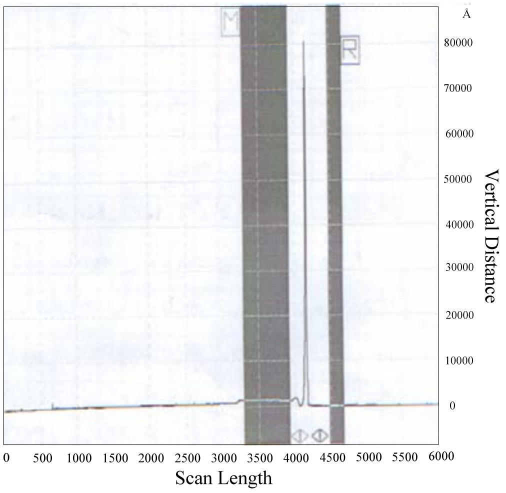

Figure 4.29 Profilometry image of PNZT thin film with a thickness 250 nm and composition $Pb_{0.985}(Zr_{0.53}Ti_{0.47})_{0.97}Nb_{0.03}O_3$ sintered at 600 °C for 1 h.

SEM images also assist the results obtained from AFM images. There can be the possibility of cracking due to the thermal mismatch between the film and the substrate. Also by the conversion of the gel to a dense film on the substrate, stresses can be generated leaving cracks on the surface of the films. However, these two conditions are not valid for the present films and Figures 4.30 and 4.31 show that the films were smooth and crack-free.

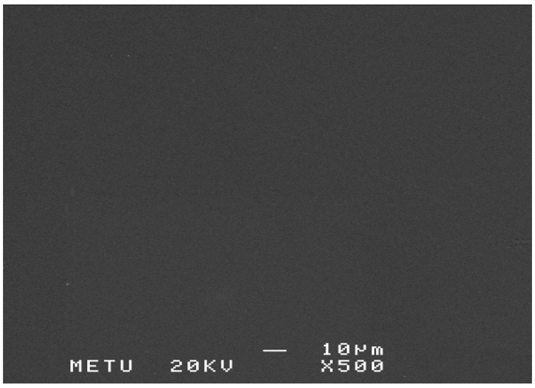

Figure 4.30 SEM image of the surface of PNZT thin film with composition $Pb_{0.985}(Zr_{0.53}Ti_{0.47})_{0.97}Nb_{0.03}O_3$ and sintered at 600 °C for 1 h.

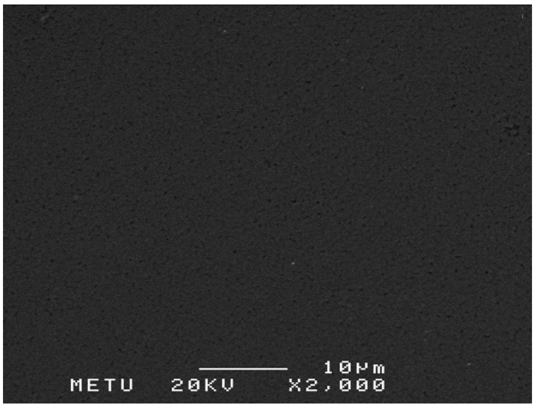

Figure 4.31 SEM image of the surface of PNZT thin film with composition $Pb_{0.985}(Zr_{0.53}Ti_{0.47})_{0.97}Nb_{0.03}O_3$ and sintered at 600 °C for 3 h.

The thickness measurements were done using SEM micrographs. Figure 4.32 shows the cross-section of a PNZT thin film containing three layers. The film was dense and uniform. Slight peeling of the film from the substrate was observed because the film was fractured while getting the cross-section of it.

Figure 4.33 is a more revealing image about the thickness and uniformity of the films. In this image, PNZT film with a thickness of 390 nm (double layered) was shown. The film had a dense structure and a consistent uniformity throughout the entire film.

To achieve an optimum thickness value, single and multilayered films up to four layers were produced. Figures 4.34 to 4.37 show the cross sectional SEM images of PNZT thin films. Thickness values were estimated approximately between 250 and 870 nm. The thickness was measured as 250 nm in single layered films produced by spin coating at a rate of 1500 rpm for 30 seconds. For the entire study the molarity and the spin coating conditions were held constant. 390 nm thickness value was obtained for two layered PNZT thin films. Three and four layered films had a thickness of 520 and 870 nm, respectively.

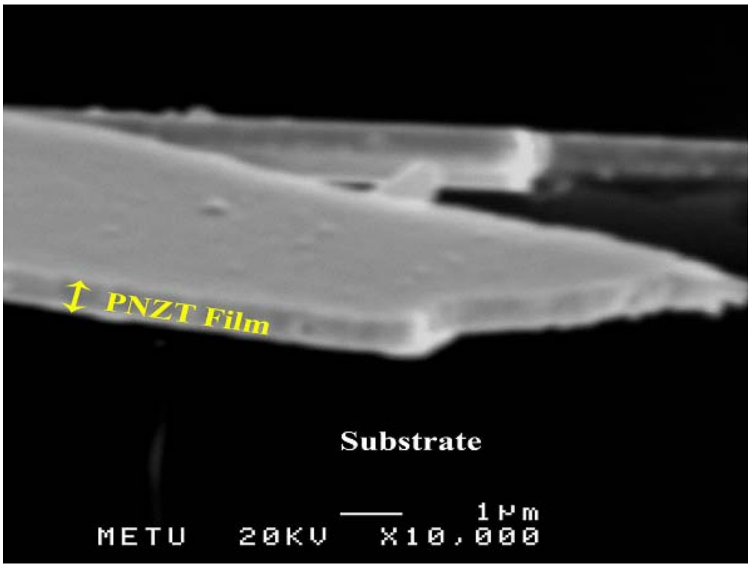

Figure 4.32 Cross sectional view of $Pb_{0.985}(Zr_{0.53}Ti_{0.47})_{0.97}$ $Nb_{0.03}O_3$-520 nm thick PNZT film sintered at 600 °C for 3 h.

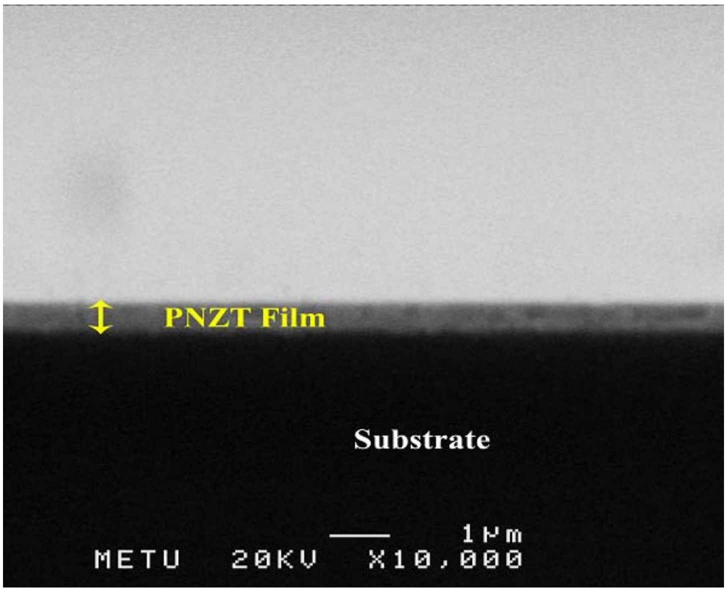

Figure 4.33 Cross sectional view of $Pb_{0.985}(Zr_{0.53}Ti_{0.47})_{0.97}$ $Nb_{0.03}O_3$-390 nm thick PNZT film sintered at 600 °C for 1 h.

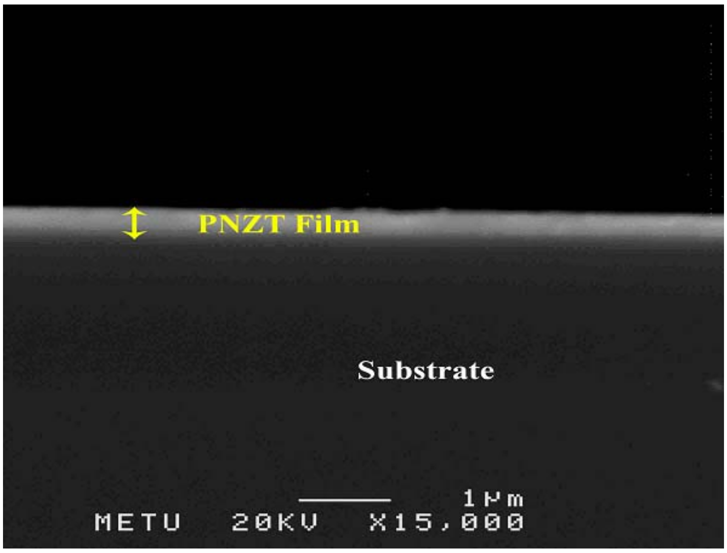

Figure 4.34 Cross sectional view of $Pb_{0.985}(Zr_{0.53}Ti_{0.47})_{0.97}Nb_{0.03}O_3$-250 nm thick (single layered) PNZT film sintered at 600 °C for 1 h.

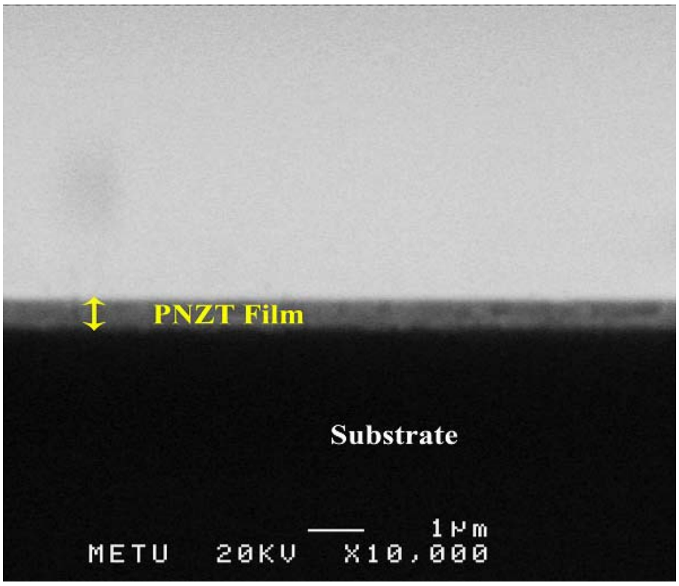

Figure 4.35 Cross sectional view of $Pb_{0.985}(Zr_{0.53}Ti_{0.47})_{0.97}Nb_{0.03}O_3$-390 nm thick (double layered) PNZT film sintered at 600 °C for 1 h.

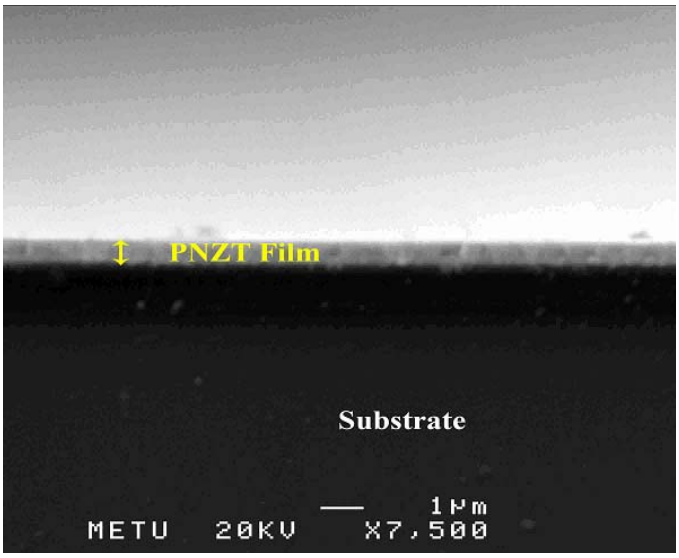

Figure 4.36 Cross sectional view of $Pb_{0.985}(Zr_{0.53}Ti_{0.47})_{0.97}Nb_{0.03}O_3$-520 nm thick (three layered) PNZT film sintered at 600 °C for 1 h.

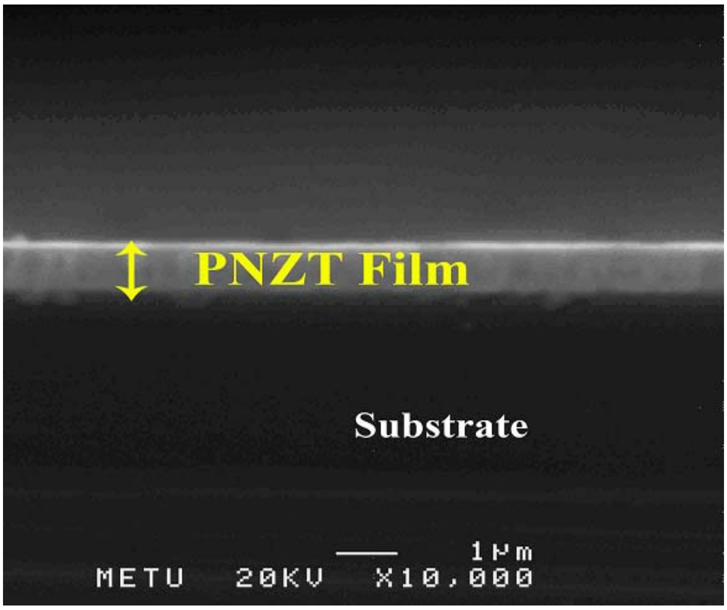

Figure 4.37 Cross sectional view of $Pb_{0.985}(Zr_{0.53}Ti_{0.47})_{0.97}Nb_{0.03}O_3$-870 nm thick (four layered) PNZT film sintered at 600 °C for 1 h.

The average size of the grains can not be measured by SEM because they are too small to be observed by the maximum magnification of SEM. FESEM images of PNZT thin films were used to analyze the surface morphology and to measure the grain size of the films.

Figures 4.38 to 4.41 show the images obtained using FESEM. Grain sizes were estimated by quantitative metallographic method. True grain size of films was determined from the equation,

$$d = 1.22\overline{d} \qquad \text{Eq. [4.1]}$$

which were given in Table 4.3 according to the calculations of Mora et al [41]. The average grain size of 1 at % Nb doped PNZT thin film was determined as 130 nm. It is found in the literature that, the grain size of PNZT films changes between 100 and 200 nm [4, 6, 7]. The use of Pt as a substrate allows for easy nucleation of the perovskite phase because of the approximate lattice parameters of $PbTiO_3$ and Pt [7]. Since Ti makes nucleation easier, the surface number density of nuclei increases in PNZT thin films leading to a fine grained perovskite structure [6, 7, 22]. For the undoped PZT films, grain size of 100 nm is achieved. For 3 and 5 at % Nb doping, grain sizes of 120 and 85 nm, respectively, were obtained. For 7% Nb doped PNZT films, the grains couldn’t be detected because of the very fine pyrochlore phase at the film surface [4] or the defects and dust at the surface. Grain size decreases with increasing Nb content starting from 1 at % Nb addition. This can be explained by the previous studies that, Nb is an effective grain growth inhibitor. Nb^{5+} ions can concentrate near the grain boundaries and reduce the mobility of grains [42].

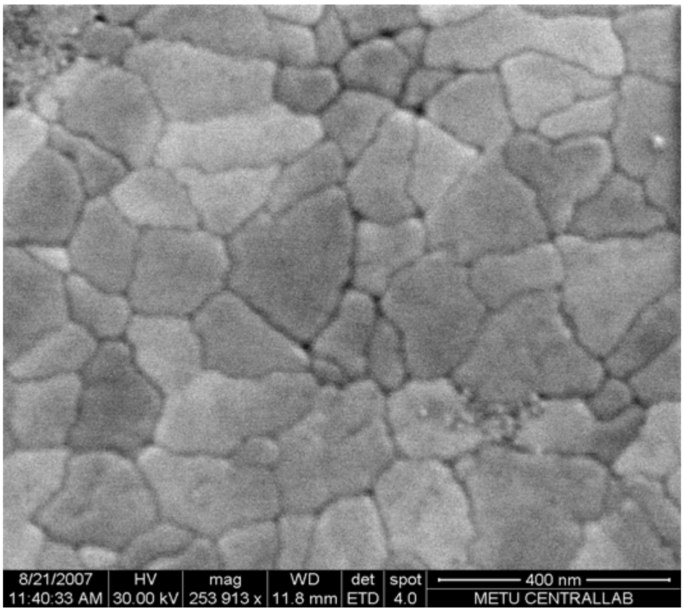

Figure 4.38 FESEM image of PZT thin film with composition $Pb(Zr_{0.53}Ti_{0.47})O_3$ sintered at 600 °C for 1 h.

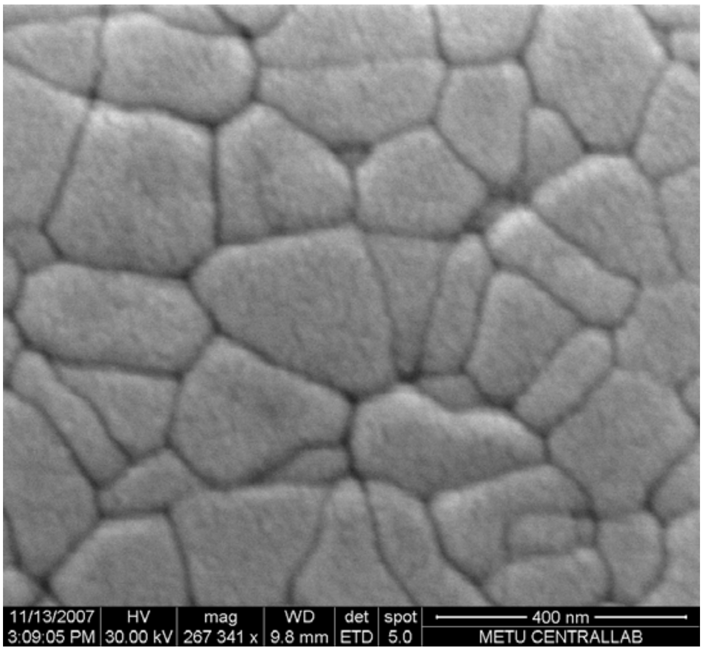

Figure 4.39 FESEM image of PNZT thin film with composition $Pb_{0.995}(Zr_{0.53}Ti_{0.47})_{0.99}Nb_{0.01}O_3$ sintered at 600 °C for 1 h.

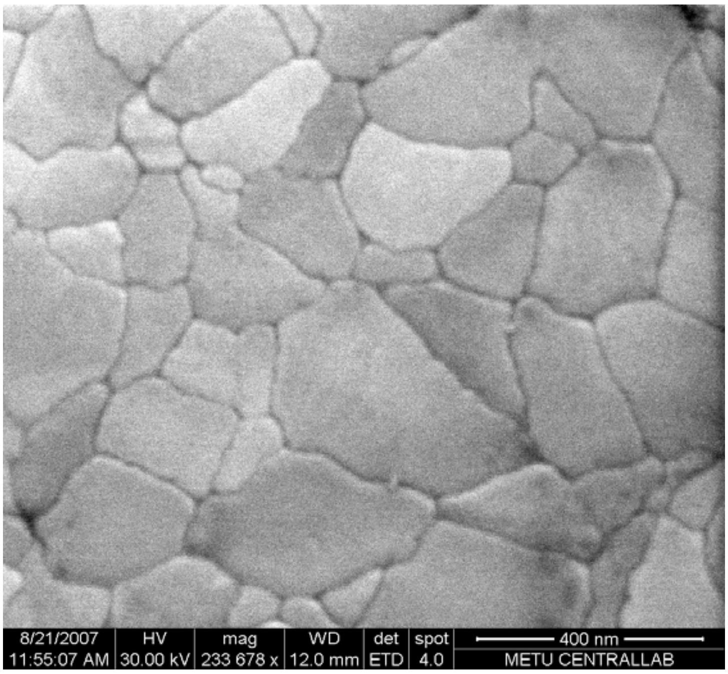

Figure 4.40 FESEM image of PNZT thin film with composition $Pb_{0.985}(Zr_{0.53}Ti_{0.47})_{0.97}Nb_{0.03}O_3$ sintered at 600 °C for 1 h.

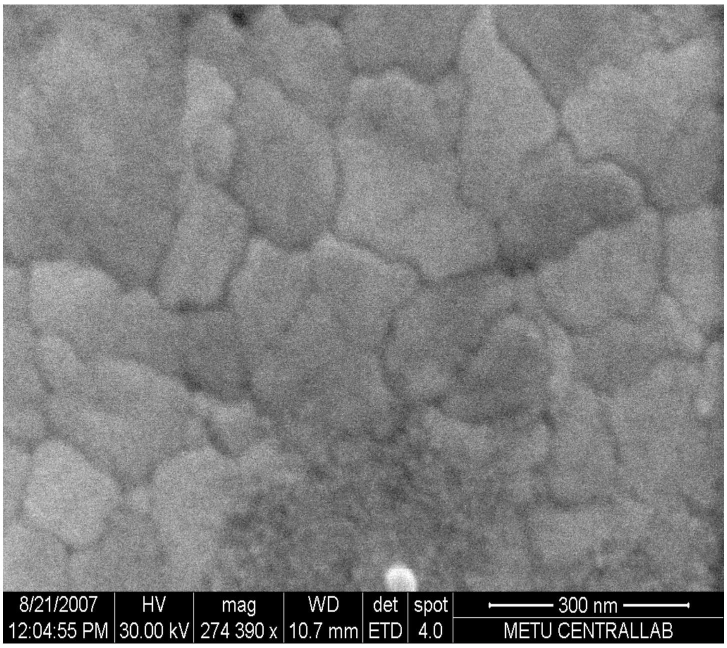

Figure 4.41 FESEM image of PNZT thin film with composition $Pb_{0.975}(Zr_{0.53}Ti_{0.47})_{0.95}Nb_{0.05}O_3$ sintered at 600 °C for 1 h.

Table 4.3 The results of the grain size measurements with varying niobium content.

Nb content (at %)	Composition	Grain Size (nm)
0	$Pb(Zr_{0.53}Ti_{0.47})O_3$	100
1	$Pb_{0.995}(Zr_{0.53}Ti_{0.47})_{0.99}Nb_{0.01}O_3$	130
3	$Pb_{0.985}(Zr_{0.53}Ti_{0.47})_{0.97}Nb_{0.03}O_3$	120
5	$Pb_{0.975}(Zr_{0.53}Ti_{0.47})_{0.95}Nb_{0.05}O_3$	85
7	$Pb_{0.965}(Zr_{0.53}Ti_{0.47})_{0.93}Nb_{0.07}O_3$	-

4.6 Dielectric Properties of PNZT Thin Films

Dielectric properties of PNZT thin films were measured by Agilent 4294A impedance analyzer. Dielectric constant (ε_r) and tangent loss ($\tan\delta$) values were obtained in the frequency range 1 kHz-500 kHz with an oscillation voltage of 0.05 V in order to compare the dielectric properties of the films. Table 4.4 shows the dielectric constant and tangent loss values of PNZT thin films between 1 kHz and 500 kHz.

The effect of sintering temperature and sintering time on dielectric constant and tangent loss values of PNZT thin films were investigated initially. Thickness (390 nm) and Nb content (3 at %) were kept constant. The films were sintered at temperatures of 600, 650 and 700 °C. Sintering periods were taken as 1, 2 and 3 h.

Table 4.4 Dielectric properties of $Pb_{(1-0.5x)}(Zr_{0.53}Ti_{0.47})_{1-x}Nb_xO_3$ thin films.

Composition	**Film Thickness (nm)**	**Heat Treatment**		**Dielectric Constant**				**Tangent Loss (%)**			
		Temperature (°C)	**Time (hr)**	**1 kHz**	**10 kHz**	**100 kHz**	**500 kHz**	**1 kHz**	**10 kHz**	**100 kHz**	**500 kHz**
$Pb_{0.985}(Zr_{0.53}Ti_{0.47})_{0.97}Nb_{0.03}O_3$	390	600	1	605	588	562	620	2.5	3.1	4.9	8.9
$Pb_{0.985}(Zr_{0.53}Ti_{0.47})_{0.97}Nb_{0.03}O_3$	390	600	2	487	473	447	407	1.6	3.1	5.6	8.4
$Pb_{0.985}(Zr_{0.53}Ti_{0.47})_{0.97}Nb_{0.03}O_3$	390	600	3	599	581	553	608	2.9	3.2	5.4	8.1
$Pb_{0.985}(Zr_{0.53}Ti_{0.47})_{0.97}Nb_{0.03}O_3$	390	650	1	563	548	521	476	3.7	3.6	4.3	8.1
$Pb_{0.985}(Zr_{0.53}Ti_{0.47})_{0.97}Nb_{0.03}O_3$	390	650	2	609	590	567	627	3.1	3.1	4.7	8.4
$Pb_{0.985}(Zr_{0.53}Ti_{0.47})_{0.97}Nb_{0.03}O_3$	390	650	3	403	391	371	385	2.5	3.3	5.4	8.1
$Pb_{0.985}(Zr_{0.53}Ti_{0.47})_{0.97}Nb_{0.03}O_3$	390	700	1	608	603	573	646	3.2	3.6	4.2	6.8
$Pb_{0.985}(Zr_{0.53}Ti_{0.47})_{0.97}Nb_{0.03}O_3$	390	700	2	579	559	529	483	5.1	3.6	4.7	7.9
$Pb_{0.985}(Zr_{0.53}Ti_{0.47})_{0.97}Nb_{0.03}O_3$	390	700	3	593	577	560	629	2.2	2.5	3.7	7.3
$Pb_{0.985}(Zr_{0.53}Ti_{0.47})_{0.97}Nb_{0.03}O_3$	250	600	1	341	331	319	346	2.1	2.6	4.5	8.8
$Pb_{0.985}(Zr_{0.53}Ti_{0.47})_{0.97}Nb_{0.03}O_3$	520	600	1	572	560	542	577	1.2	2.2	3.9	7.1
$Pb_{0.985}(Zr_{0.53}Ti_{0.47})_{0.97}Nb_{0.03}O_3$	870	600	1	1275	1028	1004	1104	2.7	2.2	2.8	4.7
$Pb(Zr_{0.53}Ti_{0.47})O_3$	390	600	1	502	484	458	483	2.9	3.4	5.7	10.1
$Pb_{0.995}(Zr_{0.53}Ti_{0.47})_{0.99}Nb_{0.01}O_3$	390	600	1	689	665	635	726	3.5	3.8	5.6	8.9
$Pb_{0.975}(Zr_{0.53}Ti_{0.47})_{0.95}Nb_{0.05}O_3$	390	600	1	521	517	498	543	2.8	3.2	5.6	8.4
$Pb_{0.965}(Zr_{0.53}Ti_{0.47})_{0.93}Nb_{0.07}O_3$	390	600	1	406	401	405	446	2.9	2.4	2.9	5.1

Dielectric constant (ε_r) of the films was calculated by using the following equation:

$$C = \varepsilon_r \times \varepsilon_0 \times \frac{A}{d} \qquad \text{Eq. [4.1]}$$

where C = capacitance of the film

ε_0 = permittivity of vacuum = 8.854×10^{-12} F/m

A = electrode area

d = film thickness

Figure 4.42 and Figure 4.43 show the variation of capacitance and dielectric constant of PNZT thin films with the change of AC frequencies as a function of sintering temperature where sintering period is 1 h. Dielectric constant values were close to each other (~605) in films sintered at 600 °C and 700 °C for 1 h. Dielectric constant decreases to 563 in films sintered at 650 °C. This decrease can be explained by the low perovskite peak intensity and appearance of Ti_2O_3 phase in the XRD results. The increase of dielectric constant for films sintered at 700 °C can be explained by the decrease of pyrochlore intensity. However, since any pyrochlore phase is not wanted for PNZT films, the optimum sintering temperature was determined as 600 °C. Tangent loss values of the PNZT films with changing frequencies at different sintering temperatures were given in Figure 4.44. At low frequencies, tangent loss values were found around 4 % and as the frequency increases, tangent loss values also increase and reach to 8 %.

Tangent loss values were expected to be constant for frequencies up to 500 kHz and a sharp increase after 500 kHz. However, an increase of tangent loss was observed in all of PNZT films in 1 kHz-500 kHz frequency range. Several explanations exist for that dispersion, including finite resistance of the electrodes, the presence of a barrier layer between the insulating film and the electrode surface, or leaky grain boundaries [13].

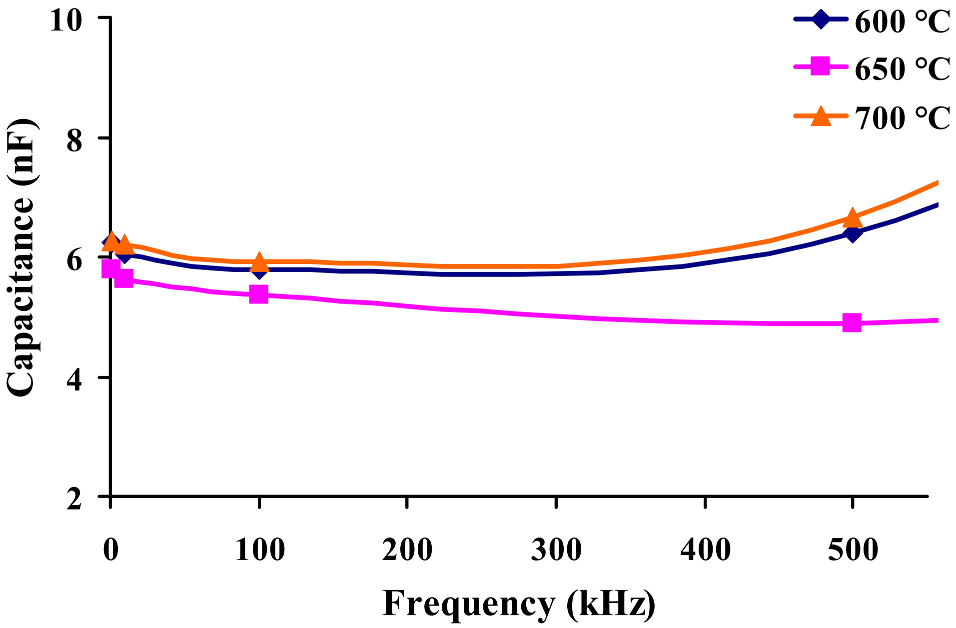

Figure 4.42 Capacitance-frequency curves of PNZT [$Pb_{0.985}(Zr_{0.53}Ti_{0.47})_{0.97}Nb_{0.03}O_3$] films sintered at different temperatures for 1 h.

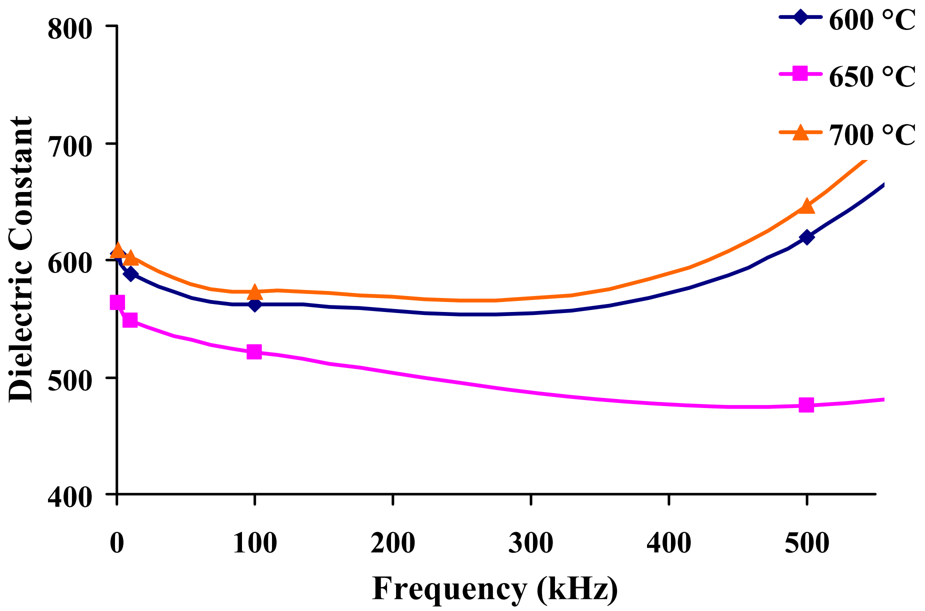

Figure 4.43 Dielectric constant-frequency curves of PNZT [$Pb_{0.985}(Zr_{0.53}Ti_{0.47})_{0.97}Nb_{0.03}O_3$] films sintered at different temperatures for 1 h.

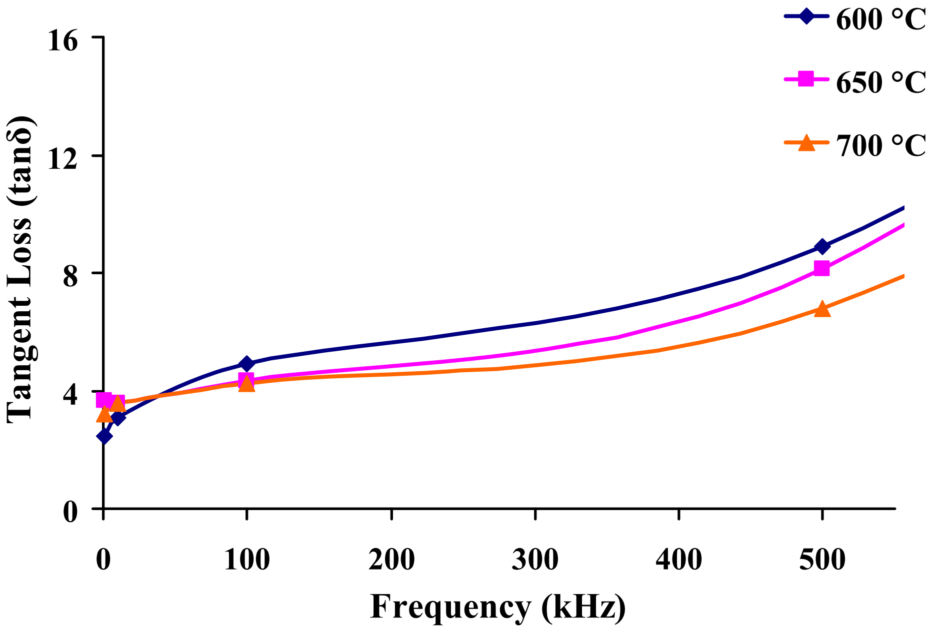

Figure 4.44 Tangent loss-frequency curves of PNZT [$Pb_{0.985}(Zr_{0.53}Ti_{0.47})_{0.97}Nb_{0.03}O_3$] films sintered at different temperatures for 1 h.

Tangent loss of the films arises from two mechanisms which are resistive loss and relaxation loss. Resistive loss mechanism involves energy consumption by the mobile charges in the film; whereas, in the case of relaxation loss mechanism, it is the relaxation of dipole which dissipates the energy. If there are very few charges in the films then the latter mechanism is dominating. The resistive loss mechanism is directly connected to the leakage current of the film: if the leakage current is higher the loss is also higher. Alternatively, if the dielectric constant of the film is large, then an increase in dielectric loss is obvious due to the contribution from the relaxation mechanism. Enhanced polarization increases the dissipation during the relaxation [43].

To find which mechanism is dominating for PNZT thin films, leakage current analysis were done. Leakage current decreases as Nb content increases that will be given in leakage current analysis. It can be seen from Table 4.4 that Nb content has no effect on tangent loss. However, it is observed that as the dielectric constant increases, tangent loss also increases showing that relaxation mechanism is dominant for the PNZT thin films.

Figure 4.45 and Figure 4.46 show the variation of capacitance and dielectric constant of PNZT thin films with the change of AC frequencies as a function of sintering time at 600 °C. Highest dielectric constant value was achieved in films sintered for 1 h as 605. It is decreasing to 487 in films sintered for 2 h because of the pyrochlore (Ti_2O_3) phase appeared in XRD results and increasing back to 598 for 3 h. Tangent loss values of PNZT films with changing frequencies at different sintering periods at 600 °C were given in Figure 4.47.

Figure 4.48 and Figure 4.49 show the effect of thickness on capacitance and dielectric constant values with changing frequencies. Change of tangent loss values with changing frequencies were given in Figure 4.50. Dielectric constant values increase with increasing thickness except for 3-layered (520 nm) PNZT film as shown in Figure 4.51. The maximum value was achieved for 4 layered films (870 nm) as 1275.

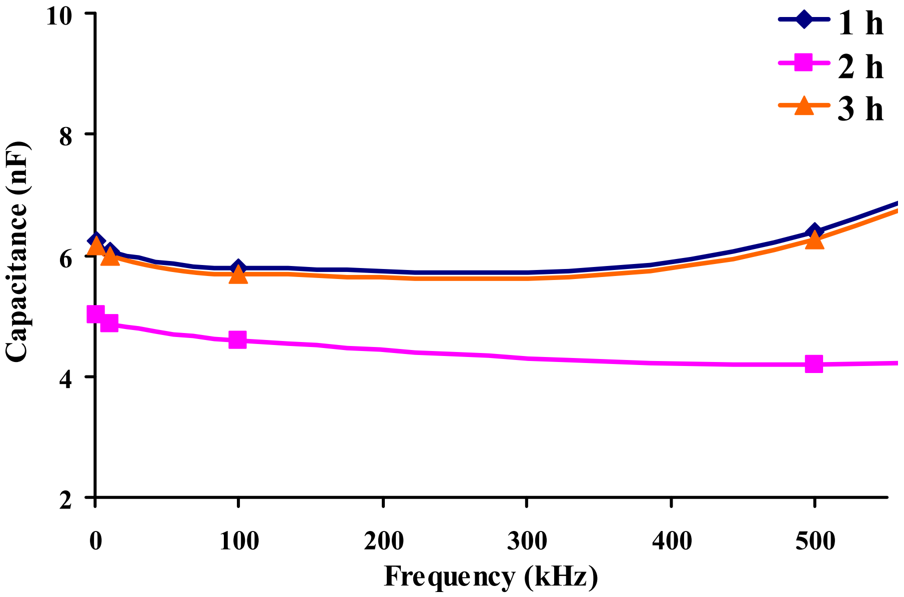

Figure 4.45 Capacitance-frequency curves of PNZT [$Pb_{0.985}(Zr_{0.53}Ti_{0.47})_{0.97}Nb_{0.03}O_3$] films sintered for different periods at 600 °C.

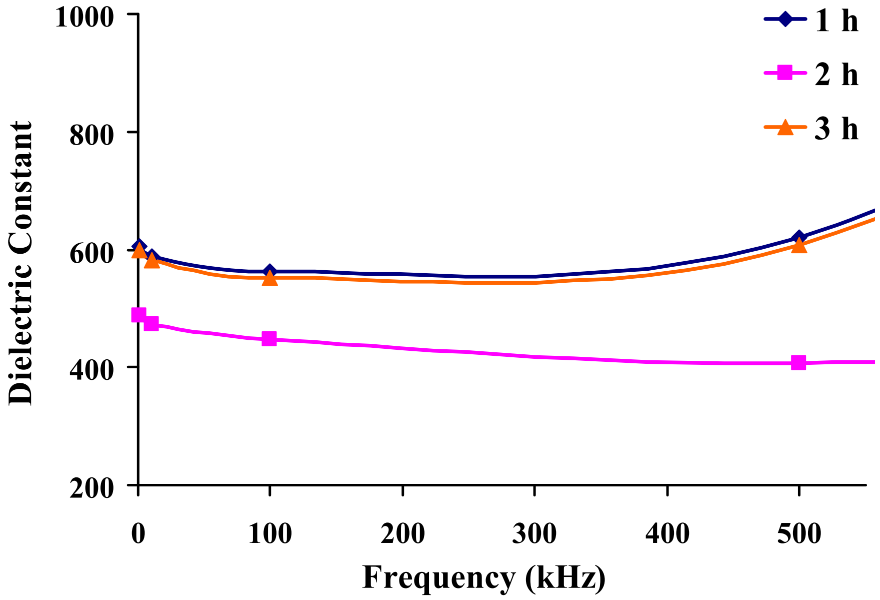

Figure 4.46 Dielectric constant-frequency curves of PNZT [$Pb_{0.985}(Zr_{0.53}Ti_{0.47})_{0.97}Nb_{0.03}O_3$] films sintered for different periods at 600 °C.

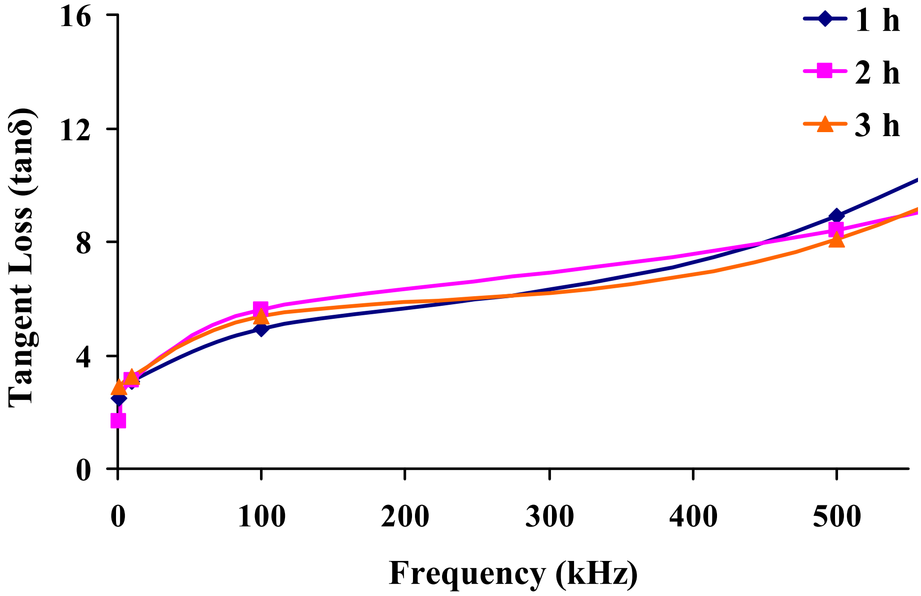

Figure 4.47 Tangent loss-frequency curves of PNZT [$Pb_{0.985}(Zr_{0.53}Ti_{0.47})_{0.97}Nb_{0.03}O_3$] films sintered for different periods at 600 °C.

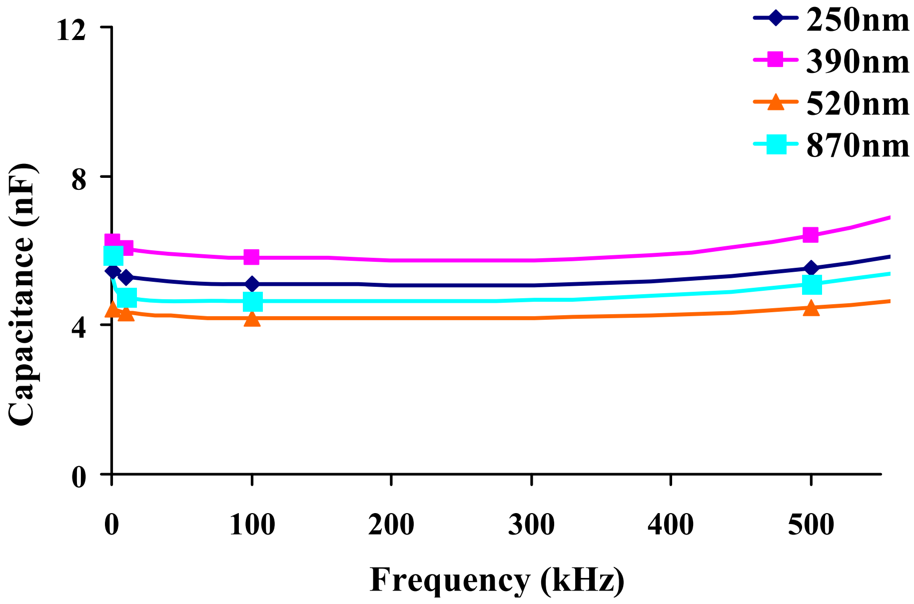

Figure 4.48 Capacitance-frequency curves of PNZT [$Pb_{0.985}(Zr_{0.53}Ti_{0.47})_{0.97}Nb_{0.03}O_3$] films sintered at 600 °C for 1 h for different film thicknesses.

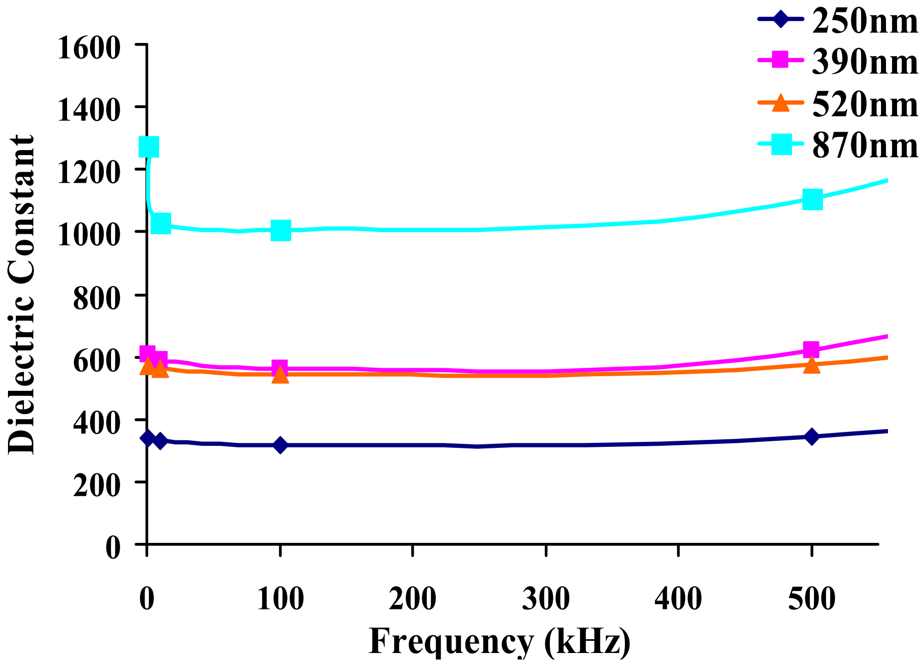

Figure 4.49 Dielectric constant-frequency curves of PNZT [$Pb_{0.985}(Zr_{0.53}Ti_{0.47})_{0.97}Nb_{0.03}O_3$] films sintered at 600 °C for 1 h for different film thicknesses.

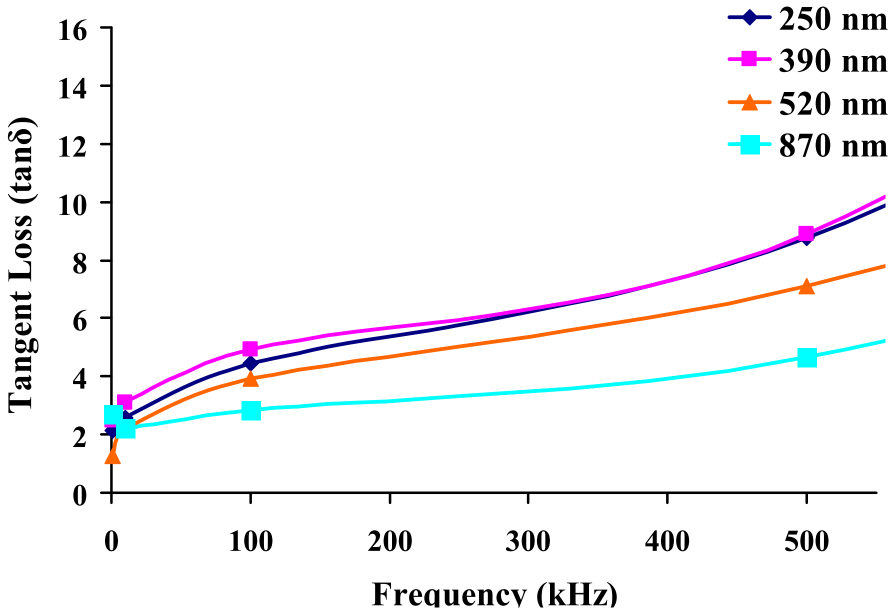

Figure 4.50 Tangent loss-frequency curves of PNZT [$Pb_{0.985}(Zr_{0.53}Ti_{0.47})_{0.97}Nb_{0.03}O_3$] films sintered at 600 °C for 1 h for different film thicknesses.

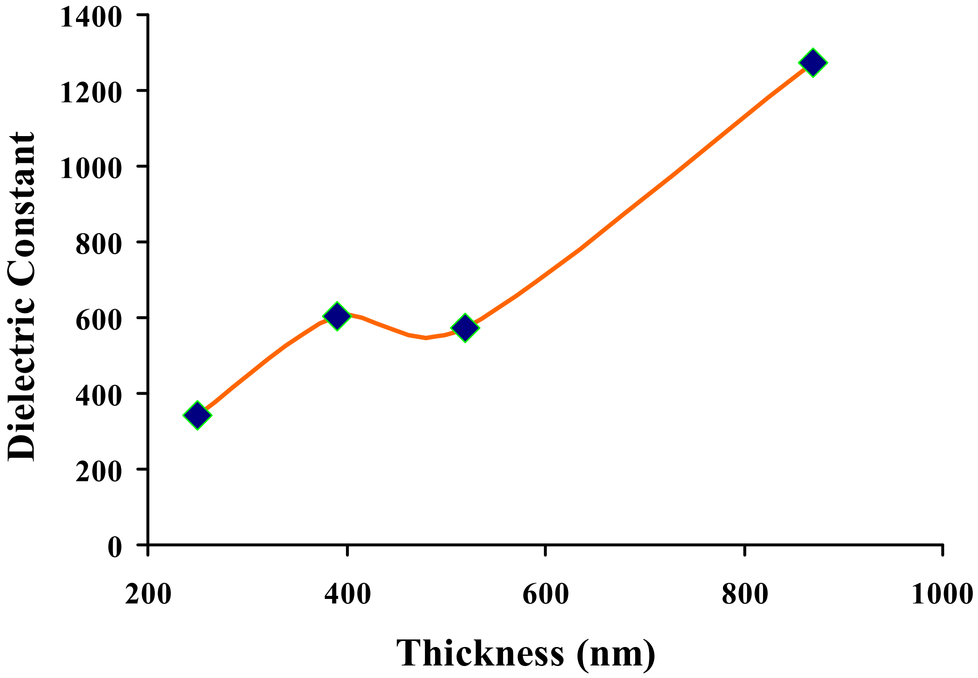

Figure 4.51 Change of dielectric constant values of PNZT [$Pb_{0.985}(Zr_{0.53}Ti_{0.47})_{0.97}$ $Nb_{0.03}O_3$] films sintered at 600 °C for 1 h with changing film thickness.

The increase in dielectric constant can be explained by formation of denser films, because number of layers and pyrolysis cycles increases as the thickness increases. Increased number of layers leads to a decrease in film porosity in solution deposition technique since subsequent layers coated on the former pyrolysed layer covers up the pores and bulk defects left behind by the organic burn-off [43]. This increase is consistent with the previous studies [5, 21, 43] .

Figures 4.52 and 4.53 show the variation of capacitance and dielectric constant of PNZT thin films with the change of AC frequencies as a function of Nb content. The double layered PNZT thin films (390 nm) were sintered at 600 °C for 1 h for all compositions. The highest dielectric constant was achieved in 1 at % Nb doped films. Up to 5 at % Nb doped films, dielectric constant is higher than the undoped one, however for 7 at % Nb doped films, dielectric constant reaches its minimum value of 405. Figure 4.54 shows the change of tangent loss values with the change of frequency as a function of Nb content which were given in Table 4.4.

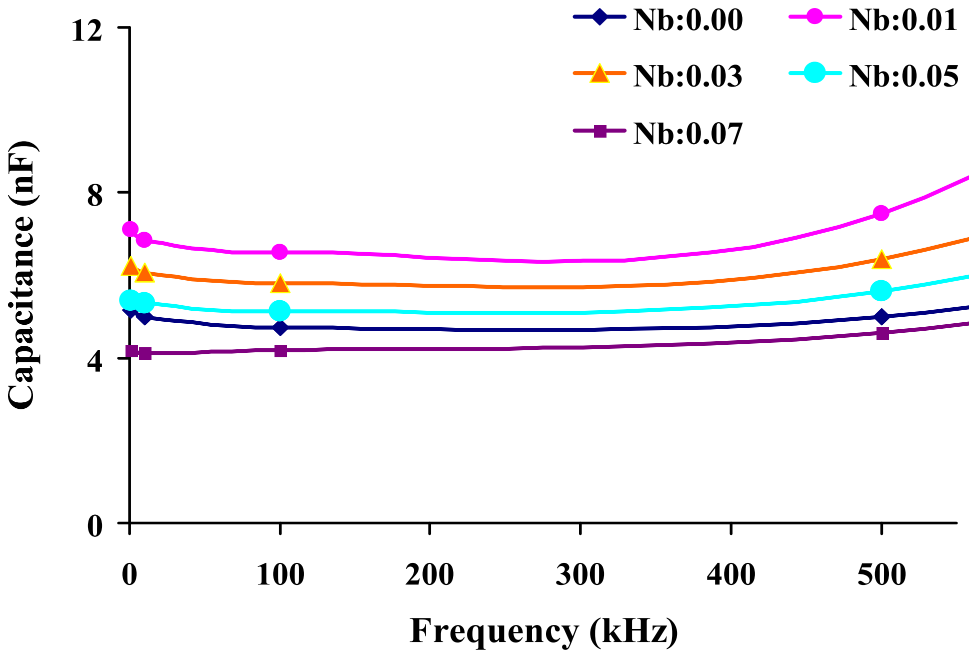

Figure 4.52 Capacitance-frequency curves of PNZT [$Pb_{0.985}(Zr_{0.53}Ti_{0.47})_{0.97}Nb_{0.03}O_3$] films sintered at 600 °C for 1 h for different Nb content additions.

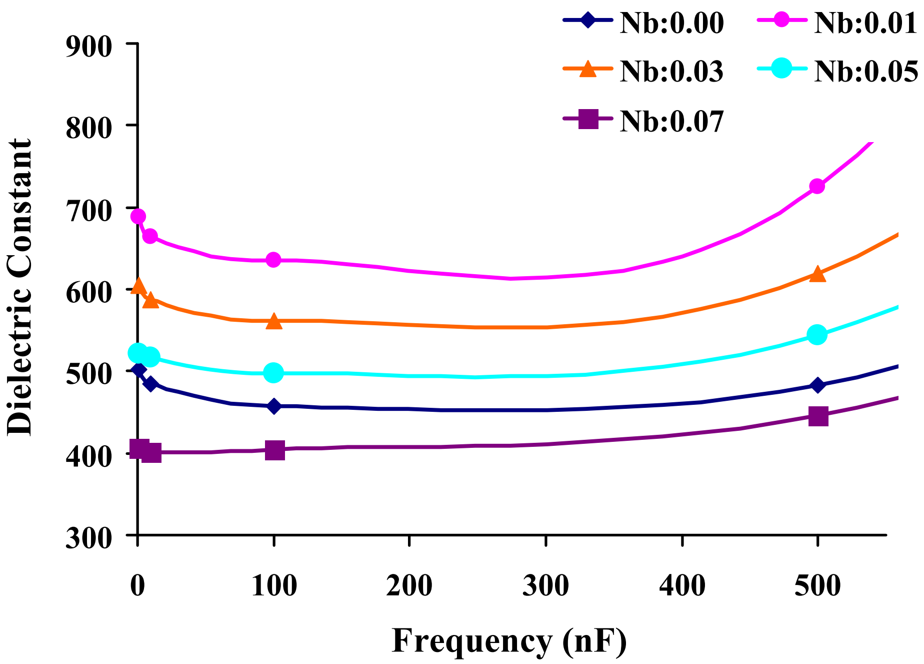

Figure 4.53 Dielectric constant-frequency curves of PNZT [$Pb_{0.985}(Zr_{0.53}Ti_{0.47})_{0.97}Nb_{0.03}O_3$] films sintered at 600 °C for 1 h for different Nb content additions.

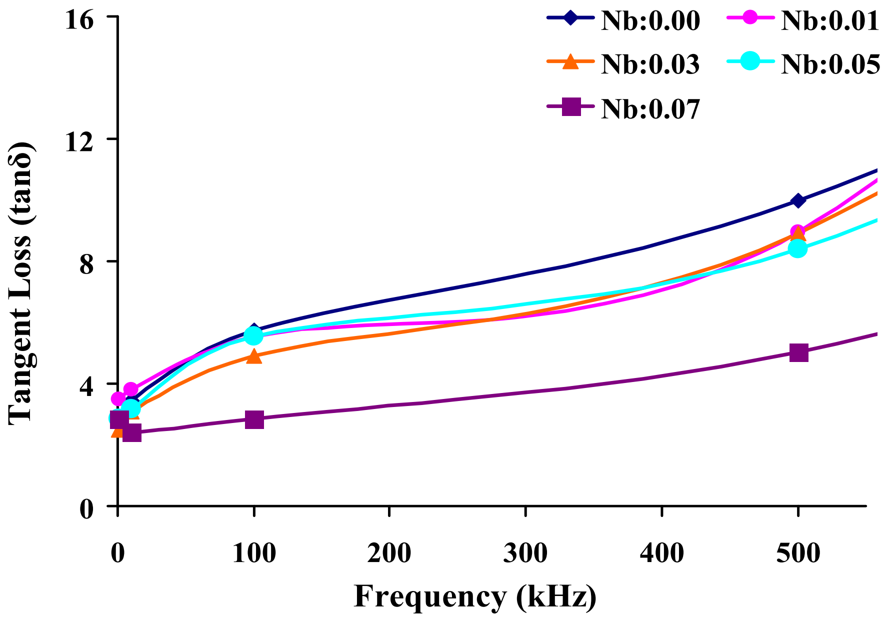

Figure 4.54 Tangent loss-frequency curves of PNZT [$Pb_{0.985}(Zr_{0.53}Ti_{0.47})_{0.97}Nb_{0.03}O_3$] films sintered at 600 °C for 1 h for different Nb content additions.

Figure 4.55 shows the change of dielectric constant values at 1 kHz with respect to Nb concentration. For the undoped films, a dielectric constant of 502 was obtained. For 1 at % Nb doped films, the maximum dielectric constant value was reached as 689. For higher doping concentrations (>1 at %), dielectric constant decreases almost linearly. Previous studies [4, 7, 21, 22, 34] also stated that for low Nb concentrations dielectric constant reaches a maximum point and for higher Nb doping levels ε_r decreases. The reason of the decrease in dielectric constant can be the decrease of grain size, the deterioration of the crystal structure and pinning of the domains by the increase of defects and oxygen vacancies as the Nb content increases. Figure 4.56 shows the change of tangent loss with varying Nb content. It can be seen that the tangent loss values lie between 2 and 4 % indicating that Nb doping has almost no effect on tangent loss values which is also given by Haccart et al [22]. The maximum tangent loss values were reached for 1 at % Nb doping as 3.5%.

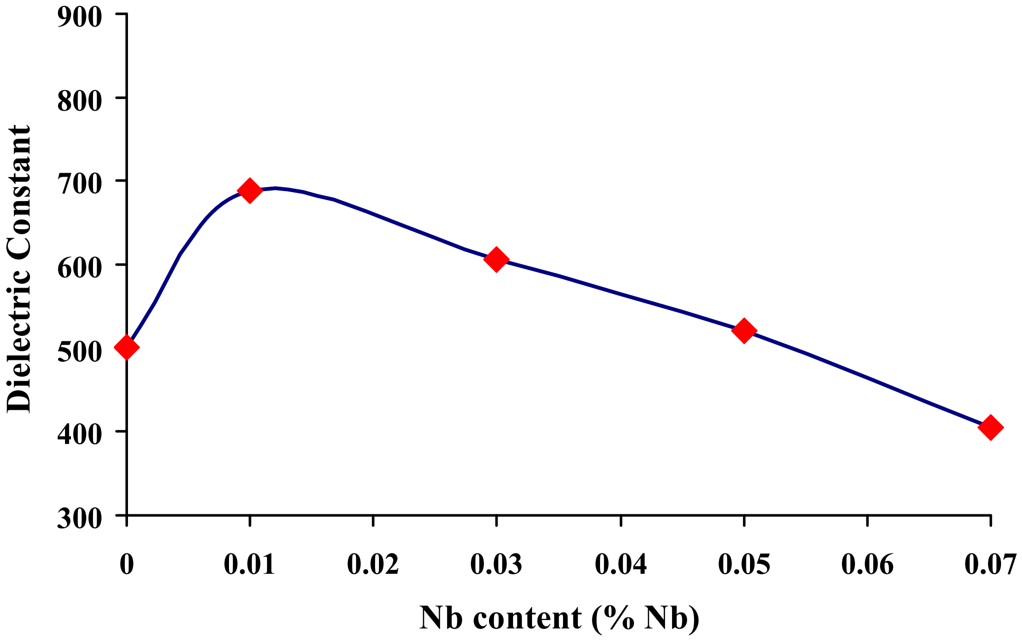

Figure 4.55 Change of dielectric constant (ε_r) values of PNZT films at 1 kHz with varying Nb content while the sintering temperature, sintering time and thickness were held constant.

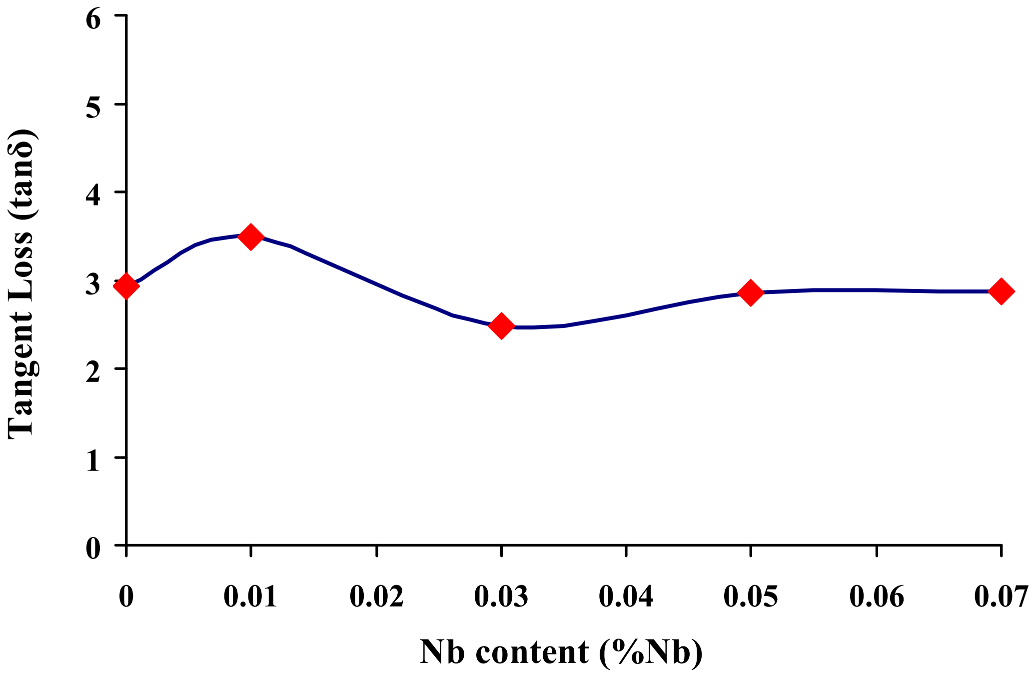

Figure 4.56 Change of tangent loss (tanδ) values of PNZT thin films at 1 kHz with varying Nb content while the sintering temperature, sintering time and thickness were held constant.

4.7 Ferroelectric Properties of PNZT thin films

The ferroelectric properties of PNZT thin films were investigated using hysteresis loops (polarization-electric field) and capacitance-voltage (C-V) curves. To find the optimum sintering temperature and sintering time for the films, remnant polarization (P_r) and coercive field (E_c) values were measured. Three sintering temperatures (600, 650 and 700 °C) and sintering periods (1, 2 and 3 h) were applied to the films. Table 4.5 shows the results of heat treatment conditions on remnant polarization and coercive field at various applied voltages.

Table 4.5 Ferroelectric properties of $Pb_{(1-0.5x)}\,(Zr_{0.53}\,Ti_{0.47})_{1-x}\,Nb_x\,O_3$ thin films.

Composition	Film Thickness (nm)	Heat Treatment		Remnant Polarization (P_r)			Coercive Field (E_c)		
		Temperature (°C)	Time (h)	5V	10 V	15 V	5V	10 V	15 V
$Pb_{0.985}(Zr_{0.53}Ti_{0.47})_{0.97}Nb_{0.03}O_3$	390	600	1	13.67	15.74	20.96	42.21	42.96	68.36
$Pb_{0.985}(Zr_{0.53}Ti_{0.47})_{0.97}Nb_{0.03}O_3$	390	600	2	3.88	13.58	20.60	12.08	40.63	75.36
$Pb_{0.985}(Zr_{0.53}Ti_{0.47})_{0.97}Nb_{0.03}O_3$	390	600	3	7.41	17.37	24.53	20.39	52.14	75.35
$Pb_{0.985}(Zr_{0.53}Ti_{0.47})_{0.97}Nb_{0.03}O_3$	390	650	1	9.70	18.96	25.18	27.65	52.22	73.59
$Pb_{0.985}(Zr_{0.53}Ti_{0.47})_{0.97}Nb_{0.03}O_3$	390	650	2	13.20	23.09	27.95	24.78	60.55	68.16
$Pb_{0.985}(Zr_{0.53}Ti_{0.47})_{0.97}Nb_{0.03}O_3$	390	650	3	10.20	16.92	21.36	33.00	44.27	59.43
$Pb_{0.985}(Zr_{0.53}Ti_{0.47})_{0.97}Nb_{0.03}O_3$	390	700	1	7.88	19.53	22.45	19.75	57.55	74.83
$Pb_{0.985}(Zr_{0.53}Ti_{0.47})_{0.97}Nb_{0.03}O_3$	390	700	2	12.01	19.39	22.81	26.35	51.41	60.69
$Pb_{0.985}(Zr_{0.53}Ti_{0.47})_{0.97}Nb_{0.03}O_3$	390	700	3	12.80	18.58	23.74	28.82	54.65	72.89
$Pb_{0.985}(Zr_{0.53}Ti_{0.47})_{0.97}Nb_{0.03}O_3$	250	600	1	11.69	-	-	25.00	-	-
$Pb_{0.985}(Zr_{0.53}Ti_{0.47})_{0.97}Nb_{0.03}O_3$	520	600	1	3.34	12.43	15.87	11.18	45.97	55.58
$Pb_{0.985}(Zr_{0.53}Ti_{0.47})_{0.97}Nb_{0.03}O_3$	870	600	1	1.32	4.13	6.97	5.33	12.23	18.05
$Pb(Zr_{0.53}Ti_{0.47})O_3$	390	600	1	16.30	33.08	35.12	26.22	75.34	82.35
$Pb_{0.995}(Zr_{0.53}Ti_{0.47})_{0.99}Nb_{0.01}O_3$	390	600	1	20.6	33.38	35.75	27.40	51.33	76.65
$Pb_{0.975}(Zr_{0.53}Ti_{0.47})_{0.95}Nb_{0.05}O_3$	390	600	1	2.72	10.66	17.06	6.37	33.30	70.12
$Pb_{0.965}(Zr_{0.53}Ti_{0.47})_{0.93}Nb_{0.07}O_3$	390	600	1	4.54	11.03	18.03	20.43	57.42	87.38

Capacitance-voltage curves were obtained in order to assure the ferroelectricity of the films. C-V curves were obtained by applying DC bias voltage in the range of 10 V to -10 V. Initially, the DC bias was increased from 0 V to 10 V in 0.8 V intervals, and then decreased again to 0 V and increased in the reverse polarity down to -10 V. C-V profile is a measure of dP/dE, so the peak in the C-V characteristic corresponds to a large polarization change, or the switching of ferroelectric domains from one orientation to another.

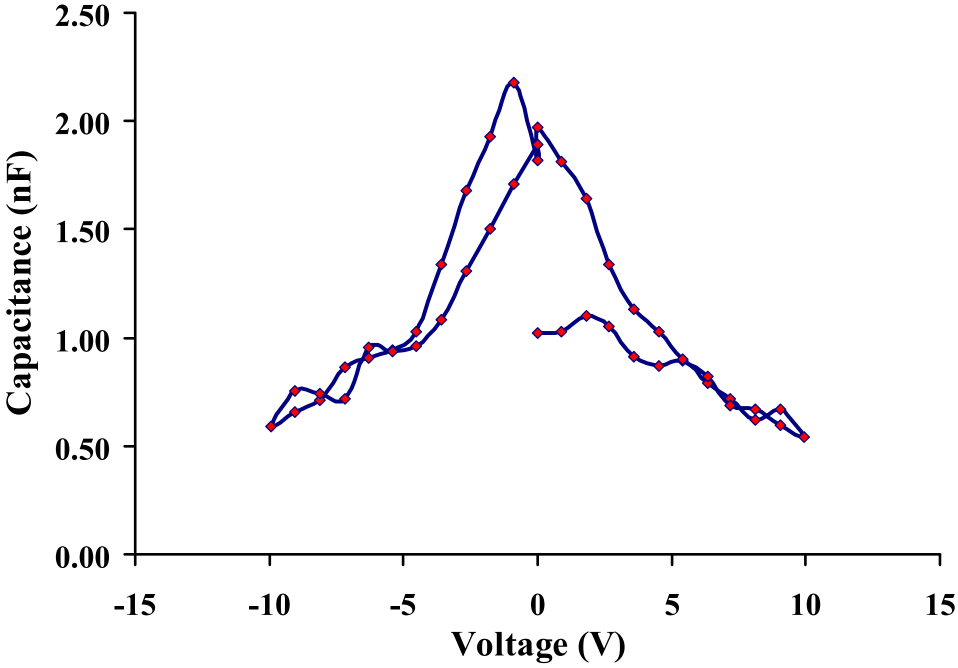

Figure 4.57 The C-V curve for a PNZT thin film that has the composition of $Pb_{0.995}(Zr_{0.53}Ti_{0.47})_{0.99}Nb_{0.01}O_3$ and sintered at 600 °C for 1 h.

Figure 4.57 shows the C-V curve of a PNZT thin film that has the composition of $Pb_{0.995}(Zr_{0.53}Ti_{0.47})_{0.99}Nb_{0.01}O_3$ and sintered at 600 °C for 1 h. This film has a thickness of 390 nm. Ferroelectric thin films possess a butterfly shaped curve. In this study all of the C-V curves were found to be butterfly shaped. However, there is a capacitance difference between the start and the end of the C-V measurements. It was observed, in all of the films that there is an asymmetry of the C-V curve along voltage axis. This shift can be seen in hysteresis loops along electric field axis. The same behavior is also observed by other workers [6, 7, 22]. This shift can be named as internal electric field (E_{int}) or internal bias field. It is stated that the reason of the asymmetric behavior in PZT and PNZT films is due to the space charges. One example is the oxygen vacancies at the interface between electrode and film [6, 22].

Figure 4.58 shows the effect of sintering temperature on the ferroelectric properties at 5 V. The curves were similarly shaped but the remnant polarization and coercive field values were changing. It is seen from Figure 4.59 that the remnant polarization and coercive field values were decreasing as the sintering temperature increases. All of the films were 390 nm in thickness and voltage applied to the films was ranging from -5 to +5 V. For PNZT thin films, saturation of the hysteresis loops could not be achieved with the maximum applied field of 382 kV/cm (15 V).

The highest P_r value was found as 13.67 μC/cm^2 for the films sintered at 600 °C for 1 h as supported by XRD studies which yield pure perovskite phase for films sintered at the same conditions. Obtained P_r and E_c values were varying for different sintering conditions as given in Table 4.5. Remnant polarization values were decreasing from 13.67 μC/cm^2 to 7.88 μC/cm^2 as the sintering temperature increased. Coercive field values were also decreased from 42.21 kV/cm to 19.75 kV/cm.

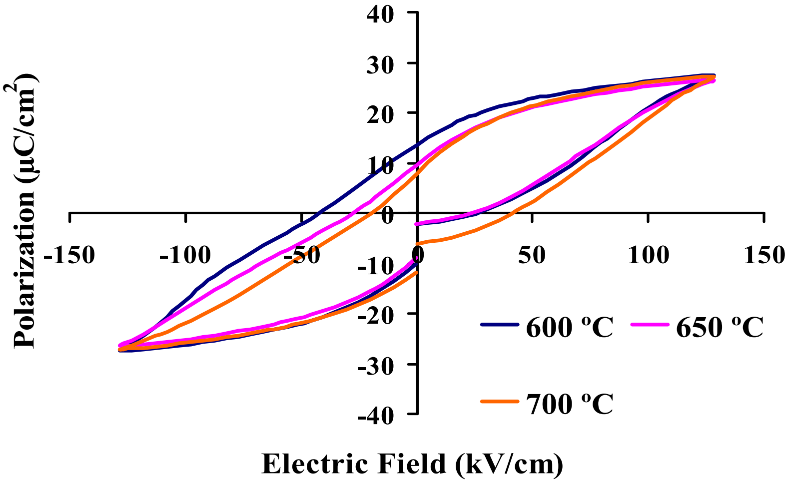

Figure 4.58 Hysteresis curves of PNZT thin films with a composition $Pb_{0.985}(Zr_{0.53}Ti_{0.47})_{0.97}Nb_{0.03}O_3$ and sintered at 600, 650 and 700 °C for 1 h.

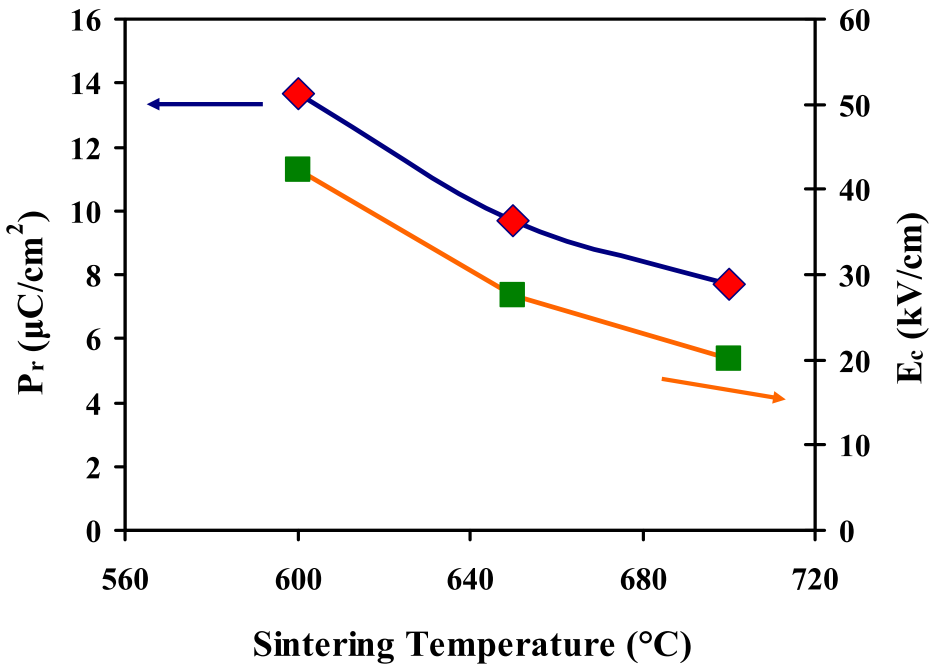

Figure 4.59 Change of remnant polarization (P_r) and coercive field (E_c) values with respect to sintering temperature for PNZT thin films with a composition $Pb_{0.985}(Zr_{0.53}Ti_{0.47})_{0.97}Nb_{0.03}O_3$ that were 390 nm in thickness and sintered for 1 h.

Figure 4.60 shows the hysteresis curves for films sintered at different sintering periods at 600 °C. It can be seen in Figure 4.61 that the remnant polarization and coercive field values were highest in the films sintered for 1 h. Longer sintering periods cause a decrease in the ferroelectric properties. There was a slight increase observed in remnant polarization value for the films sintered for 3 h, but this value is still lower than the films sintered for 1 h. This increase can be explained by the pure perovskite phase obtained for films sintered at 600 °C for 3 h given in Figure 4.9. P_r value was decreasing from 13.67 µC/cm^2 to 7.41 µC/cm^2 as the sintering period was increased. Coercive field values were also decreased from 42.21 kV/cm to 20.39 kV/cm. Figures 4.62 and 4.63 show the hysteresis curves for films sintered at 650 and 700 °C, respectively for 1, 2 and 3 h.

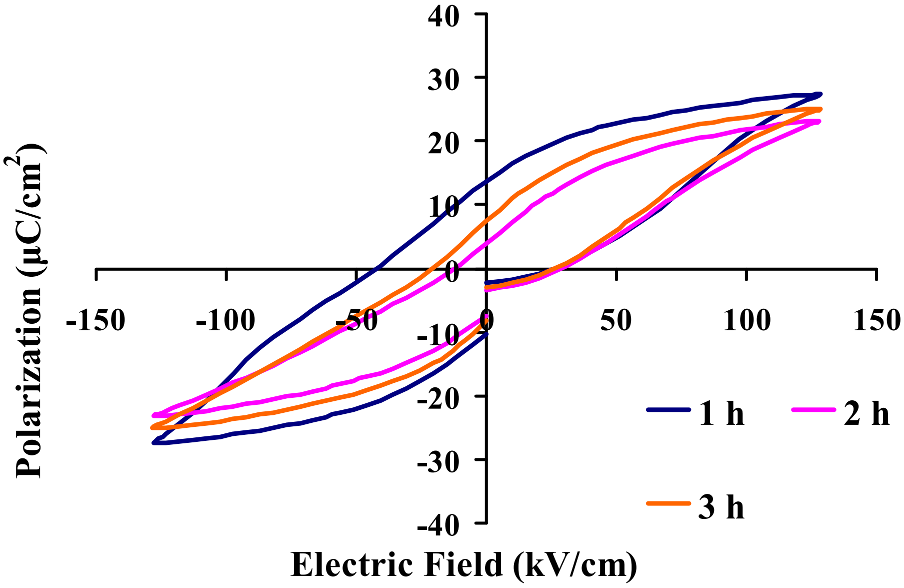

Figure 4.60 Hysteresis curves of PNZT thin films with a composition $Pb_{0.985}(Zr_{0.53}Ti_{0.47})_{0.97}Nb_{0.03}O_3$ and sintered at 600 °C for 1, 2 and 3 h.

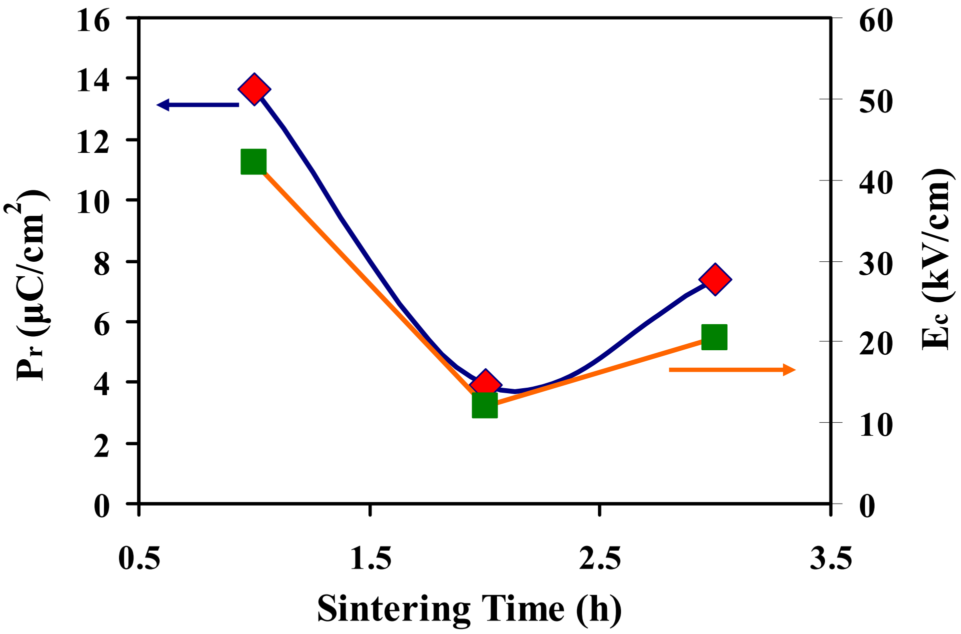

Figure 4.61 Change of remnant polarization (P_r) and coercive field (E_c) values with respect to sintering period for PNZT films of composition $Pb_{0.985}(Zr_{0.53}$ $Ti_{0.47})_{0.97}Nb_{0.03}O_3$ that have 390 nm thickness and sintered at 600 °C.

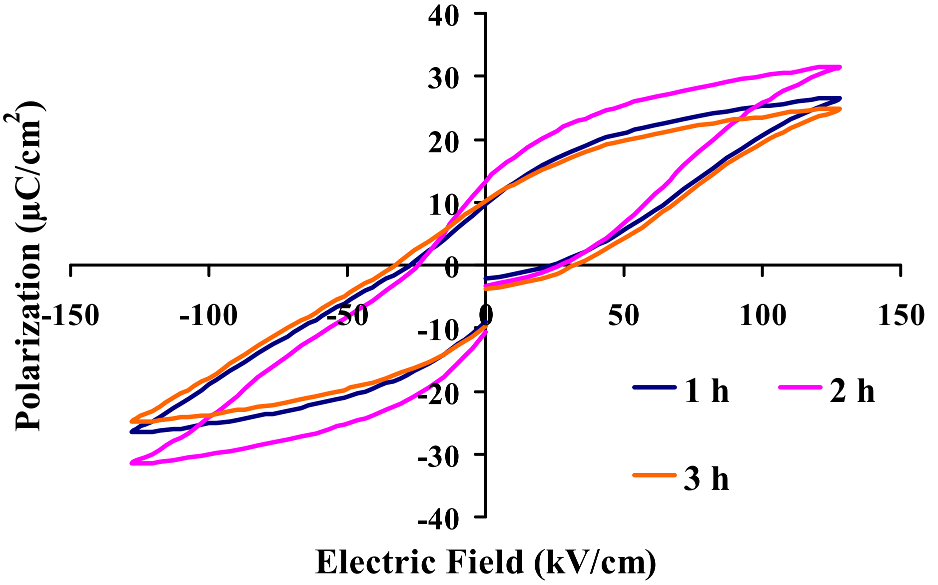

Figure 4.62 Hysteresis curves of PNZT thin films with a composition $Pb_{0.985}(Zr_{0.53}Ti_{0.47})_{0.97}Nb_{0.03}O_3$ and sintered at 650 °C for 1, 2 and 3 h.

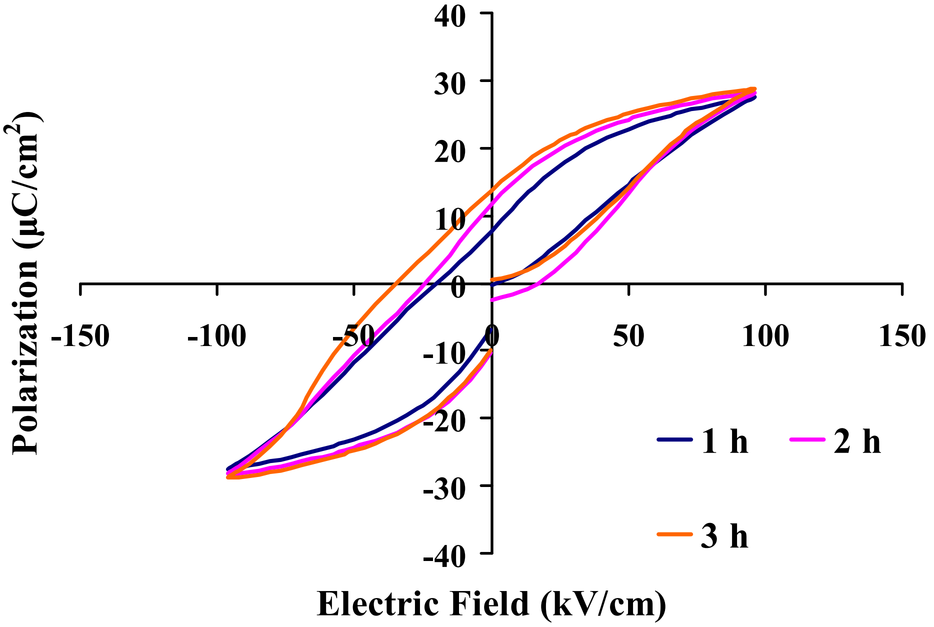

Figure 4.63 Hysteresis curves of PNZT thin films with a composition $Pb_{0.985}(Zr_{0.53}Ti_{0.47})_{0.97}Nb_{0.03}O_3$ and sintered at 700 °C for 1, 2 and 3 h.

Ferroelectric properties of the films with different compositions were measured after the determination of optimum sintering parameters of PNZT thin films using the results given in Table 4.5 as 600 °C for 1 h. Figure 4.64 shows the hysteresis curves for PNZT films sintered at 600 °C for 1 h and had a thickness of 390 nm. All of the parameters except Nb content were kept constant in order to analyze the effect of Nb addition on PZT films. Electric field value of 128.2 kV/cm (Applied Voltage: 5 V) was applied to all of the films and similar shaped hysteresis curves were obtained. Remnant polarization and coercive field values were changing at different Nb doping levels.

Figures 4.65 and 4.66 show the change of remnant polarization and coercive field values with respect to Nb content, respectively. For the undoped PZT thin films, P_r and E_c values were found as 16.3 $\mu C/cm^2$ and 26.22 kV/cm, respectively. P_r increased to 20.6 $\mu C/cm^2$ for 1 at % Nb doped PNZT films. Higher doping levels of more than 1 at % Nb decreases ferroelectric properties. It is observed that after 3 at % doping, the remnant polarization values are far below the undoped PZT thin films. This decrease can be explained by the decrease in grain size of the films. Also, a fraction of the domains were pinned and failed to switch under the weakened applied field, which also lead to a decrease of remnant polarization [44]. Coercive field values are very close for the undoped and 1 at % doped PZT thin films. E_c value is increasing between 1 and 3 at % Nb doped film. There is no explanation about this large increase in the literature. Kurchania and Milne [4] observed that as the Nb content increased the coercive field had also increased, but the increase was very small as compared to our results. Most of the studies found that Nb doping decreases coercive field [5, 6, 22]. Some of them stated that there is no effect of Nb doping on the coercive field [39, 45]. These contradictory results show that, influence of Nb addition on coercive field has not well understood yet. After 3 at % Nb doping, coercive field decreased to 6.37 kV/cm and it increases back to 20.43 kV/cm for 7 at % Nb doped films. The optimum Nb doping level was determined as 1 at % and the same results were also achieved by Klissurska et al [39].

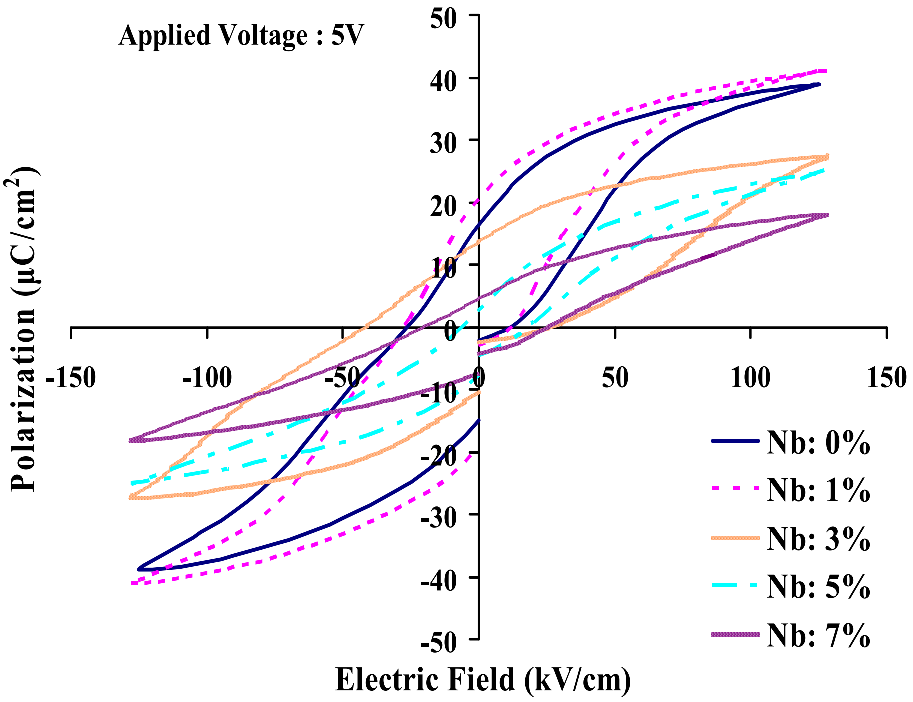

Figure 4.64 Change of hysteresis behavior with varying Nb content for PNZT thin films sintered at 600 °C for 1 h with a thickness of 390 nm.

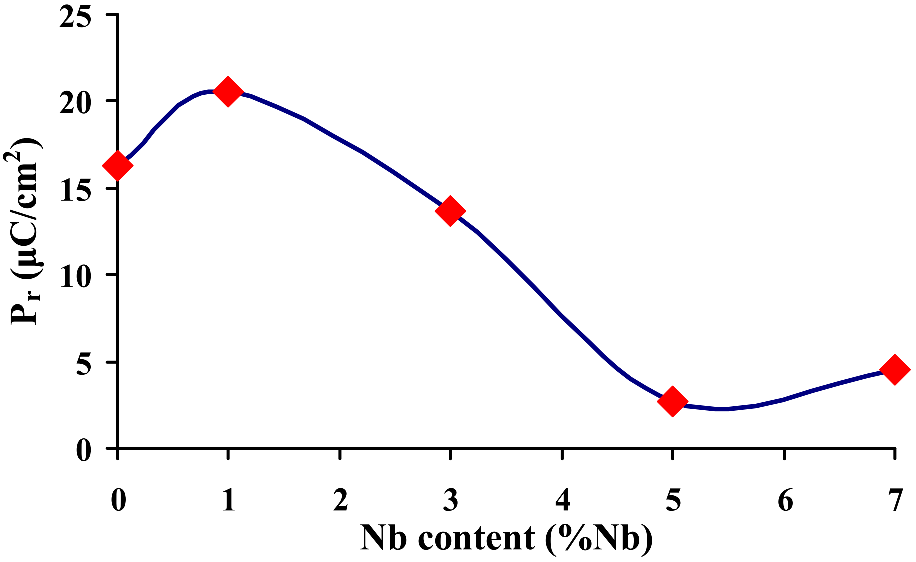

Figure 4.65 Change of remnant polarization (P_r) with respect to Nb content for the films sintered at 600 °C for 1 h.

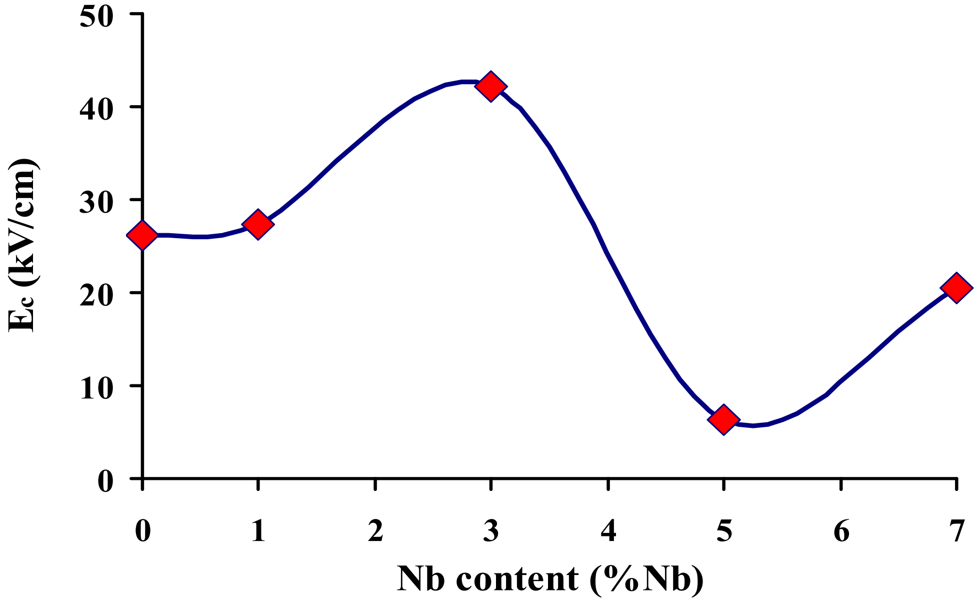

Figure 4.66 Change of coercive field (E_c) with respect to Nb content for the films sintered at 600 °C for 1 h.

Figure 4.67 shows the hysteresis loops for $Pb_{0.995}(Zr_{0.53}Ti_{0.47})_{0.99}Nb_{0.01}O_3$ thin film sintered at 600 °C for 1 h at different applied voltages. The voltage applied to the films was increased from 5 V to 10 and 15 V, so that the maximum polarizations can be achieved. The films break at voltages higher than 15 V because of the small thicknesses used in the study. For 10 and 15 V, the remnant polarizations were determined as 33.38 and 35.75 μC/cm^2, respectively. These results are consistent with the previous studies and the present values are higher than most of the studies [6, 33, 46]. Coercive field values increased to 51.33 and 76.65 kV/cm at voltages of 10 and 15 V, respectively as expected.

Figures 4.67 to 4.71 show the hysteresis loops of PNZT thin films having different compositions.

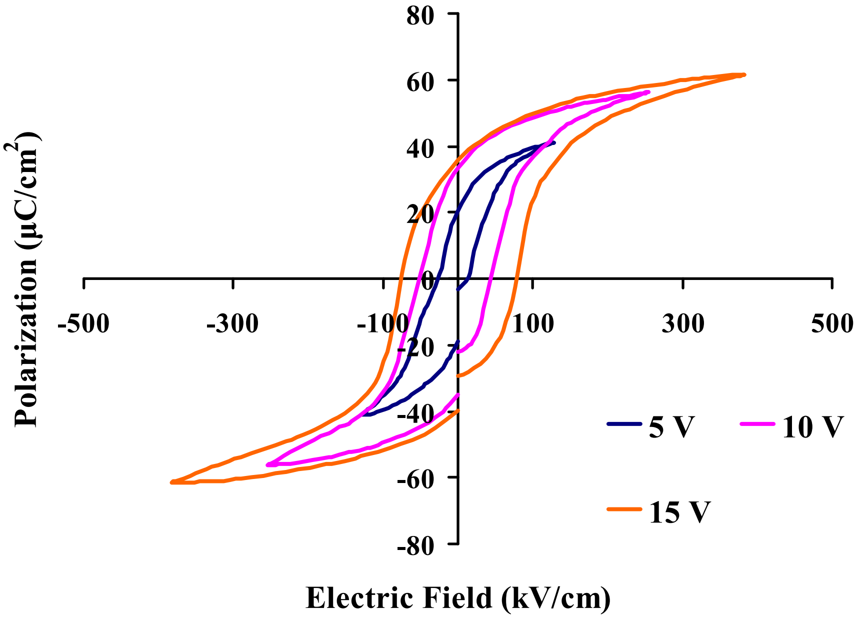

Figure 4.67 Ferroelectric hysteresis behavior of PNZT $Pb_{0.995}(Zr_{0.53}Ti_{0.47})_{0.99}Nb_{0.01}O_3$ thin films sintered at 600 °C for 1 h and had a thickness of 390 nm at different applied voltages.

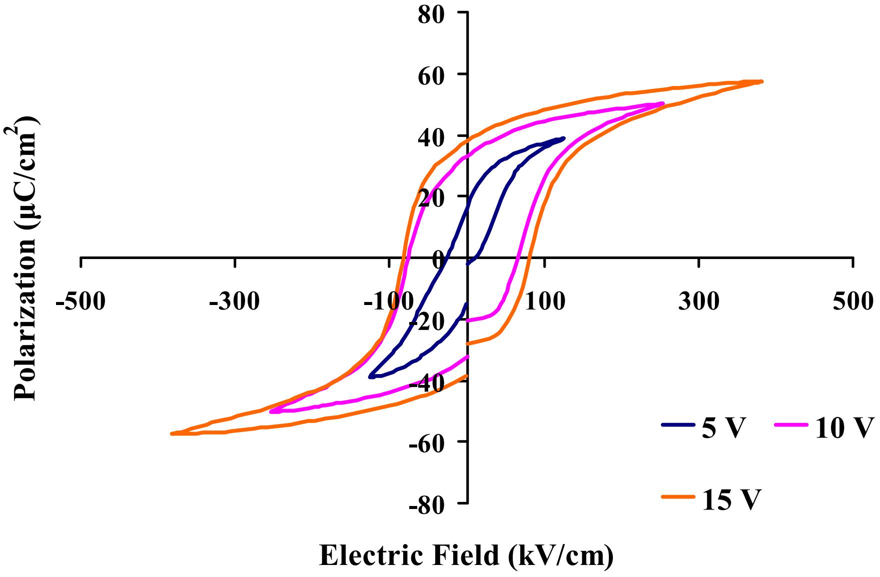

Figure 4.68 Ferroelectric hysteresis behavior of PNZT $Pb(Zr_{0.53}Ti_{0.47})O_3$ thin films sintered at 600 °C for 1 h and had a thickness of 390 nm at different applied voltages.

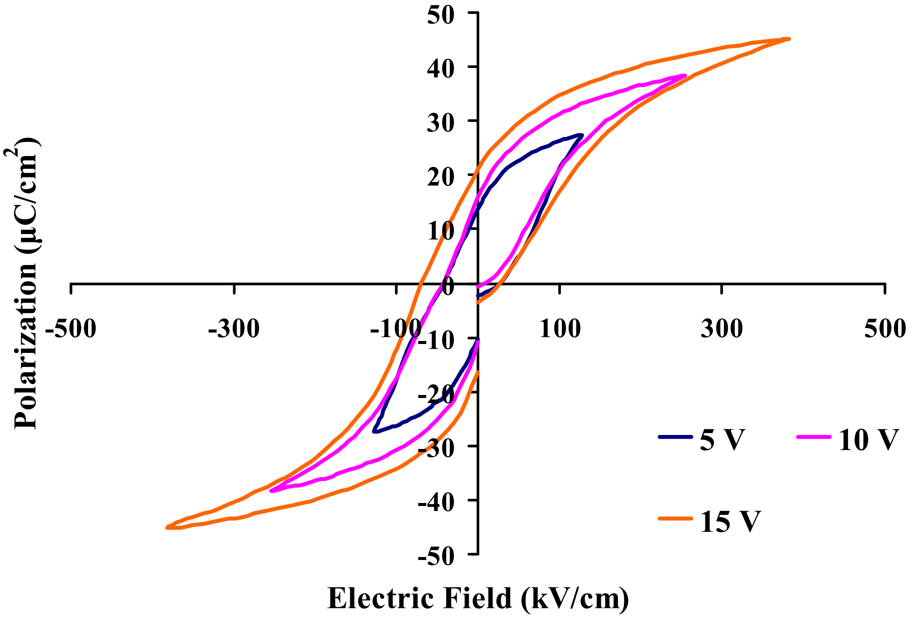

Figure 4.69 Ferroelectric hysteresis behavior of PNZT $Pb_{0.985}(Zr_{0.53}Ti_{0.47})_{0.97}Nb_{0.03}O_3$ thin films sintered at 600 °C for 1 h and had a thickness of 390 nm at different applied voltages.

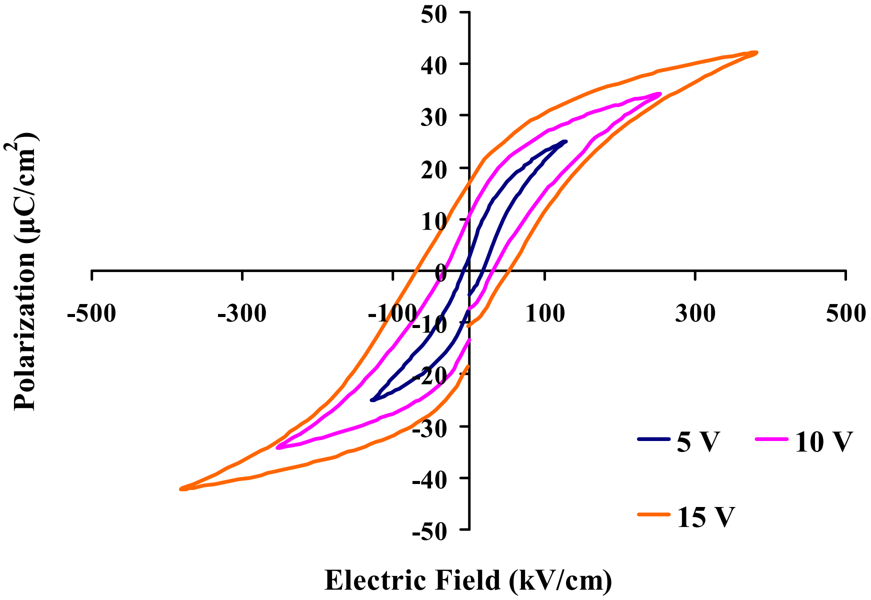

Figure 4.70 Ferroelectric hysteresis behavior of PNZT $Pb_{0.975}(Zr_{0.53}Ti_{0.47})_{0.95}Nb_{0.05}O_3$ thin films sintered at 600 °C for 1 h and had a thickness of 390 nm at different applied voltages.

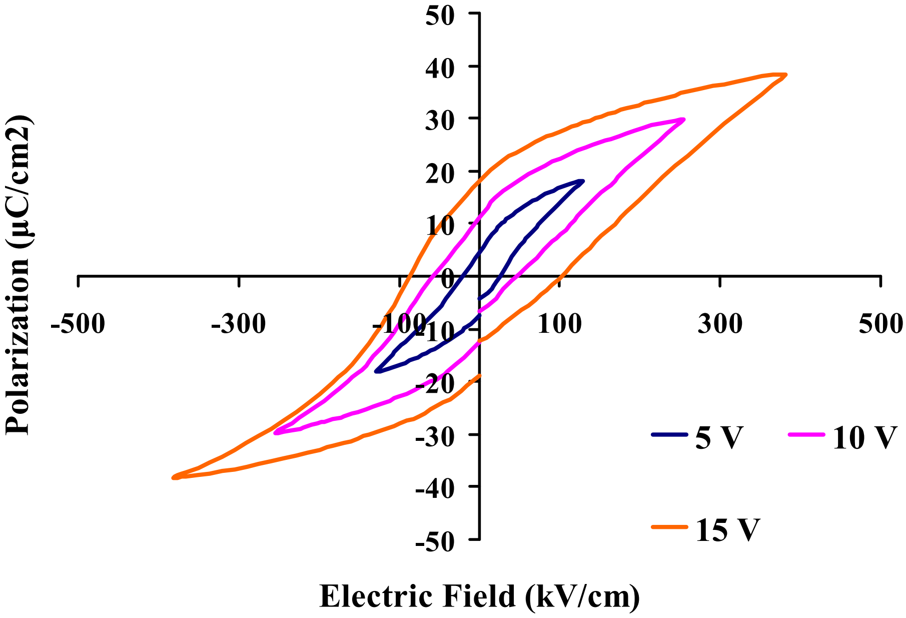

Figure 4.71 Ferroelectric hysteresis behavior of PNZT $Pb_{0.965}(Zr_{0.53}Ti_{0.47})_{0.93}Nb_{0.07}O_3$ thin films sintered at 600 °C for 1 h and had a thickness of 390 nm at different applied voltages.

4.8 Leakage Current Analysis of PNZT Thin Films

Figure 4.72 shows the influence of Nb doping on the current density with respect to electric field (J-E) at ±10 V. The leakage current densities of PNZT thin films were compared at 36.63 kV/cm. From Figure 4.73 it can be seen that, for the undoped PZT film, leakage current density is $1.1310^{-6}\times$ A/cm^2. As the Nb content increases, current density decreases and reaches to 4.38×10^{-7} A/cm^2 for the 7 at % Nb doped film. Similar results were obtained by other studies [4, 6, 33]. This decrease can be explained by the addition of a higher valence Nb^{5+} cation to the perovskite matrix. By this way, excess oxygen vacancies are created and compensated by combining free electrons. The increase of barrier height to thermonic emissions of electrons from the Pt electrode makes it difficult for electrons to transfer from Pt electrode into PNZT film because of the decreased electron concentration [47].

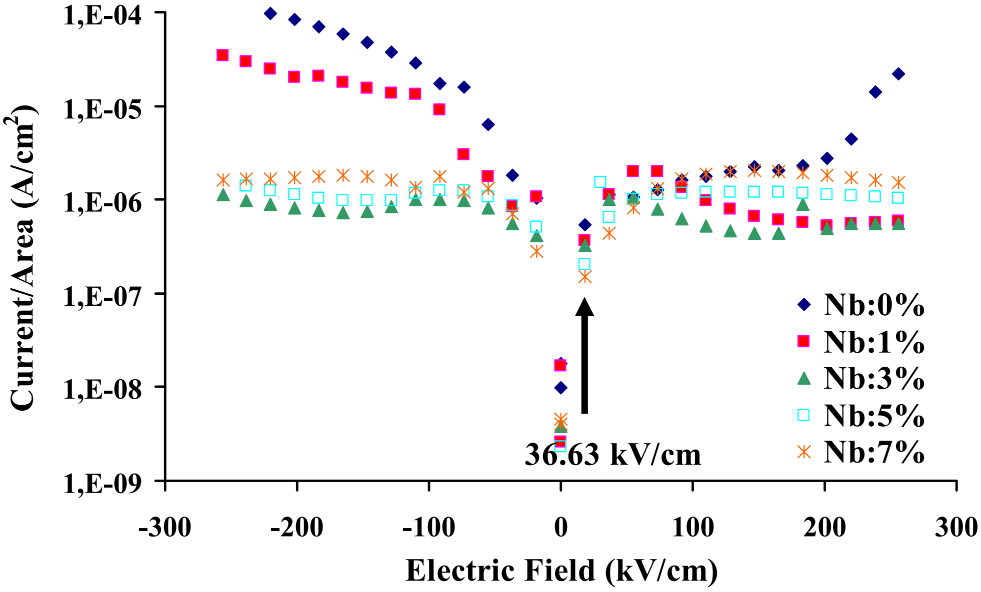

Figure 4.72 Leakage current analysis (J-E) for PNZT thin films with varying Nb content while other parameters were held constant.

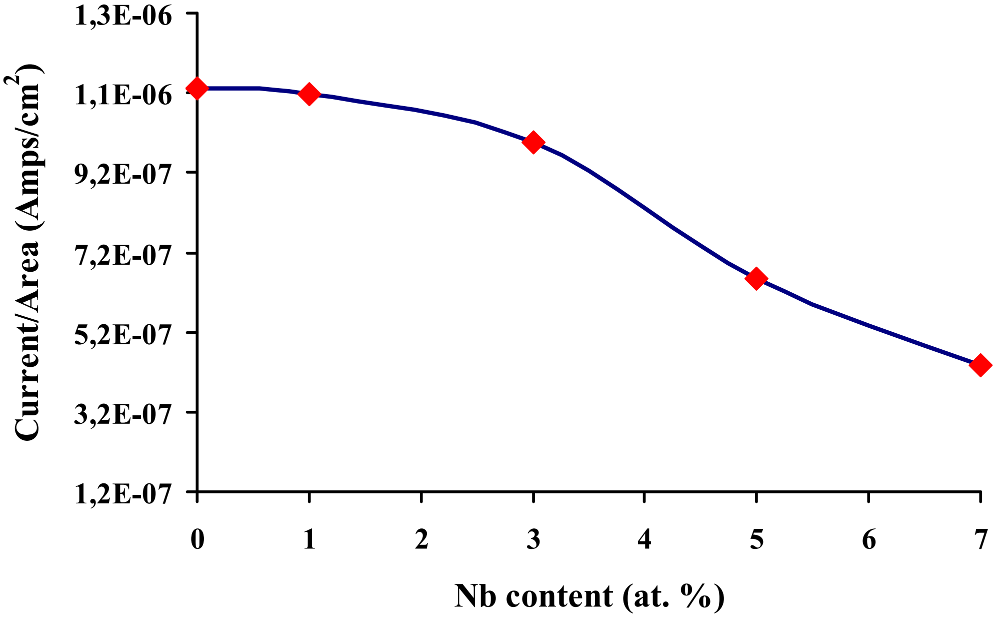

Figure 4.73 Leakage current density values of PNZT thin films at 36.63 kV/cm with changing Nb content while other parameters were held constant.

CHAPTER 5

CONCLUSION AND FURTHER SUGGESTIONS

The effect of Nb doping on PZT [Zr/Ti : 53/47] thin films have been examined in this study. PZT and PNZT thin films were prepared by sol-gel method. Different parameters like sintering temperature, sintering time, Nb content and film thickness were selected to find the optimum properties of films. Comparison of PNZT thin films were done by investigating the structural and electrical properties of the films.

PNZT thin films that are smooth and crack-free were grown on (111)-Pt/Ti/SiO_2/Si-(100) substrates by a spin coating process. In spin coating process, substrates were coated with PNZT solutions with 1500 rpm spinning speed for 30 seconds. By using multiple drying-pyrolysis cycles, films with different thicknesses produced. Optimum film thickness was achieved as 390 nm (double layered films). Single layered films had a thickness of 250 nm. Three and four layered films were 520 and 870 nm in thickness, respectively.

To obtain a homogeneous solution with the desired composition, two different solutions were prepared and then mixed with each other. The concentration and the volume of the solutions were set to 0.4M and 40 ml. They can be kept as a stock solution for a few months and 2-methoxyethanol was used as solvent for all of the compositions. Viscosity did not change significantly as the shear rate increased which showed the uniformity of the solution.

PNZT thin films having the composition $Pb_{0.985}(Zr_{0.53}Ti_{0.47})_{0.97}Nb_{0.03}O_3$ and thickness of 390 nm were used to estimate the optimum sintering parameters. In films sintered at temperatures higher than 600 °C, Ti_2O_3 phase was observed. X-ray diffraction studies showed optimum sintering temperature and sintering period as 600 °C and 1 h, since pure perovskite phase was obtained using these conditions.

PNZT thin films with changing Nb content were produced in order to observe the effects of Nb^{+5} ion additions on PZT thin films. While doing that, sintering temperature, sintering time and film thickness were kept constant. Ti_2O_3 phase was detected for the films containing 0 and 7 at % Nb. There was only perovskite peaks emerged for other compositions. As the Nb content increased, the peak intensities of the perovskite phase was decreased influencing electrical properties in a negative manner.

SEM, AFM and surface profilometry was used to study the surface and cross-sections of PNZT thin films. The results showed that the films were smooth and crack-free. Grain sizes of films were determined using FESEM micrographs. Grain size decreases with increasing Nb content except for 1 at % Nb doped films, because Nb inhibits growth of grains. For 1 at % Nb doped PNZT thin films; maximum grain size of 130 nm was obtained.

Dielectric properties of PNZT thin films were determined using two parameters which were dielectric constant (ε_r) and tangent loss ($\tan\delta$). The dielectric and tangent loss measurements were done at frequencies between 1 kHz-500 kHz. Films are usable in this range since dielectric properties were almost constant. Dielectric measurements showed that, maximum dielectric constant was achieved for 1 at % Nb doped films as 689. It was decreased as the Nb content was further increased. Tangent loss values were found between 2-4% and independent of Nb concentrations. Dielectric constant increases with increasing thickness except for 3-layered (520 nm) PNZT thin film. The maximum value was achieved for 4 layered films (870 nm) as 1275.

C-V curves of PNZT thin films showed similar behavior, where capacitance decreased with increasing bias voltage. Ferroelectric behavior of the films was determined from the butterfly shaped C-V curves.

Ferroelectric properties of PNZT thin films were determined using hysteresis curves. Remnant polarization (P_r) and coercive field (E_c) values of the films were obtained. The highest remnant polarization value was found as 13.67 μC/cm^2 for PNZT thin films sintered at 600 °C for 1 h, keeping the thickness (390 nm) and Nb content (3 at %) constant. XRD studies also supported this result since pure perovskite phase was determined for those films. E_C of 42.21 kV/cm was obtained for the films sintered at 600 °C for 1 h.

Ferroelectric properties of films with different compositions were measured. P_r and E_c values were found as 16.30 μC/cm^2 and 26.22 kV/cm, respectively for the undoped PZT thin films. P_r increased to 20.60 μC/cm^2 for 1 at % Nb doped PNZT films. Higher doping levels of more than 1 at % Nb decreases ferroelectric properties. Maximum remnant polarization was found as 35.70 μC/cm^2 for 1 at % Nb doped films using 15 V (382 kV/cm) applied voltage. Coercive field values changed with Nb content.

Leakage current analysis of PNZT thin films showed a decrease in leakage current density upon increase in Nb content. For the undoped PZT film, it is 1.13×10^{-6} A/cm^2. As the Nb content increases, current density decreases and reaches to 4.38×10^{-7} A/cm^2 for the 7 at % Nb doped film.

The decrease of the electrical properties of PNZT thin films is due to decrease of grain size of films as the Nb content increases. Another factor is the distortion in the crystal structure and pinning of the domains by the increase of defects and vacancies. As the amount of Nb^{5+} ion in the crystal structure had increased, the properties were affected negatively.

To achieve better dielectric and ferroelectric properties, clean room conditions should be obtained. The room temperature should stay constant and glove box should be used for the preparation of solutions. Niobium (V) ethoxide reacts with air rapidly so that the intended amount of Nb additions was difficult to achieve in air atmosphere. Rapid thermal sintering (RTA) could be effective in order to get better results because it reduces the interfacial layer formed between the film and substrate.

REFERENCES

1. A. S. Bhalla and K. M. Nair, Ceramic Transactions Ferroelectric Films. Westerville, Ohio : The American Ceramic Society, 1992, 25.

2. K. Tu, J. W. Mayer and L. C. Feldman, Electronic Thin Film Science for Electrical Engineers and Material Scientists. New York : Macmillan ; Toronto : Maxwell Macmillan Canada ; New York : Maxwell Macmillan International, 1992.

3. R. C. Buchanan, Ceramic Materials for Electronics. New York :Marcel Dekker, 2004.

4. R. Kurchania and S. J. Milne, Effect of Niobium Modifications to PZT (53/47) Thin Films Made by a Sol-Gel Route. Journal of Sol-Gel Science and Technology, 2003, 28, p. 143-150.

5. D. F. Ryder and N. K. Raman, Sol-Gel Processing of Nb-Doped $Pb(Zr,Ti)O_3$ Thin Films for Ferroelectric Memory Applications. Journal of Electronic Materials, 1992, 21(10), p. 971-975.

6. E. C. F. Souza, A. Z. Simoes, M. Cilense, E. Longo and J. A. Varela, The Effect of Nb Doping on Ferroelectric Properties of PZT Thin Films Prepared From Polymeric Precursors. Materials Chemistry and Physics, 2004, 88, p. 155-159.

7. R. D. Klissurska, K. G. Brooks, I. M. Reaney, C. Pawlaczyk, M. Kosec and N. Setter, Effect of Nb Doping on the Microstructure of Sol-Gel-Derived PZT Thin Films. Journal of American Ceramic Society, 1995, 78(6), p. 1513-1520.

8. C. Nistorica, J. Zhang, P. Padmini, S. Kotru and R. K. Padney, Integrated PNZT Structures for MEMS Gyroscope. Integrated Ferroelectrics, 2004, 63, p. 49-54.

9. K. W. Kwok, K. P. Kwok, R. C. W. Tsang, H. L. W. Chan and C. L. Choy, Preparation and Piezoelectric Properties of Sol-Gel-Derived Nb-Doped PZT Films for MEMS Applications. Integrated Ferroelectrics, 2006, 80, p. 155-162.

10. W. S. Kim, S. M. Ha, H. H. Park and C. E. Kim, The Effects of Cation-Substitution on the Ferroelectric Properties of Sol-Gel Derived PZT Thin Film for FRAM Application. Thin Solid Films, 1999, 355-356, p. 531-535.

11. W. D. Callister, J., Materials Science and Engineering An Introduction. New York: Wiley, 2000, 5th edition.

12. D. Damjanovic, Ferroelectric, Dielectric and Piezoelectric Properties of Ferroelectric Thin Films and Ceramics. Rep. Prog. Phys., 1998, 61, p. 1267-1324.

13. B. Kaplan, Preparation of PNZT Thin Films by Chemical Solution Deposition and Their Characterization. M.S. Thesis (Supervisor: Prof. Dr. Macit Özenbaş), Middle East Technical University, Ankara-Turkey, 2005.

14. C. P. Smyth, Dielectric Behavior and Structure; Dielectric Constant and Loss, Dipole Moment and Molecular Structure. New York, McGraw-Hill, 1955.

15. Laserworld Swedish Laser Medical Society, http://www.laser.nu/lllt/lllt_editorial13.htm, January 2008.

16. A. R. V. Hippel, Dielectric Materials and Applications; Papers by Twenty-Two Contributors. [Cambridge] Published Jointly by the Technology Press of M.I.T. and Wiley, New York, 1954.

17. Optoelectronic Devices Laboratory Department of Physics, http://physics.cusat.ac.in/oed/research_area.htm, January 2008.

18. PC in control, http://www.pc-control.co.uk/piezoelectric_effect.htm, January 2008.

19. P. K. Larsen, R. Cuppens and G. A. C. M. Spierings, Ferroelectric Memories. Ferroelectrics, 1992, 128, p. 265-292.

20. J. F. Scott and C. Araujo, Ferroelectric Memories. Science, 1989, 246, p. 1400-1405.

21. D. Remiens, E. Cattan, C. Soyer and T. Haccart, Piezoelectric Properties of Sputtered PZT Films: Influence of Structure, Microstructure, Film Thickness (Zr,Ti) Ratio and Nb Substitution. Materials Science in Semiconductor Processing, 2003, 5, p. 123-127.

22. T. Haccart, D. Remiens and E. Cattan, Substitution of Nb Doping on the Structural, Microstructural and Electrical Properties in PZT Films. Thin Solid Films, 2003, 423, p. 235-242.

23. Enhancing Science Learning Through Electronic Library, http://resources.edb.gov.hk/physics/articleIE/smartmaterials/SmartMaterials_e.htm, January 2008.

24. PI, http://www.physikinstrumente.com/en/products/prorder.php?sortnr=400600.30, January 2008.

25. C. A. Guarany, E. B. Araujo, P. R. J. Silva and H. Saitovitch, Hyperfine Interaction Measurements on Ceramics: PZT Revisited. Physica B, 2007, 389, p. 130-134.

26. A. Bouzid, E. M. Bourim, M. Gabbay and G. Fantozzi, PZT Phase Diagram Determination by Measurement of Elastic Moduli. Journal of the European Ceramic Society, 2005, 25, p. 3213-3221.

27. B. Lee and S. Komarneni, Chemical Processing of Ceramics. Boca Raton : Taylor & Francis, 2005.

28. A. C. Pierre, Introduction to Sol-Gel Processing. Boston : Kluwer Academic Publishers, 1998.

29. C. P. D. Araujo, J. F. Scott and G.W. Taylor, Ferroelectric Thin Films: Synthesis and Basic Properties. Amsterdam : Gordon and Breach, 1996.

30. Nemo, http://optoweb.fis.uniroma2.it/opto/solgel/index.html, January 2008.

31. H. Han, X. Song, J. Zhong, S. Kotru, P. Padmini and R. K. Pandey, Highly a-axis-oriented Nb-Doped $Pb(Ti_xZr_{1-x})O_3$ Thin Films Grown by Sol-Gel Technique for Uncooled Infrared Dectors. Applied Physics Letters, 2004, 85(2), p. 5310-5312.

32. B. A. Tuttle, D. H. Doughty and S. L. Martinez, Microstructure of Solution-Processed Lead Zirconate Titanate (PZT) Thin Films. Journal of American Ceramic Society, 1991, 74(6), p. 1455-1458.

33. D. Dimos, R. W. Schwartz and S. J. Lockwood, Control of Leakage Resistance in $Pb(Zr,Ti)O_3$ Thin Films by Donor Doping. Journal of American Ceramic Society, 1994, 77(11), p. 3000-3005.

34. T. Haccart, E. Cattan, D. Remiens S. Hiboux and P. Muralt, Evaluation of Niobium Effects on the Longitudinal Piezoelectric Coefficients of $Pb(Zr,Ti)O_3$ Thin Films. Applied Physics Letters, 2000, 76(22), p. 3292-3294.

35. D. E. Bornside, C. W. Macosco and L. E. Scriven, Journal of Imaging Technology, 1987, 13, p. 122-129.

36. E. İzgi, Characterization of Superconducting Bi-Sr-Ca-Cu-O System Prepared by Sol-Gel Processing. M.S. Thesis (Supervisor: Prof. Dr. Macit Özenbaş), Middle East Technical University, Ankara-Turkey, 1996.

37. A. Karakuşçu, Characterization of Maghemite Thin Films Prepared by Sol-Gel Processing. M.S. Thesis (Supervisor: Prof. Dr. Macit Özenbaş), Middle East Technical University, Ankara-Turkey, 2006.

38. Non-Newtonian Flows. http://www.clarkson.edu/subramanian/ch301/notes/nonnewtonian.pdf, January 2008.

39. R. D. Klissurska, A. K. Tagantsev, K. G. Brooks and N. Setter, Use of Ferroelectric Hysteresis Parameters for Evaluation of Niobium Effects in Lead Zirconate Titanate Thin Films. Journal of American Ceramic Society, 1997, 80(2), p. 336-342.

40. N. Tohge, S. Takahashi and T. Minami, Preparation of $PbZrO_3$ –$PbTiO_3$ Ferroelectric Thin Films by the Sol-Gel Process. Journal of American Ceramic Society, 1991, 74(1), p. 67-71.

41. F. G. Mora, D. G. Garcia, M. J. Melendo and A. D. Rodriguez, Experimental Assessment of Plasticity of Nanocrystalline 1.7 mol% Yttria Tetragonal Zirconia Polycrystals. Journal of American Ceramic Society, 2005, 88(6), p. 1529-1535.

42. M. Pereira, A. G. Peixoto and M. J. M. Gomes, Effect of Nb Doping on the Microstructural and Electrical Properties of the PZT Ceramics. Journal of the European Ceramic Society, 2001, 21, p. 1353-1356.

43. M. Nayak, S. Y. Lee and T. Y. Tseng, Electrical and Dielectric Properties of $(Ba_{0.5}Sr_{0.5})TiO_3$ Thin Films Prepared by a Hydroxide-Alkoxide Precursor-Based Sol-Gel Method. Materials Chemistry and Physics, 2002, 77, p. 34-42.

44. D. Liu, C. Wang, H. Zhang, J. Li, L. Zhao and C. Bai, Domain Configuration and Interface Structure Analysis of Sol-Gel-Derived PZT Ferroelectric Thin Films. Surface and Interface Analysis, 2001, 32, p. 27-31.

45. M. Shimizu, H. Fujisawa and T. Shiosaki, Effects of La and Nb Modification on the Electrical Properties of $Pb(Zr,Ti)O_3$ Thin Films by MOCVD. Integrated Ferroelectrics, 1997, 14, p. 69-75.

46. K. W. Kwok, R. C. W. Tsang, H. L. W. Chan and C. L. Choy, Effects of Niobium Doping on the Piezoelectric Properties of Sol-Gel-Derived Lead-Zirconate-Titanate Films. Journal of Applied Physics, 2004, 95(3), p. 1372-1376.

47. S. Y. Wang, B. L. Cheng, C. Wang, S. A. T. Redfern, S. Y. Dai, K. J. Jin, H. B. Lu, Y. L. Zhou, Z. H. Chen and G. Z. Yang, Influence of Ce Doping on Leakage Current in $Ba_{0.5}Sr_{0.5}TiO_3$ Films. Journal of Physics D:Applied Physics, 2005, 38, p. 2253-2257.

APPENDIX

CAPACITANCE-FREQUENCY, DIELECTRIC CONSTANT-FREQUENCY AND FERROELECTRIC HYSTERESIS CURVES

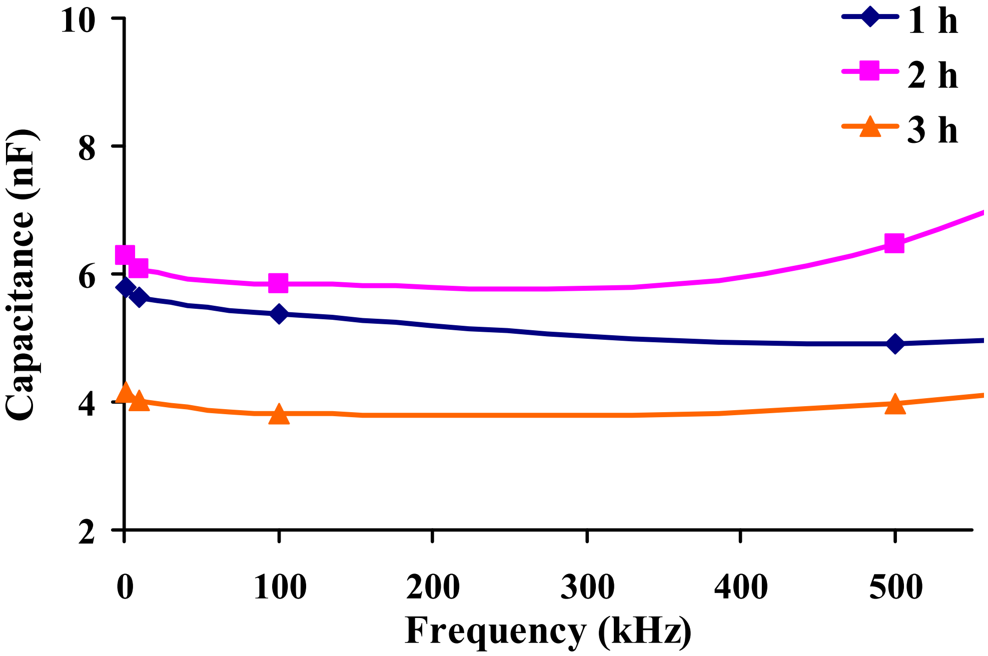

Figure A-1 Capacitance-frequency curves of PNZT [$Pb_{0.985}(Zr_{0.53}Ti_{0.47})_{0.97}Nb_{0.03}O_3$] films sintered for different periods at 650 °C.

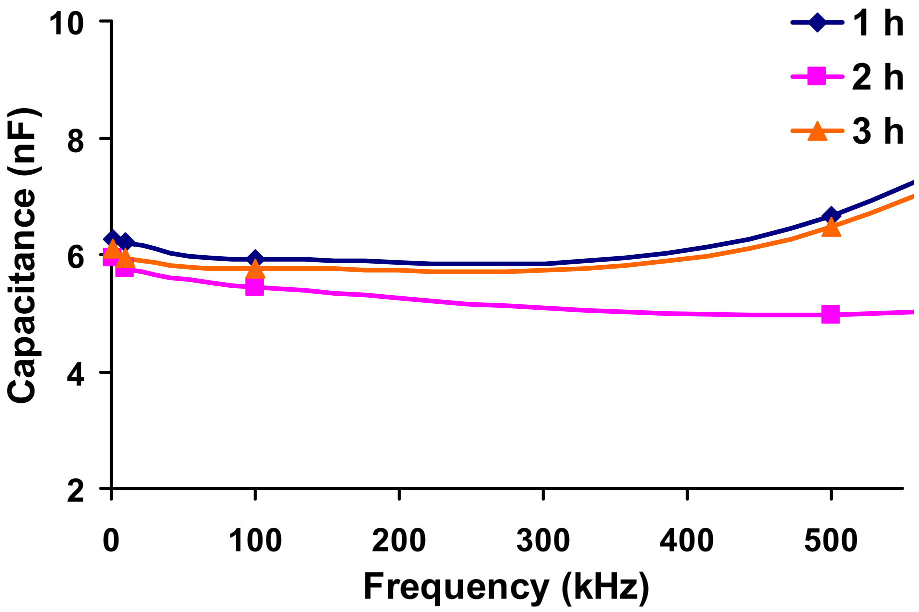

Figure A-2 Capacitance-frequency curves of PNZT [$Pb_{0.985}(Zr_{0.53}Ti_{0.47})_{0.97}Nb_{0.03}O_3$] films sintered for different periods at 700 °C.

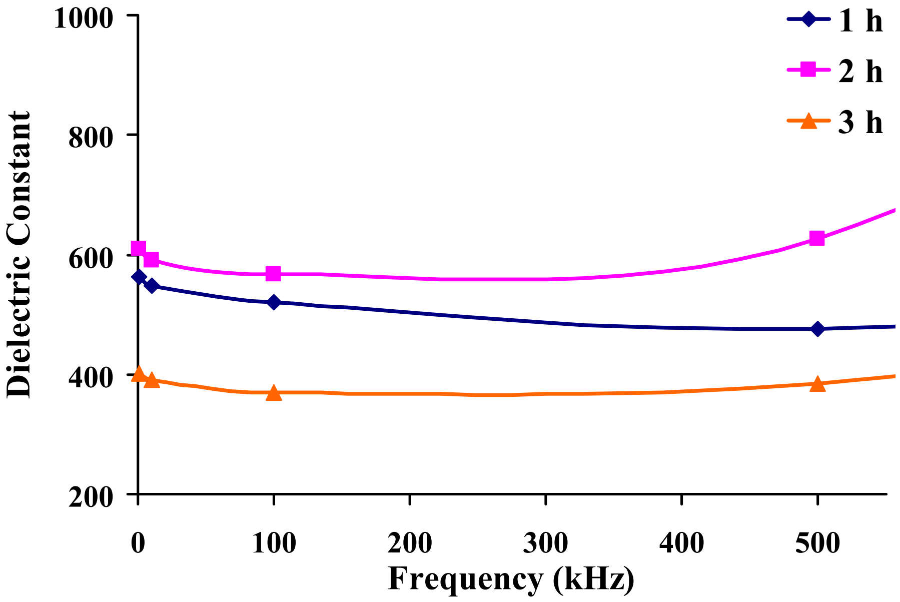

Figure A-3 Dielectric constant-frequency curves of PNZT [$Pb_{0.985}(Zr_{0.53}Ti_{0.47})_{0.97}Nb_{0.03}O_3$] films sintered for different periods at 650 °C.

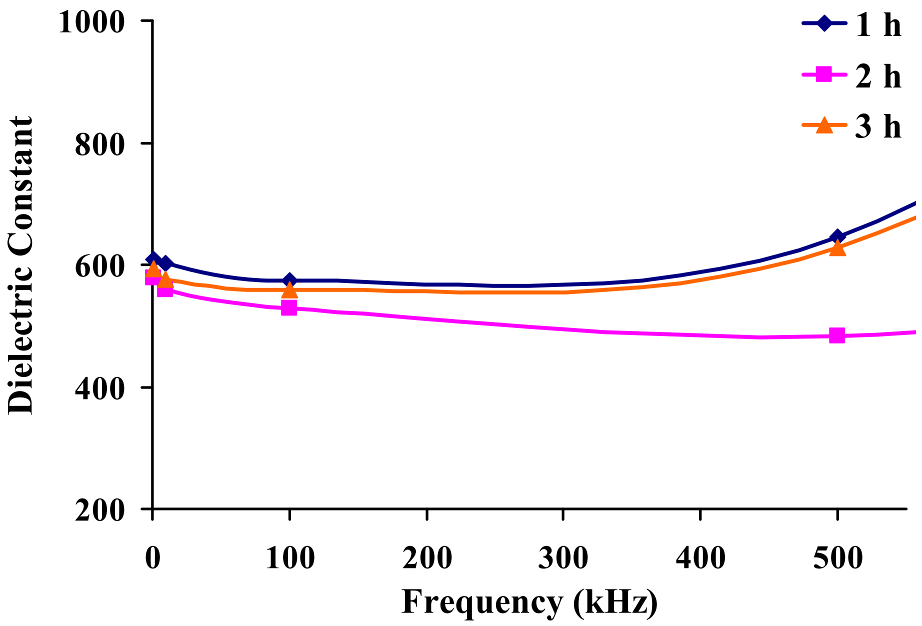

Figure A-4 Dielectric constant-frequency curves of PNZT [$Pb_{0.985}(Zr_{0.53}Ti_{0.47})_{0.97}Nb_{0.03}O_3$] films sintered for different periods at 700 °C.

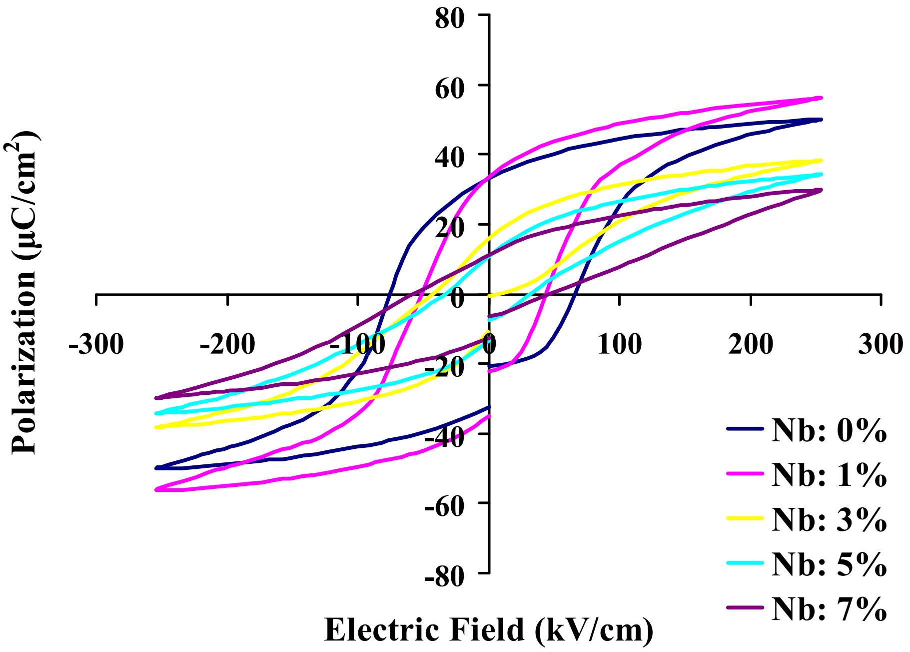

Figure A-5 Change of hysteresis behavior with varying Nb content for PNZT thin films sintered at 600 °C for 1 h with a thickness 390 nm where the applied voltage is 10 V.

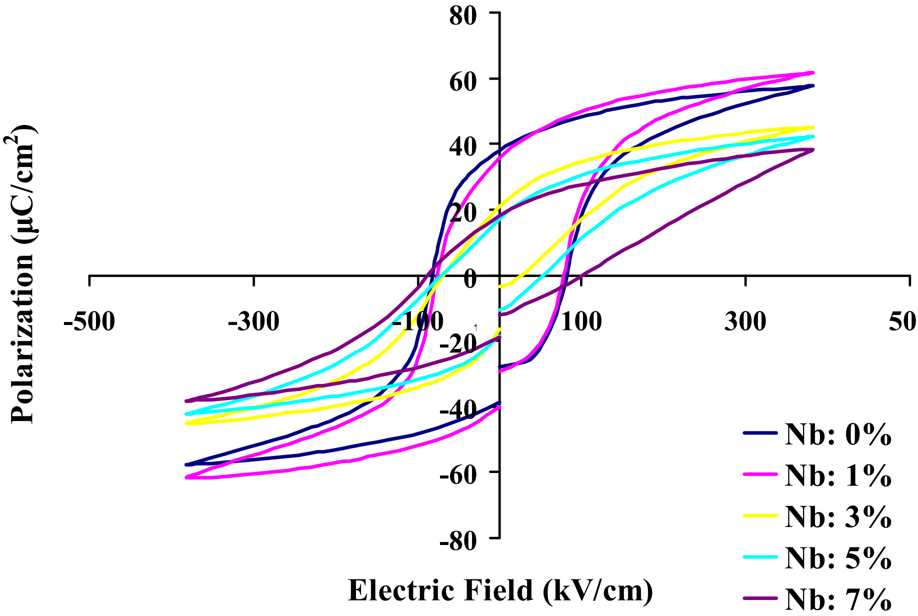

Figure A-6 Change of hysteresis behavior with varying Nb content for PNZT thin films sintered at 600 °C for 1 h with a thickness 390 nm where the applied voltage is 15 V.

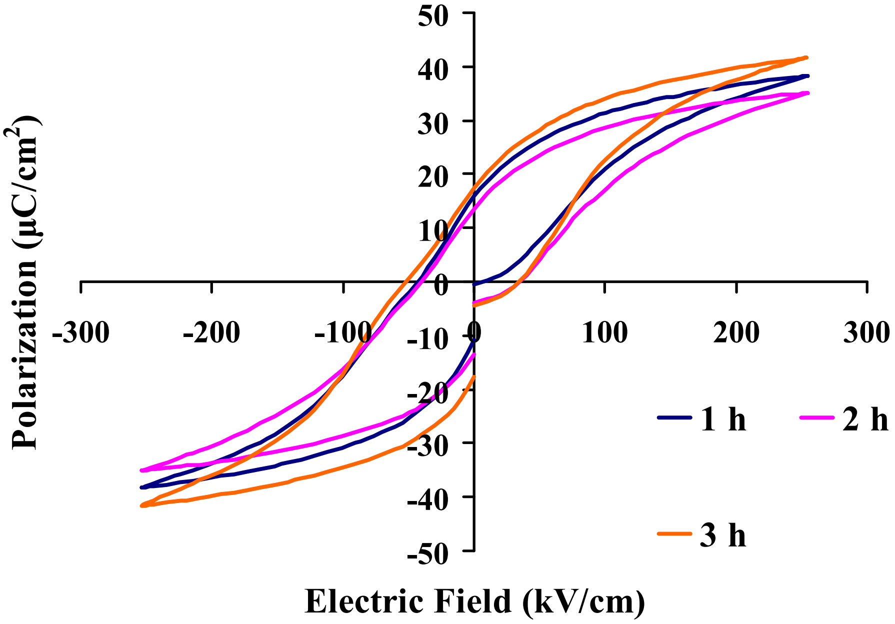

Figure A-7 Hysteresis curves of PNZT thin films with a composition $Pb_{0.985}(Zr_{0.53}Ti_{0.47})_{0.97}Nb_{0.03}O_3$ and sintered at 600 °C for 1, 2 and 3 h at an applied voltage of 10 V.

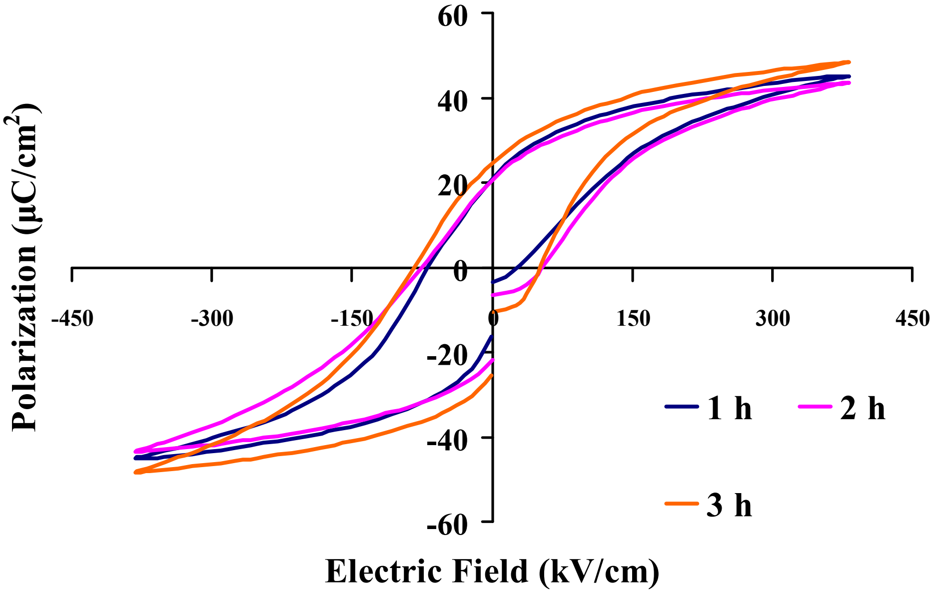

Figure A-8 Hysteresis curves of PNZT thin films with a composition $Pb_{0.985}(Zr_{0.53}Ti_{0.47})_{0.97}Nb_{0.03}O_3$ and sintered at 600 °C for 1, 2 and 3 h at an applied voltage of 15 V.

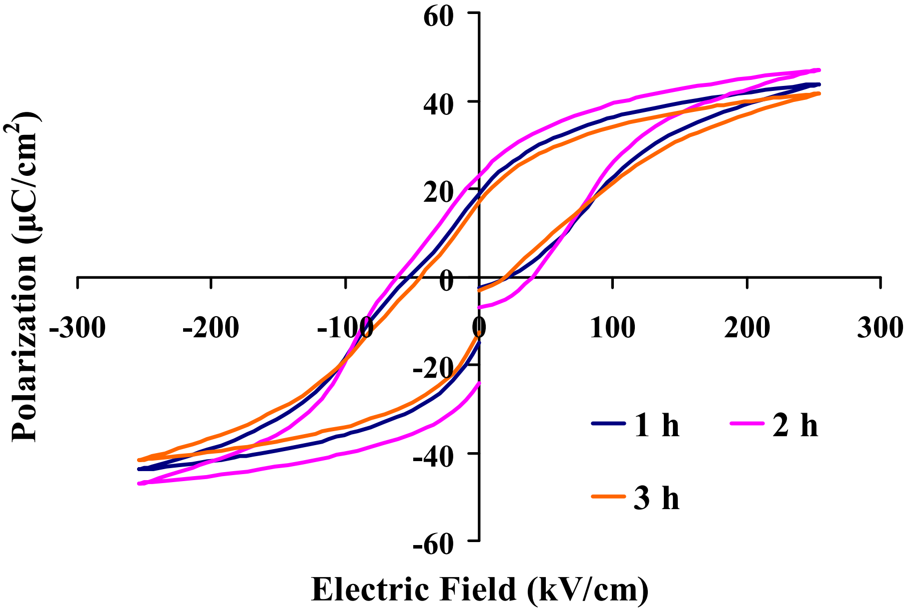

Figure A-9 Hysteresis curves of PNZT thin films with a composition $Pb_{0.985}(Zr_{0.53}Ti_{0.47})_{0.97}Nb_{0.03}O_3$ and sintered at 650 °C for 1, 2 and 3 h at an applied voltage of 10 V.

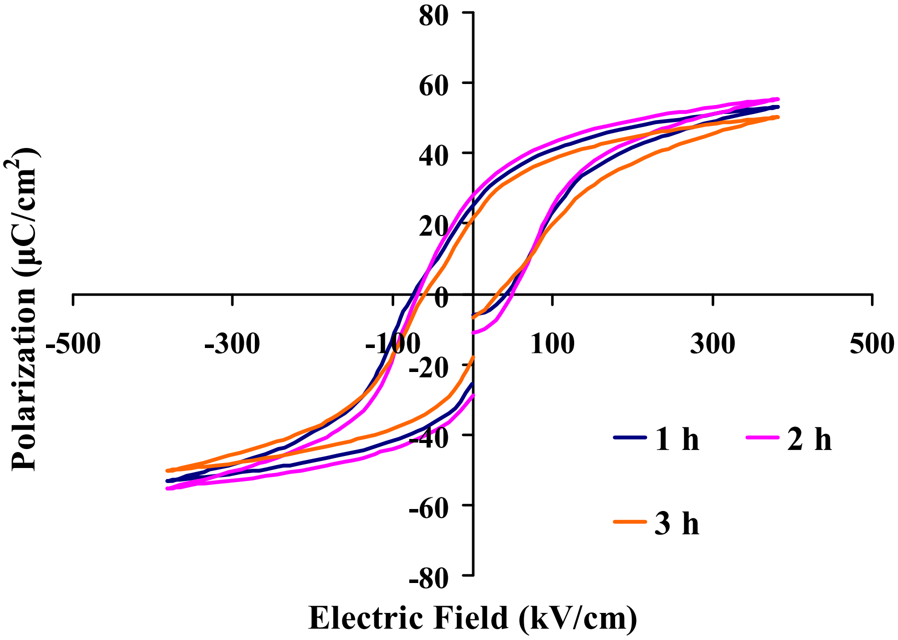

Figure A-10 Hysteresis curves of PNZT thin films with a composition $Pb_{0.985}(Zr_{0.53}Ti_{0.47})_{0.97}Nb_{0.03}O_3$ and sintered at 650 °C for 1, 2 and 3 h at an applied voltage of 15 V.

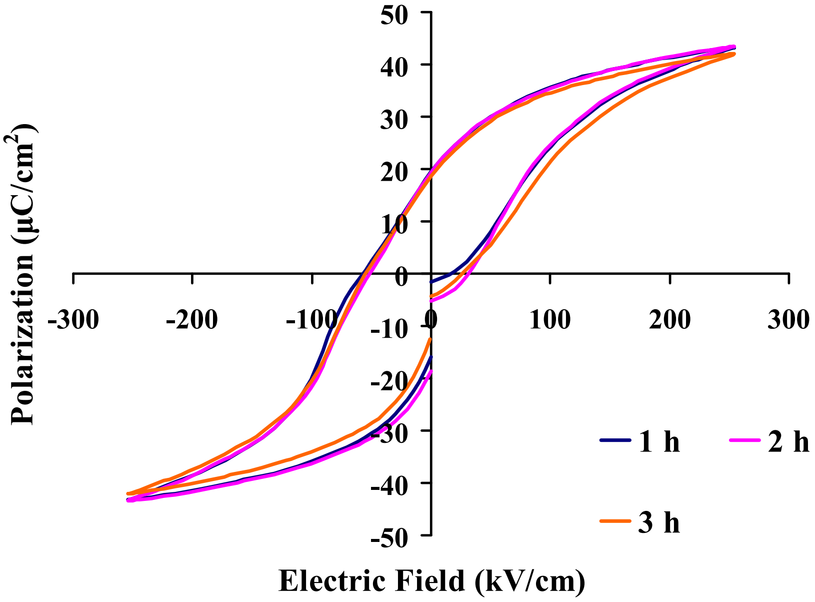

Figure A-11 Hysteresis curves of PNZT thin films with a composition $Pb_{0.985}(Zr_{0.53}Ti_{0.47})_{0.97}Nb_{0.03}O_3$ and sintered at 700 °C for 1, 2 and 3 h at an applied voltage of 10 V.

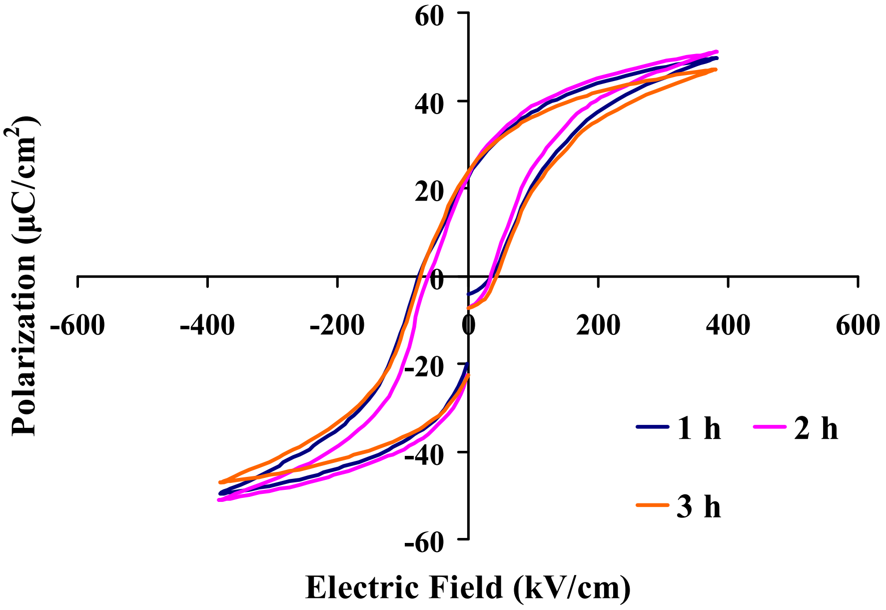

Figure A-12 Hysteresis curves of PNZT thin films with a composition $Pb_{0.985}(Zr_{0.53}Ti_{0.47})_{0.97}Nb_{0.03}O_3$ and sintered at 700 °C for 1, 2 and 3 h at an applied voltage of 15 V.

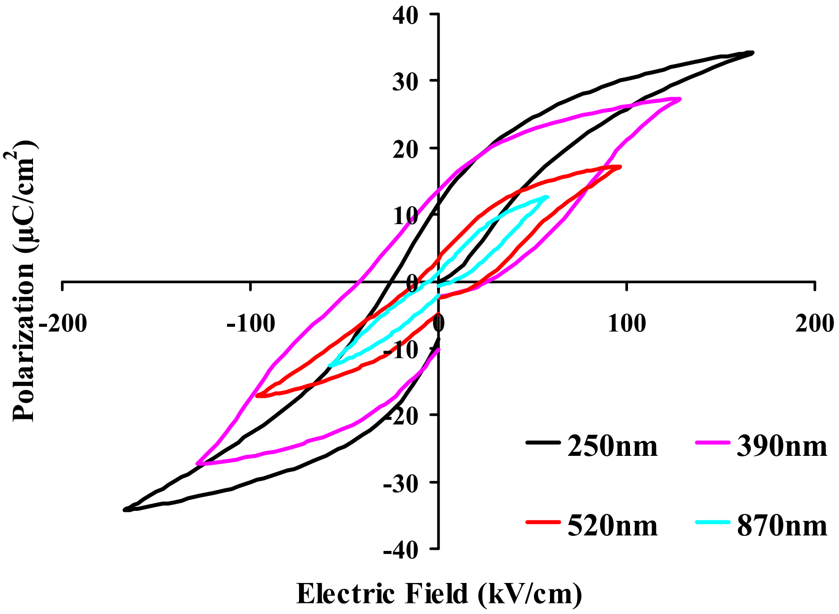

Figure A-13 Hysteresis curves of PNZT thin films with a composition $Pb_{0.985}(Zr_{0.53}Ti_{0.47})_{0.97}Nb_{0.03}O_3$ and sintered at 600 °C for 1 h with respect to changing thicknesses at an applied voltage of 5 V.

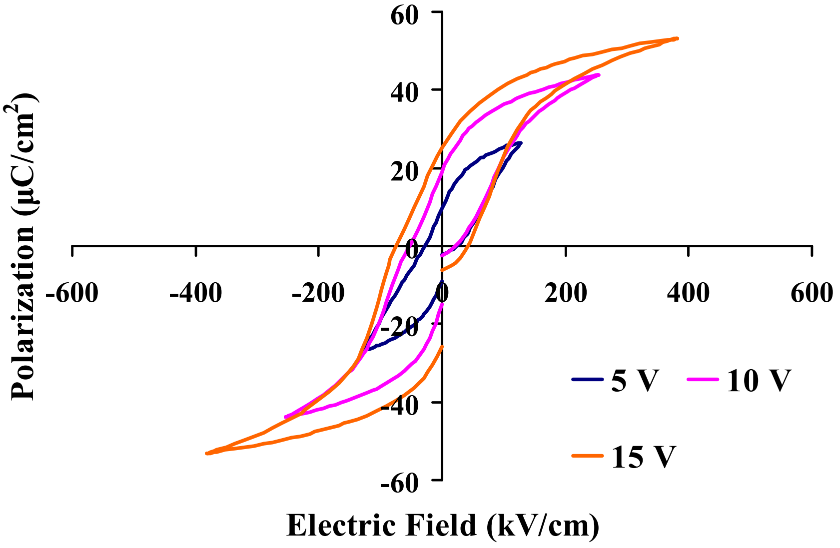

Figure A-14 Ferroelectric hysteresis behavior of PNZT $Pb_{0.985}(Zr_{0.53}Ti_{0.47})_{0.97}Nb_{0.03}O_3$ thin films sintered at 650 °C for 1 h and had a thickness of 390 nm at different applied voltages.

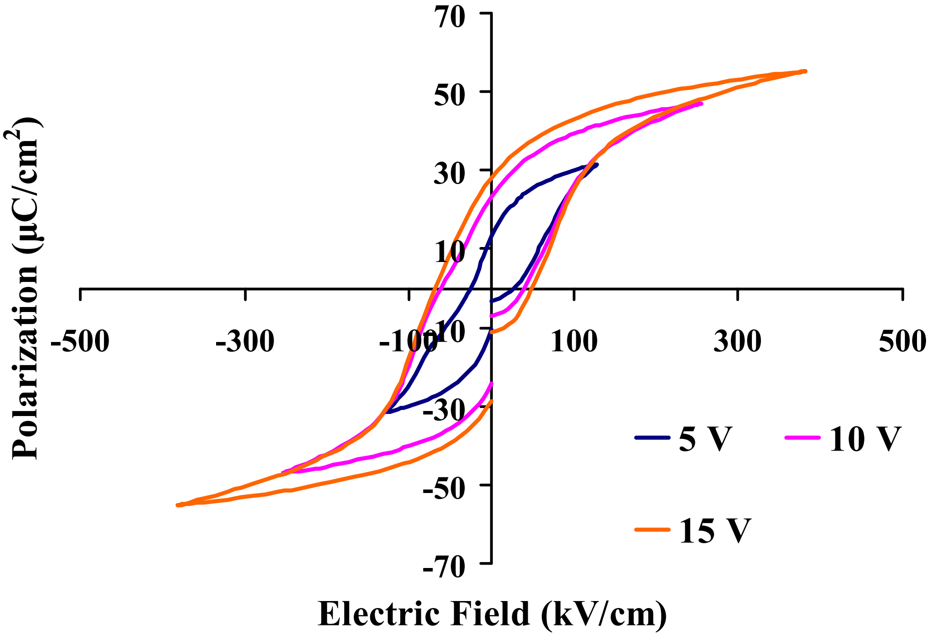

Figure A-15 Ferroelectric hysteresis behavior of PNZT $Pb_{0.985}(Zr_{0.53}Ti_{0.47})_{0.97}Nb_{0.03}O_3$ thin films sintered at 650 °C for 2 h and had a thickness of 390 nm at different applied voltages.

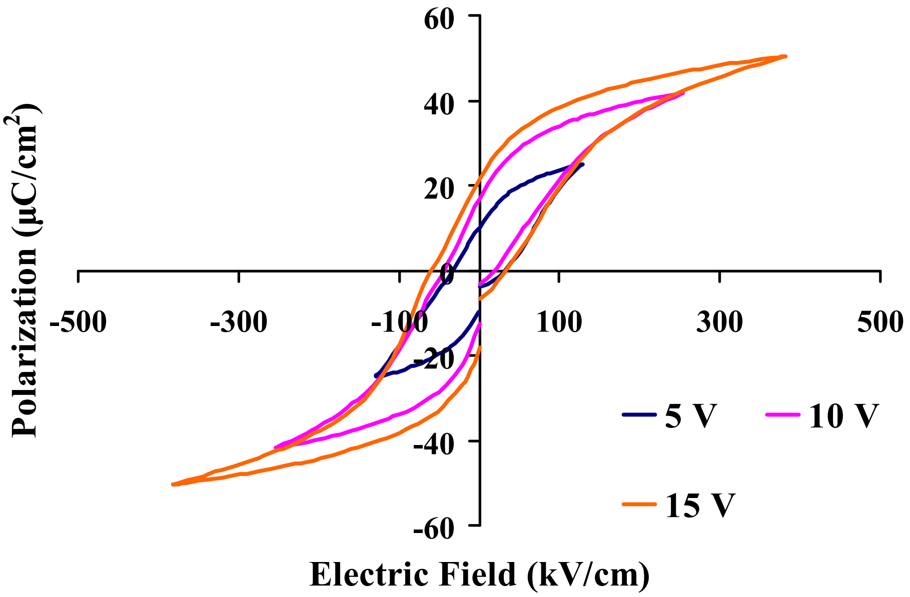

Figure A-16 Ferroelectric hysteresis behavior of PNZT $Pb_{0.985}(Zr_{0.53}Ti_{0.47})_{0.97}Nb_{0.03}O_3$ thin films sintered at 650 °C for 3 h and had a thickness of 390 nm at different applied voltages.

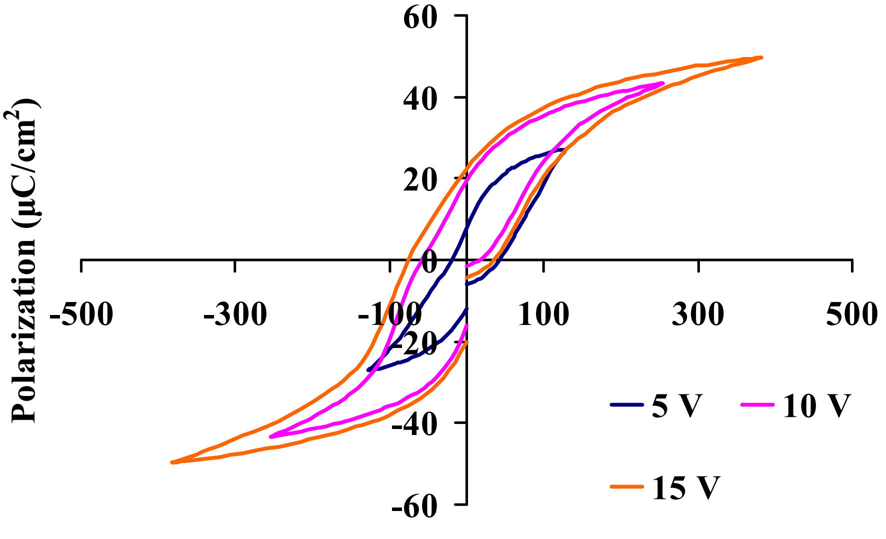

Figure A-17 Ferroelectric hysteresis behavior of PNZT $Pb_{0.985}(Zr_{0.53}Ti_{0.47})_{0.97}Nb_{0.03}O_3$ thin films sintered at 700 °C for 1 h and had a thickness of 390 nm at different applied voltages.

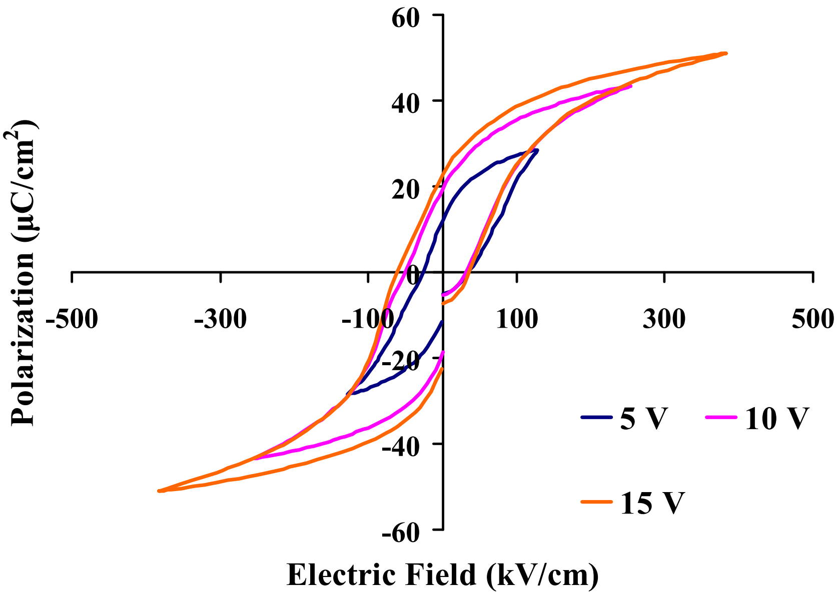

Figure A-18 Ferroelectric hysteresis behavior of PNZT $Pb_{0.985}(Zr_{0.53}Ti_{0.47})_{0.97}Nb_{0.03}O_3$ thin films sintered at 700 °C for 2 h and had a thickness of 390 nm at different applied voltages.

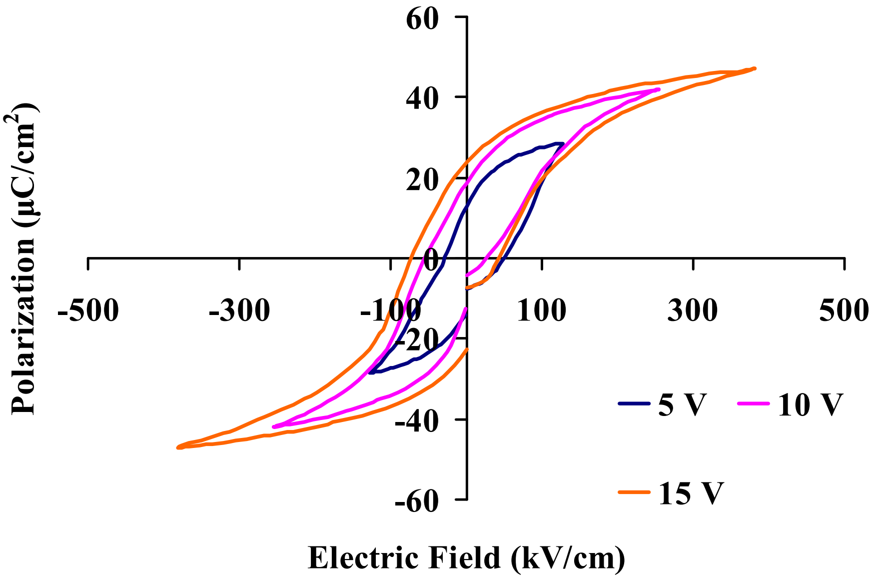

Figure A-19 Ferroelectric hysteresis behavior of PNZT $Pb_{0.985}(Zr_{0.53}Ti_{0.47})_{0.97}Nb_{0.03}O_3$ thin films sintered at 700 °C for 3 h and had a thickness of 390 nm at different applied voltages.

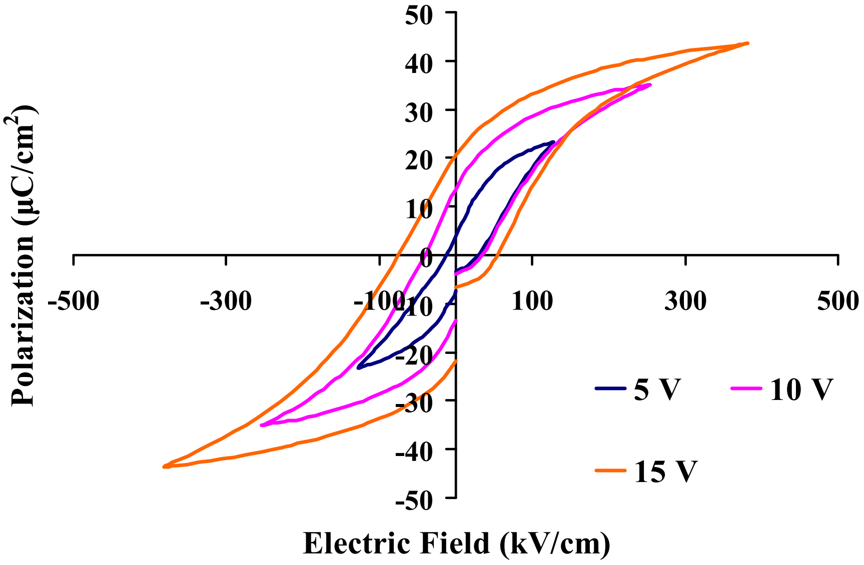

Fig. A-20. Ferroelectric hysteresis behavior of PNZT $Pb_{0.985}(Zr_{0.53}Ti_{0.47})_{0.97}Nb_{0.03}O_3$ thin films sintered at 600 °C for 2 h and had a thickness of 390 nm at different applied voltages.

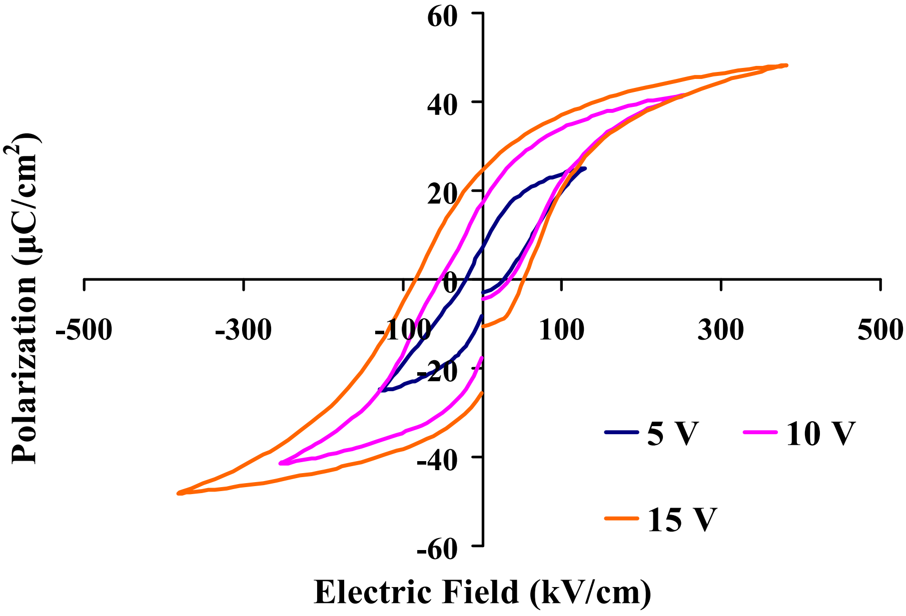

Fig. A-21. Ferroelectric hysteresis behavior of PNZT $Pb_{0.985}(Zr_{0.53}Ti_{0.47})_{0.97}Nb_{0.03}O_3$ thin films sintered at 600 °C for 3 h and had a thickness of 390 nm at different applied voltages.